Mesoscopic simulations of transport phenomena in reactive systems

Fan, R.

DOI
10.4233/uuid:f77bde56-de5b-49e5-87ab-80d8350fa099

Publication date
2024

Document Version
Final published version

Important note
To cite this publication, please use the final published version (if applicable).
Please check the document version above.

RONG FAN

MESOSCOPIC SIMULATIONS OF TRANSPORT PHENOMENA IN REACTIVE SYSTEMS

Mesoscopic simulations of transport phenomena in reactive systems

Dissertation

for the purpose of obtaining the degree of doctor
at Delft University of Technology
by the authority of the Rector Magnificus, prof.dr.ir. T.H.J.J. van der Hagen ,
chair of the Board for Doctorates
to be defended publicly on
Tuesday 29 October 2024 at 10 o'clock

by

Rong Fan

Master of Chemical Engineering, Eindhoven University of Technology
born in Shizuishan, China.

This dissertation has been approved by the promotor and copromotor.
Composition of the doctoral committee:

Rector Magnificus,	chairperson
Prof.dr.ir. Johan T. Padding	Delft University of Technology, promotor
Dr.ir. Remco M. Hartkamp	Delft University of Technology, copromotor

Independent members:

Prof.dr.ir. W. de Jong	Delft University of Technology
Prof.dr.ir. J.A.M. Kuipers	Eindhoven University of Technology
Prof.dr. R. Pecnik	Delft University of Technology
Dr. T.E. Burdyny	Delft University of Technology
Dr.ir. V. van Steijn	Delft University of Technology

Cover by: Rong Fan

Printed by: Ridderprint

to my parents and friends.

CONTENTS

SUMMARY

As one of the most widely employed types of chemical reactors within the chemical engineering industry, heterogeneous catalytic reactors have the versatility and efficiency to facilitate crucial chemical processes. For heterogeneous catalytic reactors, catalysts exist in a different phase than the reactants. Linking the macro-scale transport phenomena and the micro-scale reaction kinetics in the mesoscale is crucial to reactor design, optimization, and scale-up. Mesoscale simulations can assist in the study of heterogeneous catalytic reactors, understanding of the empirical knowledge and lowering the cost of reactor development. For this purpose, this dissertation presents 3 new tools developed for Stochastic Rotation Dynamics (SRD), a mesoscale method particularly well suited for problems involving both microscale effects on surfaces and transport phenomena in fluids: real-time temperature measurement and simulation, surface reactions and interactions simulation and surface reactions simulation in complex random geometry.

Many physical and chemical processes involve energy change with rates that depend sensitively on local temperature. Because of the multi-scale nature of heterogeneous catalytic reactors, it is desirable to connect the macroscopic world of continuous hydrodynamic and temperature fields to mesoscopic particle-based simulations with discrete particle events. The real-time measurement of the local temperature in dynamically changing environments is achieved in SRD method in **Chapter 3**, by employing ensembles averaging. After validation by heat diffusion between two isothermal plates, heating of walls by a hot strip, and by temperature programmed desorption, The method is applied to a case of a model flow reactor with temperature-sensitive heterogeneously catalysed reactions on solid spherical catalysts. In this model, adsorption, chemical reactions and desorption are explicitly tracked on the catalyst surface. This work opens the door for future projects where SRD is used to couple hydrodynamic flows and thermal fluctuations to solids with complex temperature-dependent surface mechanisms.

In heterogeneous catalysis, reactivity and selectivity are not only influenced by chemical processes occurring on catalytic surfaces but also by physical transport phenomena in the bulk fluid and fluid near the reactive surfaces. In **Chapter 4**, it is demonstrated how to simulate heterogeneous catalytic reactors by coupling an SRD fluid with a catalytic surface on which complex surface reactions are explicitly modelled. **Chapter 4** provides a theoretical background for modelling different stages of heterogeneous surface reactions. After validating the simulation method for surface reactions with mean-field assumptions, **Chapter 4** applies the method to non-mean-field reactions in which surface species interact with each other through a Monte Carlo scheme, leading to island formation on the

catalytic surface. The potential of the SRD method is shown by simulating a more complex three-step reaction mechanism with reactant dissociation.

The structure and geometry of a catalyst have a significant impact on its performance and efficiency. The fluid dynamics, as well as the resulting mass and energy transfer, are influenced by these factors. **Chapter 5** gives an approach of simulating randomly generated catalyst geometry in SRD, by voxelization of representing the geometry. Two random generating methods are provided for simulating different types of catalyst structure. The adsorption, reaction and desorption functions are prepared for coupling with the installation of complex geometry and are validated. The method is applied to randomly generate a 3D catalyst geometry with irregular connected pores, exhibiting the geometry influence to the product concentration distribution, as the result of mass transfer in porous media. This work suggests that the methodological advancements of SRD could contribute to the understanding and study of catalytic reactors, and become a tool for their design and optimization in chemical processes.

SAMENVATTING

Heterogene katalytische reactoren zijn een van de meest gebruikte types chemische reactoren in de chemische industrie. Ze zijn veelzijdig en efficiënt genoeg om cruciale chemische processen te vergemakkelijken. Bij heterogene katalytische reactoren bevinden katalysatoren zich in een andere fase dan de reactanten. Het koppelen van de transportverschijnselen op macroschaal en de reactiekinetiek op microschaal in de mesoschaal is cruciaal voor reactorontwerp, optimalisatie en opschaling. Mesoschaalsimulaties kunnen helpen bij het bestuderen van heterogene katalytische reactoren, het begrijpen van empirische kennis en het verlagen van de kosten van reactorontwikkeling. Voor dit doel presenteert dit proefschrift 3 nieuwe tools ontwikkeld voor Stochastic Rotation Dynamics (SRD), een mesoschaalmethode die bijzonder geschikt is voor problemen waarbij zowel microschaaleffecten op oppervlakken als transportverschijnselen in vloeistoffen betrokken zijn: real-time temperatuurmeting en simulatie, simulatie van oppervlaktereacties en interacties en simulatie van oppervlaktereacties in complexe willekeurige geometrie.

Veel fysische en chemische processen gaan gepaard met energieverandering met snelheden die gevoelig afhangen van de lokale temperatuur. Vanwege het multi-schaalkarakter van heterogene katalytische reactoren is het wenselijk om de macroscopische wereld van continue hydrodynamische en temperatuurvelden te verbinden met mesoscopische deeltjesgebaseerde simulaties met discrete deeltjesgebeurtenissen. De real-time meting van de lokale temperatuur in dynamisch veranderende omgevingen wordt bereikt met de SRD-methode in **Chapter 3**, door ensembles te middelen. Na validatie door warmtediffusie tussen twee isotherme platen, verhitting van wanden door een hete strip en door temperatuurgeprogrammeerde desorptie, wordt de methode toegepast op een modelstroomreactor met temperatuurgevoelige heterogene gekatalyseerde reacties op vaste bolvormige katalysatoren. In dit model worden adsorptie, chemische reacties en desorptie expliciet gevolgd op het katalysatoroppervlak. Dit werk opent de deur voor toekomstige projecten waarbij SRD wordt gebruikt om hydrodynamische stromingen en thermische fluctuaties te koppelen aan vaste stoffen met complexe temperatuurafhankelijke oppervlaktemechanismen.

In heterogene katalyse worden reactiviteit en selectiviteit niet alleen beïnvloed door chemische processen die plaatsvinden op katalytische oppervlakken, maar ook door fysische transportverschijnselen in de bulkvloeistof en vloeistof in de buurt van de reactieve oppervlakken. In **Chapter 4** wordt aangetoond hoe heterogene katalytische reactoren gesimuleerd kunnen worden door een SRD-vloeistof te koppelen aan een katalytisch oppervlak waarop complexe oppervlaktereacties expliciet gemodelleerd worden. Na validatie

van de simulatiemethode voor oppervlaktereacties met gemiddelde-veldaannames, past **Chapter 4** de methode toe op niet-gemiddelde-veldreacties waarbij oppervlaktespecies met elkaar interageren via een Monte Carlo-schema, wat leidt tot eilandvorming op het katalytische oppervlak. Het potentieel van de SRD-methode wordt aangetoond door een complexer drietrapsreactiemechanisme met reactordissociatie te simuleren.

De structuur en geometrie van een katalysator hebben een aanzienlijke invloed op zijn prestaties en efficiëntie. De vloeistofdynamica en de resulterende massa en energieoverdracht worden beïnvloed door deze factoren. **Chapter 5** geeft een benadering voor het simuleren van willekeurig gegenereerde katalysatorgeometrie in SRD, door voxelisatie van de geometrie. Twee willekeurig gegenereerde methoden worden gegeven voor het simuleren van verschillende soorten katalysatorstructuur. De adsorptie-, reactie- en desorptiefuncties worden voorbereid voor koppeling met de installatie van complexe geometrie en worden gevalideerd. De methode wordt toegepast om willekeurig een 3D katalysatorgeometrie met onregelmatig verbonden poriën te genereren, waarbij de invloed van de geometrie op de productconcentratieverdeling als gevolg van massaoverdracht in poreuze media wordt getoond. Dit werk suggereert dat de methodologische vooruitgang van SRD kan bijdragen aan het begrijpen en bestuderen van katalytische reactoren en een hulpmiddel kan worden voor hun ontwerp en optimalisatie in chemische processen.

PART I MAIN MATTER

1

INTRODUCTION

1.1 HETEROGENEOUS CATALYTIC REACTORS: A PROBLEM OF SCALES

In the world of physics, many large-scale phenomena are closely connected to small scale phenomena. An important example is given by industrial-sized heterogeneous catalytic reactors, the operation of which depends on the flow of a mixture of reactants and products at macroscale, mass and heat transfer, often through porous spaces, at mesoscale, and detailed surface chemistry at microscale, as shown in Fig. S1. This example is important because heterogeneous catalysis has played a dominant role in industrial production of chemicals and fuels for over a hundred years [1].

In most industrial applications, heterogeneous catalysts are solids or mixtures of solids, such as metals, transition metal oxides, zeolites, alumina, higher-order oxides, and graphitic carbon. Reactions occur on the active sites on the catalyst surface, which can bind with the reactant molecules. Often, catalysts are dispersed and supported by porous materials. The porous support does not only provide a large surface area, but can also influence the reaction rates, the conversion, the diffusivities of components, and the lifetime of the catalyst [2–4]. Moreover, defects on the surface of the catalyst material have an important influence on catalytic activity. This attracts frequent attention from researchers. Defects
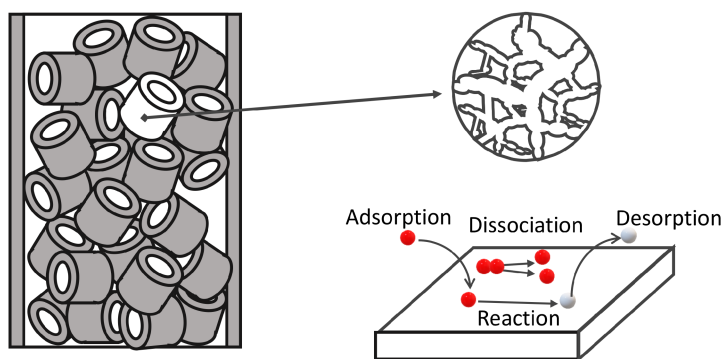
Figure 1.1: Examples of different scales in heterogeneous catalysis.

are caused by various factors in the process of catalyst preparation and can be randomly distributed on the catalyst surface. Due to these features, the chemical industry has to often face uncontrolled local catalytic reactions. This results in a series of problems such as the formation of hotspots, undesired products, and deactivation of catalysts.

The rate of chemical phenomena occurring in heterogeneous catalytic reactors is often controlled by mass transfer limitations. Moreover, as in many physical and chemical processes, heterogeneous reactions involve an exchange of energy with the surroundings as a consequence of the change in enthalpy between reactants and products. Understanding of heat transfer at different scales is required when studying heterogeneous catalysis, since one of the most common forms of energy exchanged in chemical reacion is thermal energy. A change in thermal energy is macroscopically perceived as a change in temperature, i.e. the "hotness" or "coldness" of matter [5]. More precisely, from statistical mechanics we know that temperature can be expressed in terms of the average kinetic energy of the velocity fluctuations of the constituent atoms relative to the average macroscopic flow [6].

To understand these effects, there is a great need for numerical tools that can model the interplay between mass transport of reactants and products, adsorption rates of reactants to catalytic surfaces, rates of different surface reactions, which are possibly influenced by the distribution of reaction intermediates and defects, and desorption rates of the products. Such detailed information and understanding of local properties within a reactor are hard to obtain from experiments, whereas they can be obtained by modeling. The interplay determines the overall reaction rate and selectivity toward a desired product. It also makes the modeling of heterogeneous catalysts a challenging multiscale and multiphysics problem.

1.2   MULTISCALE SIMULATION CHOICES AND MESOSCALE METHODS

To systematically study the link between macroscopic physical phenomena and the microscopic world, models and simulation methods are needed that can build bridges between different scales. A number of computational methods have been used to predict the mass transport of reactants and products in heterogeneous catalysis. At the macroscale, direct numerical simulations (DNS), which resolve the fluid flow around catalyst particles, have many applications for fluidized bed and packed bed reactors [7–9]. On an even larger scale, the discrete element method (DEM) can be used if correlations are known for the effective hydrodynamic forces and mass transfer rates between the unresolved fluid and catalyst particles [10–13]. Both DNS and DEM methods usually treat the transport of reactants and products inside the catalytic pellets through continuum (partial differential) equations, typically assuming some effective pore diffusion. In some cases, partial differential equations are also used on the level of pore networks [14, 15]. As popular methods for solving numerical equations, the finite element method (FEM) and finite volume method are widely

applied in simulating multiple types of physical and fluid problems, including the physics of chemical and thermal deconstruction processes in anisotropic macroporous particles [16].

A disadvantage of continuum methods is that, although they may describe the macroscale mass transport well, coupling between the continuous concentration fields and catalytic surfaces is typically achieved through source and sink terms (if pores are unresolved) or at best through simplified boundary conditions (if pore surfaces are resolved) for instance based on Langmuir adsorption kinetics and first-order reactions. With such a continuum approach it is difficult to properly include microscale finite size (Knudsen and thermal fluctuation) effects [17]. Moreover, it is practically impossible to include changes in reaction rates caused by microscale interactions between the different adsorbed species *on* the catalytic surface.

In such cases, microscale techniques, such as molecular dynamics (MD) simulations are preferred. Many computational studies of heterogeneous reactions focus on the prediction of individual elementary steps of the energy barriers, intrinsic elementary processes, information on supporting nanoparticles, and dynamic behavior of alloy clusters, which employ the density functional theory (DFT) and kinetic Monte Carlo simulations (kMC) [18, 19]. However, while these methods provide a more in-depth understanding of electronic structured reaction mechanisms, microscale techniques are usually too computationally expensive to simulate larger volumes of continuum fluid phases.

To fulfill the desire of exploring the gap scale phenomena, many researchers utilize various hybrid multiscale methods, combining microscale methods with macroscale methods, in studying transport phenomena in fluid phase influenced by reaction details [20–23]. In previous works, reactive systems have been modelled using direct simulation Monte Carlo (DSMC) [24, 25], the Lattice-Boltzmann method (LB) [26–29] and dissipative particle dynamics (DPD) [30, 31]. Many applications with chemical reactions are simulated with the LB method. However, LB is a pre-averaged method that does not exhibit thermal fluctuations without modifications. In contrast, coarse-grained or particle-based methods are better suited to include such microscale effects.

Stochastic rotation dynamics (SRD) [32, 33], which is the most widely used version of multi-particle collision dynamics (MPCD or MPC) methods, is advantageous in such cases. Most implementations of chemical reactions in SRD are homogeneous reactions [34, 35] or surface reactions with neglect of some processes such as adsorption, surface diffusion, or desorption through the use of mean-field rate expressions [36, 37]. Models of colloidal particles propelled by chemical reactions with adsorption-desorption kinetics such as diffusiophoretic Janus colloids and bi-particle catalytic reactions have been described before [38–43]. However, these works do not describe the detailed kinetics of changing catalyst sites. Sengar et al. were the first to incorporate Langmuir-Hinshelwood reaction kinetics by introducing individual steps like adsorption, desorption, and surface

reactions for a pseudo reaction A → B [44, 45]. It has been shown that SRD can simulate heterogeneously catalyzed systems and interlink surface and bulk phenomena which occur at different time and length scales. Particularly, SRD automatically accounts for thermal fluctuations and hydrodynamics, and can easily be extended to include reactions on surfaces. In addition, the influence of the porous catalyst structure has also been investigated through this method [46]. This makes SRD a promising tool to investigate the coupling of convection-diffusion mechanisms to microkinetic (adsorption-reaction-desorption) phenomena taking place on reactive surfaces and in porous media. For realistic catalytic reactions, more complex mechanisms exist, such as multiple elementary reaction steps or 'island formation' caused by interactions of surface particles, which lead to deviations from mean-field predictions [47, 48].

1.3 AIM OF RESEARCH AND THESIS STRUCTURE

The aim of this thesis is to develop a mesoscale simulation method that enables us to study the interplay of transport phenomena (convection, diffusion) with heterogeneous reactions taking place on surfaces in structured reactors and porous media. To simulate heterogeneous reactions with SRD, more reaction details need to be considered in the simulation, for example the dynamic surface composition and heat exchange resulting from the reactions, the molecular mass and number change, and the movement of coarse-grained particles in a complex geometry. A method that allows the extraction of macrophysical properties, such as temperature, should be developed. The precision of the method should allow the observation of microscale interactions between different species and between species and the catalyst surface. Furthermore, the method should be able to reflect the transport of particles through a complex porous geometry.

Chapter 2 gives a theoretical background of SRD for modelling hydrodynamics. It describes the technical details of this method, including the definition of simulation units.

Chapter 3 investigates a novel way to measure and simulate thermal dynamics in SRD, by which we extend the field of possible applications for the SRD method. A newly developed technique for real-time local temperature measurement is presented. To validate the method, different cases of heat conduction through a fluid phase and between a fluid and a solid phase are studied, allowing us to model heat effects in systems with surface reactions.

Chapter 4 describes how to model more complex heterogeneous catalytic reactions by coupling an SRD fluid to a catalytic surface on which surface reactions are explicitly modelled. Heterogeneous surface reactions with different mechanisms simulated in SRD are presented, including adsorption, particle interaction, and desorption. For validation, the simulations are applied to different cases of surface reactions with mean-field assumptions and for cases with surface interactions of species. Then, a three-step reaction mechanism

with reactant dissociation after adsorption is investigated to demonstrate the capability of the method when simulating more complex reaction mechanisms where mean-field assumptions fail.

Chapter 5 presents the development of a simulation methodology for heterogeneous catalysts with complex porous geometries. Two generation methods for random catalyst geometries are presented. An algorithm for updating the positions and velocities of SRD particles in complex geometries and coupling them to multi-step surface reactions is developed and validated. The influence of complex geometry is presented in a reactor simulation case and compared with a planar catalyst surface reactor simulation.

REFERENCES

[1]   Ioana Fechete, Ye Wang, and Jacques C Védrine. "The past, present and future of heterogeneous catalysis." In: *Catalysis Today* 189.1 (2012), pp. 2–27.

[2]   Gilbert F Froment, Kenneth B Bischoff, and Juray De Wilde. *Chemical reactor analysis and design*. Vol. 2. Wiley New York, 1990.

[3]   Chung-Kung Lee and Shyi-Long Lee. "Effects of the heterogeneous surface geometry on the selectivity behavior of a multi-step reaction." In: *Surface science* 339.1-2 (1995), pp. 171–181.

[4]   Kourosh Malek and Marc-Olivier Coppens. "Knudsen self-and Fickian diffusion in rough nanoporous media." In: *The Journal of chemical physics* 119.5 (2003), pp. 2801–2811.

[5]   J Mareš. "On the development of the temperature concept." In: *Journal of thermal analysis and calorimetry* 60.3 (2000), pp. 1081–1091.

[6]   William Thomson Baron Kelvin. *Mathematical and Physical Papers: 1841-1890*. Vol. 3. Cambridge University Press, 1890.

[7]   Niels G Deen, EAJF Peters, Johan T Padding, and JAM Kuipers. "Review of direct numerical simulation of fluid–particle mass, momentum and heat transfer in dense gas–solid flows." In: *Chemical Engineering Science* 116 (2014), pp. 710–724.

[8]   Saurish Das, Niels G Deen, and JAM Kuipers. "A DNS study of flow and heat transfer through slender fixed-bed reactors randomly packed with spherical particles." In: *Chemical Engineering Science* 160 (2017), pp. 1–19.

[9]   Arpit Singhal, Schalk Cloete, Stefan Radl, Rosa Quinta-Ferreira, and Shahriar Amini. "Heat transfer to a gas from densely packed beds of cylindrical particles." In: *Chemical Engineering Science* 172 (2017), pp. 1–12.

[10] Sijun Zhang, Xiang Zhao, and Zhi Yang. "Flow simulations in a pebble bed reactor by a combined DEM-CFD approach." In: *Nuclear Science and Engineering* 189.2 (2018), pp. 135–151.

[11] Julia Hartig, Hannah C Howard, Tanner J Stelmach, and Alan W Weimer. "DEM modeling of fine powder convection in a continuous vibrating bed reactor." In: *Powder Technology* 386 (2021), pp. 209–220.

[12] Kai Tong, Lijun Yang, and Xiaoze Du. "Modelling of TiO2-based packing bed photocatalytic reactor with Raschig rings for phenol degradation by coupled CFD and DEM." In: *Chemical Engineering Journal* 400 (2020), p. 125988.

[13]   Xiaoke Ku, Tian Li, and Terese Løvås. "CFD–DEM simulation of biomass gasification with steam in a fluidized bed reactor." In: *Chemical Engineering Science* 122 (2015), pp. 270–283.

[14]   Lin Zhang and NA Seaton. "The application of continuum equations to diffusion and reaction in pore networks." In: *Chemical Engineering Science* 49.1 (1994), pp. 41–50.

[15]   Philipp J Donaubauer, Leonhard Schmalhorst, and Olaf Hinrichsen. "2D flow fields in fixed-bed reactor design: a robust methodology for continuum models." In: *Chemical Engineering Science* 208 (2019), p. 115137.

[16]   Peter N Ciesielski, M Brennan Pecha, Nicholas E Thornburg, Meagan F Crowley, Xi Gao, Oluwafemi Oyedeji, Hariswaran Sitaraman, and Nicholas Brunhart-Lupo. "Bridging scales in bioenergy and catalysis: a review of mesoscale modeling applications, methods, and future directions." In: *Energy & Fuels* 35.18 (2021), pp. 14382–14400.

[17]   P Levitz. "Knudsen diffusion and excitation transfer in random porous media." In: *The Journal of Physical Chemistry* 97.15 (1993), pp. 3813–3818.

[18]   Benjamin WJ Chen, Lang Xu, and Manos Mavrikakis. "Computational methods in heterogeneous catalysis." In: *Chemical Reviews* 121.2 (2020), pp. 1007–1048.

[19]   Miguel Pineda and Michail Stamatakis. "Kinetic Monte Carlo simulations for heterogeneous catalysis: Fundamentals, current status, and challenges." In: *The Journal of Chemical Physics* 156.12 (2022), p. 120902.

[20]   Marco Kalweit and Dimitris Drikakis. "Multiscale simulation strategies and mesoscale modelling of gas and liquid flows." In: *IMA journal of applied mathematics* 76.5 (2011), pp. 661–671.

[21]   Yanping Li, Mingcan Zhao, Chengxiang Li, and Wei Ge. "Simulation study on the reaction-diffusion coupling in simple pore structures." In: *Langmuir* 33.42 (2017), pp. 11804–11816.

[22]   Mostafa Sulaiman, Eric Climent, Abdelkader Hammouti, and Anthony Wachs. "Mass transfer towards a reactive particle in a fluid flow: numerical simulations and modeling." In: *Chemical Engineering Science* 199 (2019), pp. 496–507.

[23]   Stefano Rebughini, Alberto Cuoci, and Matteo Maestri. "Hierarchical analysis of the gas-to-particle heat and mass transfer in micro packed bed reactors." In: *Chemical Engineering Journal* 289 (2016), pp. 471–478.

[24]   Sergey Gimelshein and Ingrid Wysong. "DSMC modeling of flows with recombination reactions." In: *Physics of Fluids* 29.6 (2017), p. 067106.

[25]   Sangita Swapnasrita, Georg R Pesch, Jochen AH Dreyer, Norbert Riefler, Thomas Wriedt, and Lutz Mädler. "Implementation of parcel method for surface reactions in DSMC." In: *Computers & Fluids* 187 (2019), pp. 1–11.

[26]   Roman S Voronov, Samuel B VanGordon, Vassilios I Sikavitsas, and Dimitrios V Papavassiliou. "Efficient Lagrangian scalar tracking method for reactive local mass transport simulation through porous media." In: *International journal for numerical methods in fluids* 67.4 (2011), pp. 501–517.

[27]   Meng Wang and Weibing Zhu. "Pore-scale study of heterogeneous chemical reaction for ablation of carbon fibers using the lattice Boltzmann method." In: *International Journal of Heat and Mass Transfer* 126 (2018), pp. 1222–1239.

[28]   Xuhui Meng and Zhaoli Guo. "Boundary scheme for linear heterogeneous surface reactions in the lattice Boltzmann method." In: *Physical Review E* 94.5 (2016), p. 053307.

[29]   CS Bresolin and AAM Oliveira. "An algorithm based on collision theory for the lattice Boltzmann simulation of isothermal mass diffusion with chemical reaction." In: *Computer Physics Communications* 183.12 (2012), pp. 2542–2549.

[30]   N Filipovic, Milos Kojic, and A Tsuda. "Modelling thrombosis using dissipative particle dynamics method." In: *Philosophical Transactions of the Royal Society A: Mathematical, Physical and Engineering Sciences* 366.1879 (2008), pp. 3265–3279.

[31]   Qinyu Zhu, Timothy R Scott, and Douglas R Tree. "Using reactive dissipative particle dynamics to understand local shape manipulation of polymer vesicles." In: *Soft Matter* 17.1 (2021), pp. 24–39.

[32]   Anatoly Malevanets and Raymond Kapral. "Mesoscopic model for solvent dynamics." In: *The Journal of chemical physics* 110.17 (1999), pp. 8605–8613.

[33]   G Gompper, T Ihle, DM Kroll, and RG Winkler. "Multi-particle collision dynamics: A particle-based mesoscale simulation approach to the hydrodynamics of complex fluids." In: *Advanced computer simulation approaches for soft matter sciences III*. Springer, 2009, pp. 1–87.

[34]   Kay Tucci and Raymond Kapral. "Mesoscopic Multiparticle Collision Dynamics of Reaction- Diffusion Fronts." In: *The Journal of Physical Chemistry B* 109.45 (2005), pp. 21300–21304.

[35]   Katrin Rohlf, Simon Fraser, and Raymond Kapral. "Reactive multiparticle collision dynamics." In: *Computer Physics Communications* 179.1-3 (2008), pp. 132–139.

[36]   Alireza Sayyidmousavi and Katrin Rohlf. "Reactive multi-particle collision dynamics with reactive boundary conditions." In: *Physical biology* 15.4 (2018), p. 046007.

[37] Jiang-Xing Chen, Yu-Guo Chen, and Raymond Kapral. "Chemically propelled motors navigate chemical patterns." In: *Advanced Science* 5.9 (2018), p. 1800028.

[38] Pierre de Buyl and Raymond Kapral. "Phoretic self-propulsion: a mesoscopic description of reaction dynamics that powers motion." In: *Nanoscale* 5.4 (2013), pp. 1337–1344.

[39] Jiang-Xing Chen and Raymond Kapral. "Mesoscopic dynamics of diffusion-influenced enzyme kinetics." In: *The Journal of chemical physics* 134.4 (2011), 01B624.

[40] Gunnar Rückner and Raymond Kapral. "Chemically powered nanodimers." In: *Physical review letters* 98.15 (2007), p. 150603.

[41] Pierre de Buyl. "Mesoscopic simulations of anisotropic chemically powered nanomotors." In: *Physical Review E* 100.2 (2019), p. 022603.

[42] Shang Yik Reigh, Mu-Jie Huang, Hartmut Löwen, Eric Lauga, and Raymond Kapral. "Active rotational dynamics of a self-diffusiophoretic colloidal motor." In: *Soft matter* 16.5 (2020), pp. 1236–1245.

[43] Andreas Zöttl. "Simulation of microswimmer hydrodynamics with multiparticle collision dynamics." In: *Chinese Physics B* 29.7 (2020), p. 074701.

[44] A Sengar, JAM Kuipers, Rutger A Van Santen, and JT Padding. "Particle-based modeling of heterogeneous chemical kinetics including mass transfer." In: *Physical Review E* 96.2 (2017), p. 022115.

[45] A Sengar, JAM Kuipers, RA van Santen, and JT Padding. "Towards a particle based approach for multiscale modeling of heterogeneous catalytic reactors." In: *Chemical Engineering Science* 198 (2019), pp. 184–197.

[46] Sebastian Muehlbauer, Severin Strobl, Matthew Coleman, and Thorsten Poeschel. "Simulation of catalytic reactions in open-cell foam structures." In: *arXiv preprint arXiv:2010.03904* (2020).

[47] Wen Lai Huang and Jinghai Li. "Mesoscale model for heterogeneous catalysis based on the principle of compromise in competition." In: *Chemical Engineering Science* 147 (2016), pp. 83–90.

[48] Joaquın Cortés, Heinrich Puschmann, and Eliana Valencia. "Mean-field hierarchical equations for some A+ BC catalytic reaction models." In: *The Journal of chemical physics* 109.14 (1998), pp. 6086–6091.

2

STOCHASTIC ROTATION DYNAMICS

In SRD, a system consisting of point particles is evolved with a discrete streaming step and a collision step in which all particles in a collision cell simultaneously exchange momentum. This general approach is often referred to as multi-particle collision dynamics (MPCD or MPC)[1] and shares some features with the Direct Simulation Monte Carlo approach. SRD refers to a particular implementation in which the collisions are executed through a stochastic rotation of the relative velocities of the particles in the collision cell [2]. Ihle and Kroll [3] pointed out that the introduction of a grid-shift procedure is necessary to sustain Galilean invariance. The fact that SRD is particle-based and generates Navier-Stokes hydrodynamics in an efficient way makes this method very suitable for simulations of complex systems such as equilibrium and nonequilibrium colloid and polymer solutions [4–15], microswimmers [16–22], and viscoelastic fluids [23–25]. Applications of SRD to biological systems have sprung up, such as for biological functional molecules, bacteria and cell suspensions and their dynamic behaviors [26–31].

In MPC, coarse-grained particles are used to represent the fluid, which evolve in discrete time steps, alternating between particle position updates and momentum exchange. The collisions between multiple particles are accounted for simultaneously rather than treating individual binary collisions of pairs of particles. This makes it computationally more efficient than DSMC when applied to dense fluids. Stochastic Rotation Dynamics is a widely used version of MPC in which the momentum exchanges via a rotation of the particle relative velocities around a randomly oriented axis [1].

The hydrodynamics resulting from the SRD method shows Navier-Stokes behavior on large length scales, while also automatically accounting for thermal fluctuations and (coarse-grained) molecular diffusion [32, 33]. In this technique, the positions and velocities of ideal particles obeying Newton's laws of motion are tracked through time.

There are two essential steps. In the streaming step, the position of every particle is advanced in time using its respective velocities by an Euler scheme. N particles are placed in the system to represent the fluid, with a total mass of $\Sigma_{j=1}^{k} X_j m_j N$. Here, X_j, m_j and k are the mole fraction, mass of component j, and the number of components in the system, respectively. In between two subsequent collisions, in the so-called streaming step, the position of each particle i is updated by a first order Euler scheme. If $\mathbf{r}_i^t$ and $\mathbf{v}_i^t$ are the

Table 2.1: Simulation parameters of SRD and derived units. In our simulations, the collision cell size, majority species mass and thermal energy at the reference temperature are the units of length, mass, and energy, respectively.

SRD fluid simulation parameters	
$a_0 \equiv 1$	Collision cell size
$m_0 \equiv 1$	Solvent (majority species) mass
$k_B T_0 \equiv 1$	Thermal energy (at reference temperature)
γ	Average number of particles per collision cell
Δt_s	Streaming integration timestep
Δt_c	Collision time interval
α	SRD rotation angle
Derived units	
Density	m_0/a_0^3
Time	$t_0 = a_0 \sqrt{\frac{m_0}{k_b T_0}}$
Diffusion coefficient	$D_0 = \frac{a_0^2}{t_0} = a_0 \sqrt{\frac{k_b T_0}{m_0}}$

position and velocity vectors of particle i at time t, and Δt_s is the timestep used during streaming, then the new position vectors are given by:

$$r_i^{t+1} = r_i^t + v_i^t \Delta t_s \tag{2.1}$$

If there is a body force applied to the fluid, e.g. to drive a flow, the velocity of particle i is updated in the streaming step according to

$$v_i^{t+1} = v_i^t + g \Delta t_s \tag{2.2}$$

In this expression, g is the acceleration associated with the body force.

Then, in the collision step, a grid divides the volume into cubic cells. The grid is shifted randomly before every collision step to ensure Galilean invariance [3] and 'ghost particles' are added in cells overlapping with walls to correct the fluid viscosity and velocity there. Afterwards, the particle velocities relative to the center of mass velocity in each cell are instantaneously rotated by a given angle around a randomly chosen axis, to mimic the exchange of fluid momentum. To increase the accuracy of handling wall collisions, multiple streaming steps per collision step can be taken, i.e. the collision time interval can be an integer multiple of the streaming integration time step.

The transport properties of the SRD fluid can be analytically expressed in terms of simulation parameters such as collision time step (Δt_c), the number density of particles (γ), thermal energy $k_b T$, cell size (a_0) and the mass of the particle (m_i). In SRD, the velocity vector of each particle is updated according to:

$$\mathbf{v}'_i = \bar{\mathbf{v}} + \mathbf{\Omega}(\mathbf{v}_i - \bar{\mathbf{v}}) \tag{2.3}$$

The fact that these analytical expressions, shown in Table 2.2, exist simplifies the use of SRD and reduces the need for trial and error simulations. The analytical expression for the (kinematic) shear viscosity ν has been derived and validated by Ihle and Tüzel [34–36]. Fig. 2.1 shows how different contributions to the shear viscosity scale with the dimensionless free path λ. Unlike the shear viscosity, no analytical expression for the collisional contribution to the self-diffusion coefficient has been derived due to the difficulty of theoretically including effects of hydrodynamic correlations on the self-diffusivity [1, 37]. The expression for the collisional contribution is derived from the assumption of molecular chaos. Therefore, the expression for the self-diffusion coefficient is most accurate when the dimensionless mean free path ($\lambda = \Delta t_c / t_0$) is larger than 0.6.[38]

In SRD, the temperature is not set as a direct parameter but is inherent in the particles' velocity fluctuations. The temperature can be controlled by modulating the velocity fluctuations, which can be done through various thermostatting schemes. For example, the Andersen thermostat reassigns the fluctuating velocities in each time step stochastically based on the Maxwell-Boltzmann distribution[2], and the Nosé–Hoover thermostat couples the system with an external reservoir in a way that allows for fluctuations in temperature[39–41]. In this work, a direct temperature scaling is used to maintain a strictly isothermal system: in the collision step, we add for each cell c containing $n_c \geqslant 2$ SRD particles the kinetic energy associated with velocity fluctuations, $K = \sum_{cell\,c} \sum_i^{n_c} \frac{1}{2} m_i \delta v_i^2$, and the number of degrees of freedom, $n_{free} = \sum_{cell\,c} 3(n_c - 1)$. This allows us to calculate an instantaneous global temperature $k_B T_{current} = 2K/n_{free}$ based on the velocity fluctuations in the entire system, independent of any convective flow velocities. Subsequently, the relative velocities in each cell are scaled by a factor $\sqrt{T_{target}/T_{current}}$, where T_{target} is the target temperature. This 'strong coupling' scheme is simple to apply, however does not allow for fluctuations in the instantaneous global temperature. Such a simplification is only justified if one is dealing with a very large number of particles, for which statistical mechanics predicts that the relative fluctuations in total energy ($\delta K/K \propto 1/\sqrt{n_{free}}$) are very small.

When dealing with multi-component mixtures, frictional forces between different components may lead to some unexpected behavior that cannot be explained by Fickian diffusion. A Maxwell-Stefan diffusion model is employed instead. In this framework, the

Table 2.2: Kinetic (streaming) and collisional contributions to SRD transport coefficients for a three-dimensional single-component SRD fluid, valid up to order $1/\gamma^2$. Note that the shear viscosity is expressed as a kinematic viscosity, i.e. with the same units as self-diffusivity.

	Kinetic contribution $\times\, k_B T \Delta t_c / (2m)$
Shear viscosity	$\nu = \dfrac{5\gamma}{(\gamma-1+e^{-\gamma})[2-\cos\alpha-\cos(2\alpha)]} - 1$
Thermal diffusivity	$D_T = \dfrac{3}{1-\cos\alpha}\left(1-\dfrac{1}{\gamma}\right) + \dfrac{24}{5\gamma} - 1$
Self-diffusivity	$D_s = \dfrac{3\gamma}{(\gamma-1+e^{-\gamma})(1-\cos\alpha)} - 1$
	Collisional contribution $\times\, a_0^2 / \Delta t_c$
Shear viscosity	$\nu = \dfrac{1}{18\gamma}(\gamma-1+e^{-\gamma})[1-\cos\alpha]$
Thermal diffusivity	$D_T = \dfrac{1}{15\gamma^2}(\gamma-1)[1-\cos\alpha]$

driving force of transport, which is linked to the spatial derivative of the chemical potential, can be balanced with the frictional forces. In SRD, multi-component diffusion is imposed due to the collision step that treats molecules based on their particle mass. The particle velocities are adjusted based on the center of mass velocity (mass weighted average velocity). For this reason, molecules with a large mass undergo smaller changes in velocity in the collision step than a particle with a smaller mass [1]. The Maxwell-Stefan diffusion coefficients $Đ_{ij}$ cannot be calculated a priori but they can be estimated. In binary dilute mixtures, the Darken equation can be used:

$$Đ_{12} = x_1 D_{2s} + (1 - x_1)D_{1s} \tag{2.4}$$

where D_{1s} and x_1 represent the self-diffusivity and mole fraction of species 1. This relation is used later when dealing with mixtures containing particles with varying masses.
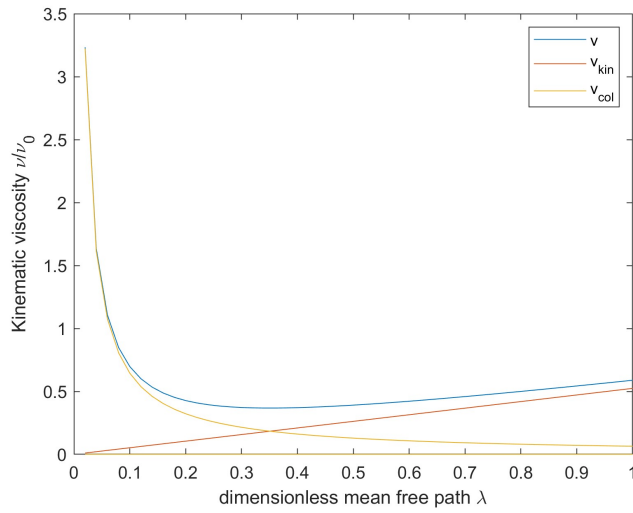
Figure 2.1: Kinetic and collisional contributions to the SRD kinematic viscosity as a function of dimensionless mean free path, controlled by the SRD collision time step.

REFERENCES

[1]   Anatoly Malevanets and Raymond Kapral. "Mesoscopic model for solvent dynamics." In: *The Journal of chemical physics* 110.17 (1999), pp. 8605–8613.

[2]   G Gompper, T Ihle, DM Kroll, and RG Winkler. "Multi-particle collision dynamics: A particle-based mesoscale simulation approach to the hydrodynamics of complex fluids." In: *Advanced computer simulation approaches for soft matter sciences III*. Springer, 2009, pp. 1–87.

[3]   T Ihle and DM Kroll. "Stochastic rotation dynamics: A Galilean-invariant mesoscopic model for fluid flow." In: *Physical Review E* 63.2 (2001), p. 020201.

[4]   Zhen-Yue Yang, Xiao-Fei Tian, Li-Jun Liu, and Ji-Zhong Chen. "Role of hydrodynamic interactions in the deformation of star polymers in poiseuille flow." In: *Chinese Journal of Polymer Science* 38.4 (2020), pp. 363–370.

[5]   Martin Wagner and Marisol Ripoll. "Solvent-induced depletion interactions in multiparticle collision dynamic simulations." In: *International Journal of Modern Physics C* 30.10 (2019), p. 1941008.

[6]   Maud Formanek and Angel J Moreno. "Single-chain nanoparticles under homogeneous shear flow." In: *Macromolecules* 52.4 (2019), pp. 1821–1831.

[7]   Antonio Lamura and Roland G Winkler. "Tethered Semiflexible Polymer under Large Amplitude Oscillatory Shear." In: *Polymers* 11.4 (2019), p. 737.

[8]   Chien-Cheng Huang, Roland G Winkler, Godehard Sutmann, and Gerhard Gompper. "Semidilute polymer solutions at equilibrium and under shear flow." In: *Macromolecules* 43.23 (2010), pp. 10107–10116.

[9]   Raghunath Chelakkot, Roland G Winkler, and Gerhard Gompper. "Migration of semiflexible polymers in microcapillary flow." In: *EPL (Europhysics Letters)* 91.1 (2010), p. 14001.

[10]   Dagmar Steinhauser, Sarah Köster, and Thomas Pfohl. "Mobility gradient induces cross-streamline migration of semiflexible polymers." In: *ACS Macro Letters* 1.5 (2012), pp. 541–545.

[11]   L Cannavacciuolo, RG Winkler, and G Gompper. "Mesoscale simulations of polymer dynamics in microchannel flows." In: *EPL (Europhysics Letters)* 83.3 (2008), p. 34007.

[12]   JT Padding and AA Louis. "Hydrodynamic interactions and Brownian forces in colloidal suspensions: Coarse-graining over time and length scales." In: *Physical Review E* 74.3 (2006), p. 031402.

[13]   A Malevanets and JM Yeomans. "Dynamics of short polymer chains in solution." In: *EPL (Europhysics Letters)* 52.2 (2000), p. 231.

[14]   JT Padding and AA Louis. "Hydrodynamic and Brownian fluctuations in sedimenting suspensions." In: *Physical review letters* 93.22 (2004), p. 220601.

[15]   Adam Wysocki, C Patrick Royall, Roland G Winkler, Gerhard Gompper, Hajime Tanaka, Alfons van Blaaderen, and Hartmut Löwen. "Direct observation of hydrodynamic instabilities in a driven non-uniform colloidal dispersion." In: *Soft Matter* 5.7 (2009), pp. 1340–1344.

[16]   Ingo O Götze and Gerhard Gompper. "Mesoscale simulations of hydrodynamic squirmer interactions." In: *Physical Review E* 82.4 (2010), p. 041921.

[17]   Gunnar Rückner and Raymond Kapral. "Chemically powered nanodimers." In: *Physical review letters* 98.15 (2007), p. 150603.

[18]   J Liam McWhirter, Hiroshi Noguchi, and Gerhard Gompper. "Flow-induced clustering and alignment of vesicles and red blood cells in microcapillaries." In: *Proceedings of the National Academy of Sciences* 106.15 (2009), pp. 6039–6043.

[19]   Mingcheng Yang and Marisol Ripoll. "Simulations of thermophoretic nanoswimmers." In: *Physical Review E* 84.6 (2011), p. 061401.

[20]   Kai Qi, Elmar Westphal, Gerhard Gompper, and Roland G Winkler. "Enhanced rotational motion of spherical squirmer in polymer solutions." In: *Physical review letters* 124.6 (2020), p. 068001.

[21]   Jan-Timm Kuhr, Felix Rühle, and Holger Stark. "Collective dynamics in a monolayer of squirmers confined to a boundary by gravity." In: *Soft Matter* 15.28 (2019), pp. 5685–5694.

[22]   Andreas Zöttl and Holger Stark. "Simulating squirmers with multiparticle collision dynamics." In: *The European Physical Journal E* 41.5 (2018), p. 61.

[23]   Yu-Guo Tao, Ingo O Götze, and Gerhard Gompper. "Multiparticle collision dynamics modeling of viscoelastic fluids." In: *The Journal of chemical physics* 128.14 (2008), p. 144902.

[24]   Shichen Ji, Run Jiang, Roland G Winkler, and Gerhard Gompper. "Mesoscale hydrodynamic modeling of a colloid in shear-thinning viscoelastic fluids under shear flow." In: *The Journal of chemical physics* 135.13 (2011), p. 134116.

[25]   Bartosz Kowalik and Roland G Winkler. "Multiparticle collision dynamics simulations of viscoelastic fluids: Shear-thinning Gaussian dumbbells." In: *The Journal of chemical physics* 138.10 (2013), p. 104903.

[26]   S Mahdiyeh Mousavi, Gerhard Gompper, and Roland G Winkler. "Wall entrapment of peritrichous bacteria: a mesoscale hydrodynamics simulation study." In: *Soft matter* 16.20 (2020), pp. 4866–4875.

[27]   Swapnil C Kohale and Rajesh Khare. "Cross stream chain migration in nanofluidic channels: Effects of chain length, channel height, and chain concentration." In: *The Journal of chemical physics* 130.10 (2009), p. 104904.

[28]   Richard M Jendrejack, Eileen T Dimalanta, David C Schwartz, Michael D Graham, and Juan J de Pablo. "DNA dynamics in a microchannel." In: *Physical review letters* 91.3 (2003), p. 038102.

[29]   Allen P Minton. "How can biochemical reactions within cells differ from those in test tubes?" In: *Journal of cell science* 119.14 (2006), pp. 2863–2869.

[30]   Gernot Guigas, Claudia Kalla, and Matthias Weiss. "The degree of macromolecular crowding in the cytoplasm and nucleoplasm of mammalian cells is conserved." In: *FEBS letters* 581.26 (2007), pp. 5094–5098.

[31]   Paolo Miocchi, Philippe Derreumaux, Fabio Sterpone, and Simone Melchionna. "Mesoscale biosimulations within a unified framework: from proteins to plasmids." In: *Molecular Simulation* 47.2-3 (2021), pp. 101–112.

[32]   Chien-Cheng Huang, Gerhard Gompper, and Roland G Winkler. "Hydrodynamic correlations in multiparticle collision dynamics fluids." In: *Physical Review E* 86.5 (2012), p. 056711.

[33]   Anoop Varghese, Chien-Cheng Huang, Roland G Winkler, and Gerhard Gompper. "Hydrodynamic correlations in shear flow: multiparticle-collision-dynamics simulation study." In: *Physical Review E* 92.5 (2015), p. 053002.

[34]   Thomas Ihle, E Tüzel, and Daniel M Kroll. "Equilibrium calculation of transport coefficients for a fluid-particle model." In: *Physical Review E* 72.4 (2005), p. 046707.

[35]   E Tüzel, Martin Strauss, Thomas Ihle, and Daniel M Kroll. "Transport coefficients for stochastic rotation dynamics in three dimensions." In: *Physical Review E* 68.3 (2003), p. 036701.

[36]   E Tüzel, Thomas Ihle, and Daniel M Kroll. "Dynamic correlations in stochastic rotation dynamics." In: *Physical Review E* 74.5 (2006), p. 056702.

[37]   Anatoly Malevanets and Raymond Kapral. "Solute molecular dynamics in a mesoscale solvent." In: *The Journal of Chemical Physics* 112.16 (2000), pp. 7260–7269.

[38]   Marisol Ripoll, K Mussawisade, RG Winkler, and G Gompper. "Dynamic regimes of fluids simulated by multiparticle-collision dynamics." In: *Physical Review E* 72.1 (2005), p. 016701.

[39]   Shūichi Nosé. "A molecular dynamics method for simulations in the canonical ensemble." In: *Molecular physics* 52.2 (1984), pp. 255–268.

[40]   Shuichi Nosé. "A unified formulation of the constant temperature molecular dynamics methods." In: *The Journal of chemical physics* 81.1 (1984), pp. 511–519.

[41]   William G Hoover. "Canonical dynamics: Equilibrium phase-space distributions." In: *Physical review A* 31.3 (1985), p. 1695.

TEMPERATURE MEASUREMENT AND HEAT TRANSFER

This chapter is based on the article:
Fan, R., Zachariah, G. T., Padding, J. T., Hartkamp, R. (2021). Real-time temperature measurement in stochastic rotation dynamics. Physical Review E, 104(3), [034124]. https://doi.org/10.1103/PhysRevE.104.034124

3.1 INTRODUCTION

Many physical and chemical processes involve an exchange of energy with the surroundings or the conversion of one form of energy to another. One of these forms is thermal energy. Temperature is commonly perceived as the "hotness" or "coldness" of matter [1]. More precisely, from statistical mechanics we know that temperature can be expressed in terms of the average kinetic energy of the constituent atoms in the absence of macroscopic flow [2].

Temperature is important for various physical and chemical processes, including adsorption, desorption and chemical reactions, which often take place at interfaces, such as the interface between a solid catalyst and a fluid containing the reactants and products. The rates with which these processes take place are not only influenced by microscale kinetic factors, but also by local macroscale properties such as pressure, hydrodynamic velocity fields and, importantly, temperature. Applications of these processes often involve fluids in complex geometries, for example adsorption in porous media or heterogeneously catalysed reactions taking place in packed bed reactors. When modelling such systems, one usually encounters the problem of having to tackle phenomena at different length scales ranging from the microscale to the macroscale.

Macroscale computational techniques are based on the continuum assumption. These techniques generally require solving conservation equations in the form of partial differential equations. As a results, the continuum methods model macroscopic effects of the embedded microscopic behavior directly [3]. The continuum assumption breaks down for systems where molecular effects such as Knudsen diffusion, and other effects that involve finite numbers of particles, are prominent. In such a case, microscale techniques, such as Molecular Dynamics (MD) simulations are preferred. However, microscale techniques

are usually too computationally expensive to simulate larger volumes of continuum fluid phases.

In such cases, it is advantageous to use mesoscale simulation methods, such as Lattice-Boltzmann (LB), Direct simulation Monte Carlo (DSMC), dissipative particle dynamics (DPD), or Stochastic Rotation Dynamics (SRD) [4]. The advantage of SRD in particular is that it automatically accounts for thermal fluctuations and hydrodynamics, and can easily be extended to include reactions on surfaces. This makes it a promising tool to investigate the coupling of convection-diffusion mechanisms to microkinetic (adsorption-reaction-desorption) phenomena taking place on reactive surfaces and in porous media.

In SRD, a system consisting of point particles is evolved with a discrete streaming step and a collision step in which all particles in a collision cell simultaneously exchange momentum. This general approach is often referred to as multi-particle collision dynamics (MPCD or MPC)[4] and shares some features with the Direct Simulation Monte Carlo approach. SRD refers to a particular implementation in which the collisions are executed through a stochastic rotation of the relative velocities of the particles in the collision cell [5]. Ihle and Kroll [6] pointed out that the introduction of a grid-shift procedure is necessary to sustain Galilean invariance. The fact that SRD is particle-based and generates Navier-Stokes hydrodynamics in an efficient way makes this method very suitable for simulations of complex systems such as equilibrium and nonequilibrium colloid and polymer solutions [7–18], microswimmers [19–25], and viscoelastic fluids [26–28]. Applications of SRD to biological systems have sprung up, such as for biological functional molecules, bacteria and cell suspensions and their dynamic behaviors [29–33]

Most of the implementation cases of SRD are assumed to be isothermal [34, 35]. However, recently researchers start to pay attention on the nonequilibrium simulations with SRD. Lepri [36] studied nonequilibrium steady states of a one-dimensional fluid in a finite domain with thermal walls. Investigating temperature effects has not been the first concern in this method, and is complicated by the feature of inherent thermal fluctuations. More precisely, in MPC or SRD, the temperature is not set as a direct parameter but is inherent in the particles' velocity fluctuations. This feature brings difficulties for measuring and simulating real-time local temperature change in the system, since the temperature is not an explicitly accessible variable of the simulation. Usually when there is viscous heating present in a non-equilibrium simulation, a thermostat is used to regulate temperature and establish a steady state. A thermostat rescales the relative velocities of particles in a collision cell, without compromising the cell-averaged velocity, nor the Maxwell-Boltzmann distribution in the collision step [5]. Thermostats are widely used in MPC, for example, Anderson Thermostat (MPC-AT) [34]. Dynamic parameter values remain constant in thermostatted systems, while the kinetic temperature relaxes to a fixed temperature.

If certain system properties are highly temperature dependent, local temperature variations can lead to strong feedback effects. An important example of this is heterogeneous catalysis, where the rates of catalyzed chemical reactions can change orders of magnitude due to a relatively small change of temperature. Because of the high sensitivity of reaction rates to local temperature, the conversion and selectivity in structured or packed bed reactors is intricately linked to variations in temperature that can change over relatively small time and length scales. Modelling such reactors with proper temperature-dependent local reaction rates thus requires measurement of the local temperature in real-time.

In this work, we investigate a novel way to measure and simulate thermal dynamics in SRD, by which we extend the field of possible application of the SRD method. This paper is arranged as follows. In section 3.2, we provide a theoretical background of SRD for modelling hydrodynamics and a newly developed technique for real-time local temperature measurement. In section 3.3, we validate the method for different cases of heat conduction through a fluid phase and between a fluid and a solid phase and investigate heat effects in systems with surface reactions. Finally, in section 3.4 we give our conclusions and outlook.

3.2   METHODOLOGY

In SRD, similarly to molecular dynamics simulations, temperature can be calculated from the average fluctuation velocities, i.e. particle velocities minus any contribution due to convective motion, of a sample of particles [37]. According to statistical mechanics, the instantaneous temperature of a collection of n particles may be determined from:

$$k_b T = \frac{1}{3(n-1)} \sum_{i=1}^{n} m_i (v_i - \bar{v})^2 \tag{3.1}$$

where the number of degrees of freedom (per Cartesian direction) n is reduced by one to account for the constraint that the average of the velocities v_i must equal the center-of-mass velocity $\bar{v}$ of all n particles. Based on Eq. (3.1), a local and instantaneous temperature $T(x_c, t)$ can be determined for each cell located at x_c. However, the number of particles per cell (typically in the range of 5 to 20) is usually too low to perform a statistically meaningful local and instantaneous measurement. For a system in steady state, a proper solution to find the – possibly spatially dependent – temperature is to locally average over many subsequent time instances, in other words to perform a long time average. Conversely, for systems with a certain symmetry in the geometry, this symmetry may be exploited to average over multiple equivalent locations and find the – possibly time dependent – average temperature. However, an unsteady state system with a complex geometry, such as the start-up of reactive flow in structured or packed bed reactors, calls

for an innovative way of averaging that preserves the local and instantaneous nature of the temperature field.

In this work we propose to determine the local and instantaneous temperature by averaging over sufficiently many independent realisations of the same system, i.e. replica averaging.

There are two ways in which replica averaging can be implemented: serial and parallel. In the serial implementation, each simulation is run to completion and saved, then reinitialized and repeated. The accumulated solution is then averaged at the end of n_s iterations. In a parallel implementation, n_s versions (replicas) of the simulation are performed simultaneously, while exchanging data and averaging between the replicas at each time step.

Both implementations have their advantages and disadvantages. Serial implementation is simpler to realize. It is well-suited for problems in which the dynamics are independent of on-the-fly information about the local temperature. For example, a study of heat transfer through a fluid between boundaries at different temperature can be easily realized with this technique since the influence of local temperature variations on the heat transfer is emergent. Parallel implementation is more involved, but it allows us to solve problems where on-the-fly information about the local temperature influences the dynamics of the system. For example, determining the reaction rate of a heterogeneously catalysed reaction requires access to a statistically meaningful measurement of the local instantaneous temperature. By using the power of parallel computing we can implement an ensemble of n_s equivalent versions of the system, while exchanging data and averaging each time step.

SRD or MPCD is naturally suitable for parallel computing, owing to the fact that the system is discretised in independent particles, and no differential equations need to be solved to simulate the fluid. Howard exploit the parallel computational capabilities of GPUs in the implementation of MPCD algorithm [38]. One way to implement parallel SRD is by using Compute Unified Device Architecture (CUDA), an extension to the C language developed by Nvidia. The advantage of this technique is that it can accelerate the simulation even if there is only one instance running. The implementation is suitable to all potential applications of SRD. However, such GPU-based implementations are often bottlenecked by hardware limitations. GPUs often possess smaller RAM capacities than CPUs, which could be limiting for a memory-intensive method such as the one studied in this work.

In this work, a new variation of SRD is developed that employs Open MPI. Parallel replicas of the simulation are executed simultaneously. Communication between the parallel simulations is only needed when averaging macroscopic properties such as local temperature. This can be handled efficiently in Open MPI. The parallel algorithm used in this study is shown in Fig. 3.1. The simulation starts by initializing multiple instances

(four instances in Fig. 3.1) of the simulation simultaneously. For each time step, every instance undergoes, independently from other instances, the streaming, wall bounce-back, and collision step, and any chemical or physical process implemented in the simulation that possibly partially depends on the local macroscopic variables. Local macroscopic variables are evaluated for each instance and then averaged between the instances and delivered back to each node. The overall mean values of macroscopic variables can then be used in the next time step.

3.2.1   HEAT EXCHANGE BETWEEN BULK FLUID AND BULK SOLID PHASE

The temperature of the bulk of a solid phase is often neglected in SRD. Rather, the wall temperature is usually accounted for via Boundary Conditions (BCs). In SRD, the most commonly used BC at a wall is the bounce back BC, leading to an effective no-slip boundary condition. In bounce back, all components of a particle's velocity are inverted when it collides with a solid surface or a hard wall of the domain, as in Eq. (3.2).

$$\boldsymbol{v}_i \rightarrow -\boldsymbol{v}_i \tag{3.2}$$

However, the bounce back BC does not allow for energy exchange between the fluid and the solid since the distribution of the post-collisional velocity exactly mirrors the distribution of the pre-collisional velocity. In other words, from a thermal perspective bounce back BCs are equivalent to adiabatic boundaries.

Any system with viscous fluid flow exhibits viscous dissipation: the kinetic energy associated with fluid flow is converted into thermal energy, which is observed as an increase in velocity fluctuations. Previous SRD studies [39, 40] removed this excess heat by enforcing a predetermined temperature. Such a thermostat is not utilizable here since the goal of this work is to mimic systems in which reaction heat or viscous dissipation can cause the temperature to evolve in time and space.

In many real systems, viscous heat generated in the fluid is removed via the confining walls. To mimic this, an option is to use the stochastic BC suggested by Padding and Louis [15]. In this BC, post-collision velocities at the surface are generated from the expected velocity distribution of SRD particles, at the desired wall temperature. This method results in a small slip velocity in systems with flow tangential to the wall, because of the non-zero average tangential velocity before the collision with the wall. A correction to this was proposed by Bolintineanu et al. [41]. Essentially, the Gaussian distribution in the tangential direction is biased with the local mean velocity to counteract the slip. This leads
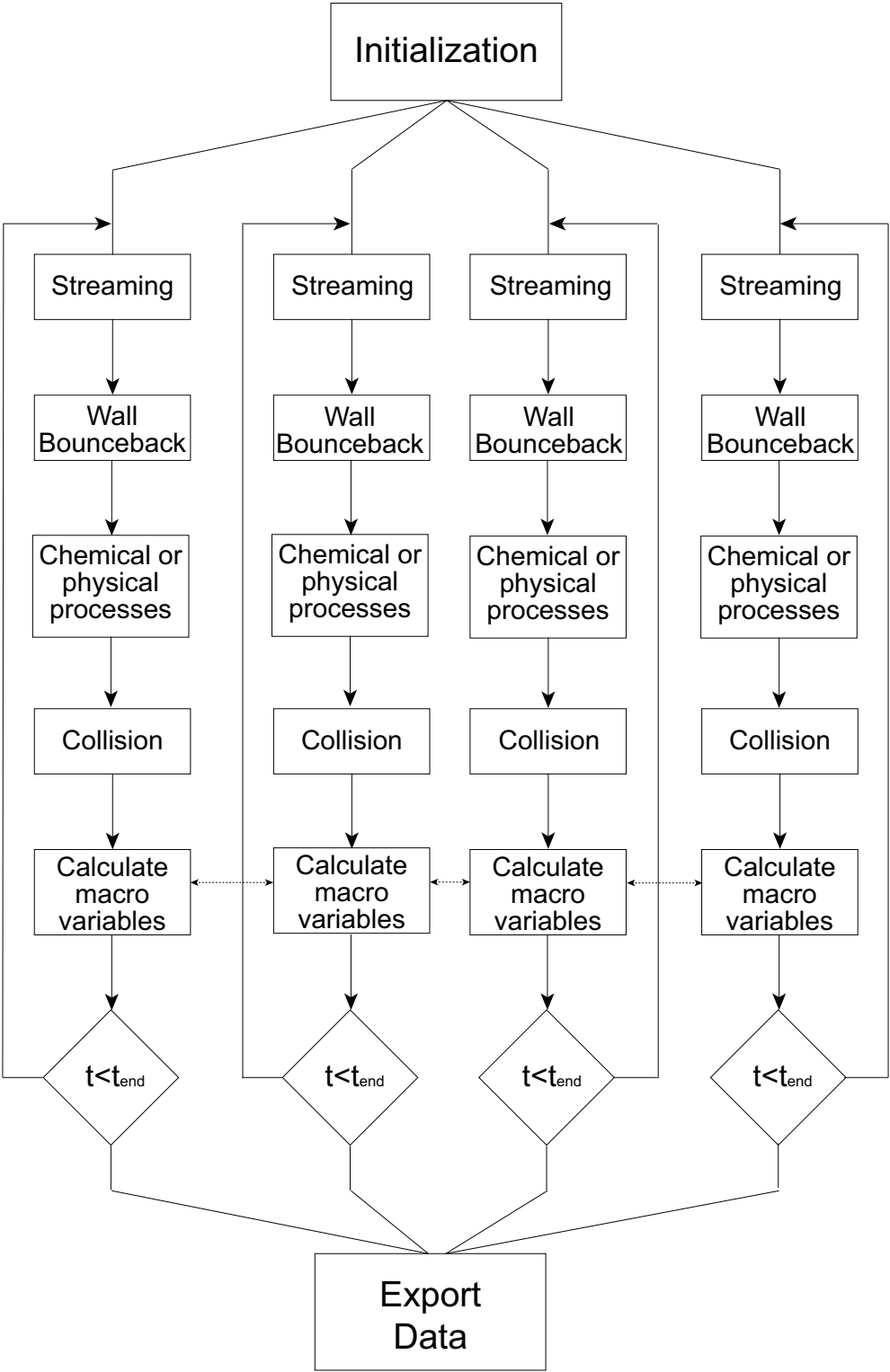
CHAPTER 3

Figure 3.1: Flowchart of the OpenMPI algorithm for parallel averaging of local macroscopic variables in SRD. In this example we show $n_s = 4$ instances (replicas).

to the following probabilities to generate new velocity components v_{ni} and v_{ti} normal and tangential to the wall, respectively, for a particle i that bounced into the wall:

$$P(v_{ni}) \quad = \quad v_{ni} \exp\left(-\frac{m_i v_{ni}^2}{k_B T_w}\right) \Theta(v_{ni}) \tag{3.3}$$

$$P(v_{ti}) \quad = \quad \sqrt{\frac{k_B T_w}{2\pi m_i}} \exp\left(-\frac{m_i(v_{ti} + \bar{v}_{ti})^2}{k_B T_w}\right) \tag{3.4}$$

where T_w is the wall temperature, $\Theta(v_{ni})$ is a Heaviside function ensuring that only positive normal velocities are generated, and $\bar{v}_{ti}$ is the fluid flow mean particle velocity of the cell in which particle i was located in the previous time step. Note that the + sign in front of $\bar{v}_{ti}$ in Eq. (3.4) is not a typo, because the mean tangential post-collisional velocity should be equal to $-\bar{v}_{ti}$, which corrects the slip velocity by using a bounce-back scheme on the mean local tangential velocity. No additional noise is introduced, since the mean velocity profile is obtained by averaging. Even though the number of particles in a single SRD cell is limited, the correction of the boundary condition is not affected. This method will henceforth be called the biased stochastic boundary condition.

The biased stochastic bounce-back BC not only enables us to specify the temperature of the wall boundary but also to describe the heat flux through the boundary between the fluid and solid phase. To this end it is important to also consider thermal conduction through the solid structure.

Temperature conduction in a solid is described by the governing energy equation:

$$\rho_s C_s \frac{\partial T}{\partial t} = K_s \nabla^2 T \tag{3.5}$$

where ρ_s is the density of the solid material, C_s is the heat capacity (per unit mass) and K_s is the thermal conductivity of the solid. Note that in practice we specify the thermal diffusivity $K_s/(\rho_s C_s)$ (in units of D_0) and the heat capacity per unit volume $\rho_s C_s$ (in units of $k_B T_0/a_0^3$) of the solid phase.

In this work the temperature field in a solid is evaluated on a Cartesian grid. Solids with curved surfaces are therefore approximated into cuboidal volumes. However, the fluid phase in coarse grained particle form is not influenced by this approximation. The spatial derivatives on the right side of Eq. (3.5) can be discretized using a central difference scheme.

For boundary cells, there are no more solid cells in one or more directions. Special care has to be taken in the directions where the solid is contacting the fluid. Taking a one-dimensional case, we can discretize the spatial derivative as:

$$K_s \frac{\partial^2 T}{\partial x^2} \quad = \quad \frac{K_s(\frac{\partial T}{\partial x})_{x+\Delta x/2} - K_s(\frac{\partial T}{\partial x})_{x-\Delta x/2}}{\Delta x}$$

$$= \quad \frac{-F_{x+} + F_{x-}}{\Delta x} \tag{3.6}$$

CHAPTER 3

where F_{x+} and F_{x-} denote the heat flux at the right and left interfaces of the cell. For interior cells, each of these terms can be further discretized with a general central difference scheme. For boundary cells, the flux term on the interface contacting the wall is replaced with the actual flux from the SRD fluid, which is determined as follows.

In the case of arbitrary geometries, a solid temperature mesh spans across the entire simulation domain, indicating cells that contain solid with a flag. The solid cells in contact with the fluid can be classified as a boundary cell, cells in the fluid as fluid cells, and solid cells fully surrounded by other solid cells as interior cells. Each solid temperature mesh cell contains the coefficients for itself and its six closest neighbors. In the preprocessing step, the interior cells are identified and given their coefficients. Then, the boundary cells are identified and given their coefficients according to Eq. (3.6), leaving out the external flux terms. This allows us to simply calculate the total energy transfer due to all particle-wall collisions in the cell without having to store in memory every location of surface collision.

When a particle collides with a wall, the exact location of the contact is calculated and the corresponding solid temperature mesh cell is identified. The flux due to the collision is then added to the flux variable of the mesh cell. All interior wall cells are given a flux value of 0 by default. The solid temperatures are then updated using the coefficient matrix to determine the discretization and the flux variable to add the necessary flux from the SRD fluid. This ensures that all wall cells can be updated with the same code, regardless of its contact with the fluid. A drawback of this method is the additional memory required to store the coefficient matrices. However, this memory requirement is small compared to that required to save the large number of simultaneous simulations.

The wall temperature T_w is determined from the solid cell temperature closest to the interface, and the post-bounce-back velocity of the particle is calculated using Eqs. (S3) and (3.4). This essentially changes the temperature of the outgoing particles to that of the local wall. The particle collisions with the interface of a specific solid cell during a time step result in energy change

$$\Delta E = \sum_i \frac{1}{2} m_i (\Delta v_{xi}^2 + \Delta v_{yi}^2 + \Delta v_{zi}^2) \tag{3.7}$$

that is quantifies the heat flux into the solid cell:

$$F_t = \frac{\Delta E}{\Delta x^2 \Delta t} \tag{3.8}$$

This heat flux is used in Eq. (3.6) to update the solid temperature [1]. This creates a two-way exchange of energy between the solid and the fluid.

---

1 Note the subtlety involved through our definition of the energy scale as $k_B T_0$: a unit change in local temperature corresponds to a 0.5 unit change in (kinetic) energy.

3.2.2 SURFACE HEAT SOURCES

In the previous part, we dealt with energy exchange between a fluid and a solid. We now consider the case where thermal energy is generated *on* the interface, for example as a result of adsorption or a (heterogeneous) surface reaction. Since the surface has no volume, and therefore no heat capacity, the question is how this heat should be initially distributed between the fluid phase and solid phase. For materials used in most common applications (solids in the form of metals, fluids in the form of water, air or other gases), the thermal diffusivity in the solid is larger than that in the fluid. In that case, surface heat tends to first predominantly transfer to the solid phase and only then to the fluid phase. This is the approach taken in this work.

When there is a surface heat source, the energy change in Eq. (3.7), which is used to determine the heat flux into the solid, must be replaced by:

$$\Delta E = \sum_i \frac{1}{2} m_i (\Delta v_{xi}^2 + \Delta v_{yi}^2 + \Delta v_{zi}^2) + \Delta E_{surf} \tag{3.9}$$

where ΔE_{surf} is the amount of heat generated on the surface.

3.3 RESULTS

Before investigating a complex process involving heat and mass transport, we first validate the method by computing the velocity profile under the modified boundary condition, the heat diffusion between two isothermal plates, and between a hot strip and solid walls that can be heated. We then present the temperature measurement during programmed desorption and a chemical reaction involving both the fluid phase and the solid phase.

3.3.1 BIASED STOCHASTIC BOUNDARY CONDITION

We validate the boundary conditions by comparing the simulated flow profile and the the analytical solution for a planar Poiseuille flow. The SRD fluid parameter values are chosen as: $\gamma = 7$, $\Delta t_c = 0.5$ and $\alpha = 90°$. The flow is induced by a body force $g = 0.001$ (in SRD units) acting on the SRD particles. This yields a Reynolds number of approximately 10.

The velocity profiles in Fig. (3.2) show that the bounce-back BC yields the closest agreement with the analytical solution. As expected, the stochastic BC shows some amount of slip, which is mostly corrected by the biased stochastic BC in Eq. (3.4). In this work, to demonstrate the significance of real-time temperature measurement and heat-transfer between solid and fluid, the biased stochastic BC is chosen in further simulations.
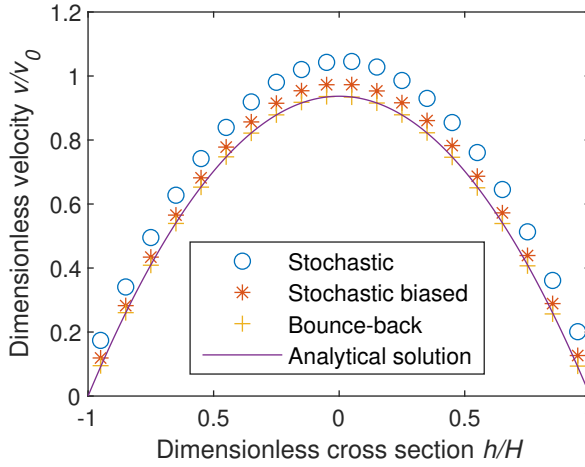
Figure 3.2: Comparison of analytical and simulated velocity in Poiseuille flow. The walls are kept at a constant temperature.

3.3.2   HEAT DIFFUSION BETWEEN ISOTHERMAL PLATES

Heat transfer is tested by simulating a fluid confined between two infinite plates (i.e., periodic boundary condition are applied in the x and z-direction). The plates are located at $y = 0$ and $y = L_y$, where L_y is the distance between the plates. In this case, the geometry of the simulation domain is set as $L_x = 15$, $L_y = 40$ and $L_z = 5$. The wall at $y = L_y$ is maintained at the initial temperature of 1, while the wall at $L = 0$ is instantaneously heated to a temperature of 1.1 at time $t = 0$, and maintained at this temperature throughout the simulation. The fluid number density was chosen to be $\gamma = 7$, the rotation angle $\alpha = 90°$, and time step size $\Delta t_c = 0.5$. Following the equations in Table 2.2, the thermal diffusivity varies between 0.5806 and 0.6371 depending on temperature, if the average fluid density of $\gamma = 7$ can be assumed fixed. 7500 simulations were conducted simultaneously for ensemble averaging. Analytically, one-dimensional heat transfer from a plate to an infinite domain is described by the following expression:

$$\frac{\partial T}{\partial t} = \frac{\partial}{\partial y}\left(D_T \frac{\partial T}{\partial y}\right) \tag{3.10a}$$

$$T(y, t = 0) = T_0 \quad T(y = 0, t) = T_w \tag{3.10b}$$

where T_0 and T_w are the initial system temperature and the heated wall temperature, respectively. If the thermal diffusivity D_T is assumed to be constant, the solution to the above differential equation can be readily found to be the complementary error function, with a width growing in time as $\sqrt{D_T t}$.
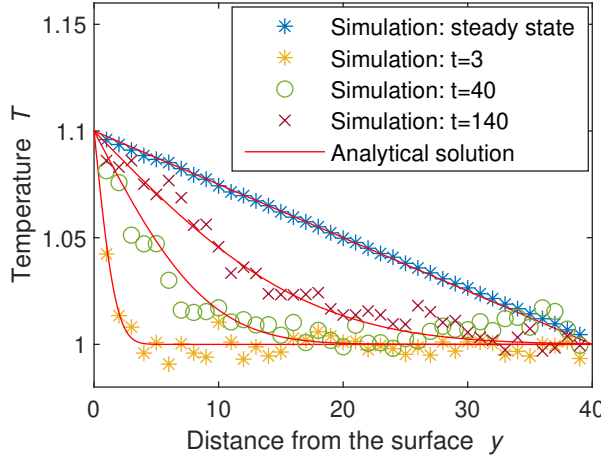
Figure 3.3: Time evolution of the temperature distribution between two isothermal plates; the analytical solution is under the assumption of a constant thermal diffusivity evaluated at the temperature of the hot plate.

In the simulation, the existence of the cold wall at $y = L_y$ invalidates this solution for an infinite domain, except for the initial times of the simulation when the effect of the hot wall has not yet reached the opposite cold wall. Moreover, the thermal diffusivity is not constant in the simulation, because it depends on the local temperature and local number density. For relatively small temperature differences between the two walls we can approximate the thermal diffusivity to be constant at the value of the hot wall (which is most relevant for thermal diffusion of the hotter parts of the fluid). Following this approach, Fig. (3.3) shows that the temperature evolution follows the expected analytical solution.

The thermal diffusivity can also be measured from the SRD simulation in various ways [6, 42–46]. For example, Ihle et al. [47] used a discrete-time projection operator technique to obtain the Green-Kubo relations for the transport coefficients. With the establishment of real-time temperature measurement in the present study, the thermal diffusivity can be measured more directly and computationally efficiently from the steady state heat flux to the walls during conduction between flat plates, given by:

$$F_{t,x=0} = K\frac{dT}{dx} \tag{3.11}$$

$$D_T = \frac{K}{\rho C_P} \tag{3.12}$$

where $F_{t,x=0}$ denotes the thermal flux at $x = 0$ (or any other plane in steady state), K is the thermal conductivity of the fluid, ρ the mass density and C_P the heat capacity per unit mass. We apply this method to to a system with fluid particle density $\rho = m\gamma = 50$.
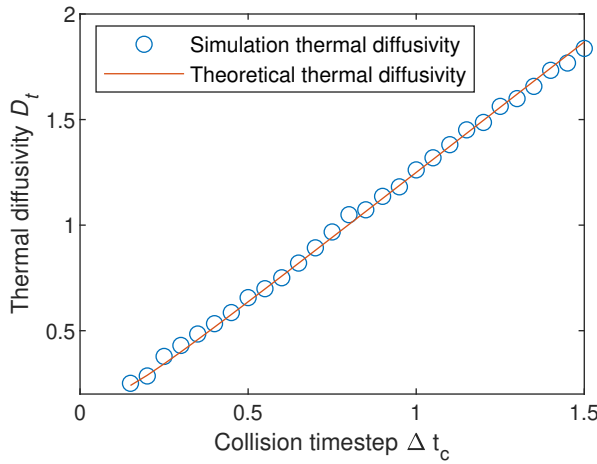
Figure 3.4: Comparison between the theoretical thermal diffusivity (Table 2.2) and the thermal diffusivity obtained from the measured heat flux (equation 3.12).

The resulting thermal diffusivity is shown in Fig. (3.4) for various settings of the collision time step Δt_c and compared with the theoretical solution for thermal diffusivity derived in the work of Ihle et al. [47]. The simulated results closely match the analytical solution.

3.3.3   FLUID CONFINED BETWEEN PLANAR WALLS

The exchange of heat between solid and fluid phases plays a key role in many processes. For example, the reaction kinetics and the catalyst efficiency in a heterogeneous catalytic reactor can be sensitive to temperature, and the formation of local hotspots due to the inefficient thermal conductivity can cause severe problems. In simulating such problems, a heat transfer model between solid and fluid is necessary.

The performance of the fluid-solid coupled model introduced in Sec. 3.2.1 is evaluated by conducting a test case in which a heat flow is induced between two planar surface. A rectangular strip of the wall at $y = 0$ is maintained at a temperature of 1.1 (see Fig. (3.5)), whereas the temperature of the rest of the wall and the wall at $y = L_y$ can evolve freely from an initial temperature of 1.0. A 10% maximum difference in temperature is chosen to limit the effects of changes in temperature-dependent properties such as diffusivity, while producing a relatively high signal-to-noise ratio. The latter reduces the needed number of parallel simulations to be run for averaging.

Fig. 3.6 presents the evolution of the local wall surface temperatures with time. The temperatures are averaged in the x-direction since the system does not vary along this direction. It can be observed that the conduction through the fluid to the cold wall occurs
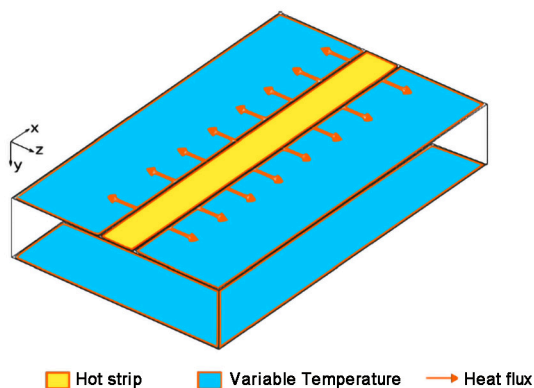
Figure 3.5: Schematic of the heated wall. Blue represents the zone with variable temperature, yellow the heated zone and the red arrows denote the direction of heat flow. Domain boundaries in x and z coordinates are periodic.

as expected. Since the temperature of the heated strip is higher than the surroundings, the temperature increase of the fluid starts near the hot strip. The opposite wall slowly increases in temperature due to the thermal diffusion across the gap.

3.3.4 TEMPERATURE PROGRAMMED DESORPTION AND ISOTHERMAL SURFACE REACTIONS

By now, the foundation for the real-time temperature measurement has been laid. Next, we will demonstrate that the model is suitable for simulating complex surface processes like heterogeneous chemical reactions, which contains three steps: adsorption, reaction and desorption at catalytic surface sites.

To implement heterogeneous chemical reactions, the Langmuir adsorption-reaction model proposed by Sengar [48] is applied. Details of the model can be found in appendix a.1.

In the preprocessing step, the catalyst surface is assigned active sites. They can either be distributed uniformly on the surface in a fixed grid pattern, or they can be randomly distributed. In this work, we distribute the active sites randomly onto discretized surface cells. For simplicity, these cells are taken to be the intersections between the solid and the SRD grids. A particle is then adsorbed exactly where it collides with the wall if there are any free active sites in the cell. This way, instead of fixing the locations of each active site, we fix the number of active sites in each cell, which determines the capacity of the cell to hold adsorbed particles. In this way, the catalyst sites can be easily implemented for complex boundaries. It is notable that being coarse-grained particles, the SRD particles
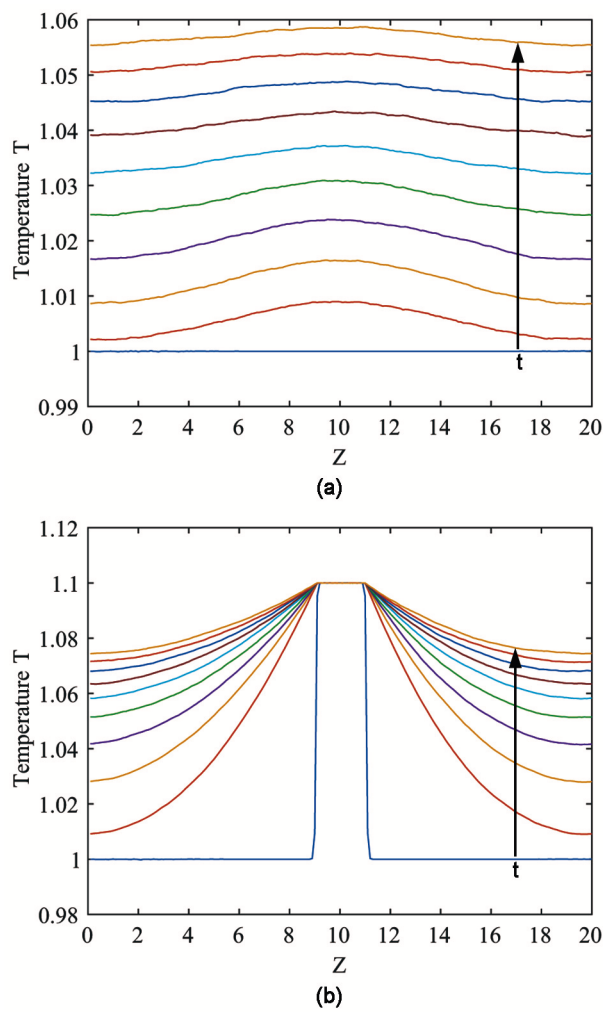
Figure 3.6: Temperature evolution of the surface of the unheated (a) and heated (b) wall with time. Subsequent time steps are plotted above each other to illustrate the change in temperature profile with time.

represent multiple molecules and similarly the catalyst sites are larger than the size of molecular catalyst sites.

The grid shift procedure needs to be adjusted for the presence of catalytic spheres. Ghost particles are added when the particle density in the SRD cell near a sphere is lower than average number density of the fluid, which is similar to the treatment of the wall of the domain described in Chapter 2. The velocities of these particles are taken from a Gaussian distribution with mean velocity equal to that of the spherical particle (zero for the fixed spheres in this work)and the same temperature as the fluid, as determined in the previous step.

We first perform a virtual experiment of temperature programmed desorption (TPD) from a slowly heated solid spherical catalyst in a bath of SRD particles. The geometry of the test domain is set to $L_x = L_y = L_z = 20$, and the sphere radius is 2 with in total 10000 catalytic sites on the surface. To load the sphere surface with particles, the adsorption probability prefactor p_a^0 is set to 0.5 and desorption probability prefactor p_d^0 to 0. The simulation is then allowed to run until all N_{cat} catalytic sites per unit area are occupied. The temperature of the solid is then lowered to 0.1 and subsequently slowly increased at a rate of $\beta = 0.001$. The adsorption probability prefactor is set to 0 to avoid re-adsorption. The desorption probability prefactor is set to 1 and the particles are allowed to desorb from the surface as the temperature increases. Δt_s is the streaming time interval as the timestep to update adsorption, reaction and desorption. The fractional surface coverage of the sphere $\theta = N_a/N_{cat}$, where N_a is the number of adsorbed particles per unit area and N_{cat} is the number of catalytic sites per unit area, will evolve according to the rate of desorption:

$$\frac{d\theta}{dt} = -\theta \frac{p_d^0}{\Delta t_s} e^{-E_d/k_B T} \tag{3.13}$$

where E_d is the desorption activation energy, set to $0.5 k_B T_0$ in this example. The left hand side can now be transformed as:

$$\frac{d\theta}{dt} = \frac{d\theta}{dT}\frac{dT}{dt} = \frac{d\theta}{dT}\beta \tag{3.14}$$

Therefore, the final expression for the TPD curve can be written as:

$$\frac{d\theta}{dT} = -\frac{p_d^0}{\beta \Delta t_s}\theta e^{-E_d/k_B T} \tag{3.15}$$

Eq. (4.10) can be solved numerically to obtain the final solution. This resulting solution, the desorption rate as the change of $\frac{d\theta}{dt}$ with temperature is compared with the simulation results in Fig. 3.7. It shows that the observed simulation results closely agree with the theoretical prediction, which validates that the desorption model exhibits the expected
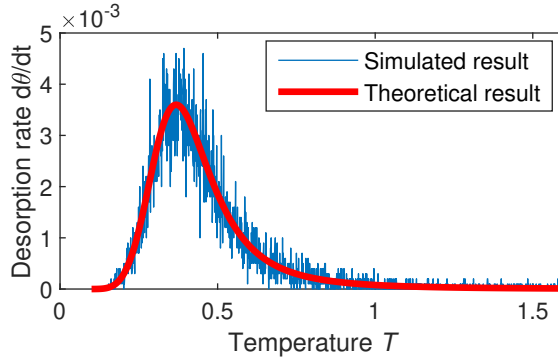
Figure 3.7: Desorption rate versus temperature during a Temperature Programmed Desorption (TPD) virtual experiment where the sphere temperature is increased at a rate of $\beta = 0.001$.

temperature kinetics. The fluctuations in the simulation results are a consequence of density fluctuations in the SRD fluid.

Next, we test the competition between adsorption, reaction and desorption for an isothermal case (in the next section we will investigate heat effects). At the catalyst surface, an adsorbed reactant particle A reacts to form a product particle B. While both A and B are set to have equal adsorption and desorption probability prefactors as well as activation energies, the desorption probability prefactor is set to a low value of 0.05 to create a rate limiting step when adsorption probability prefactor is 0.5. This also avoids unwanted hydrodynamic effects due to sudden changes in local density. The probability prefactor for reaction is set to 0.005. The real-time fractional surface coverage is then measured. As explained in Appendix a.1, the number of A and B particles adsorbing per unit area per unit time can be written as:

$$R_{A,ads} = C_A \sqrt{\frac{2k_B T}{\pi m_A}} p_a^0 \left(1 - \frac{N_{A,ads} + N_{B,ads}}{N_{cat}}\right) e^{-E_a/k_B T}$$

(3.16)

$$R_{B,ads} = C_B \sqrt{\frac{2k_B T}{\pi m_B}} p_a^0 \left(1 - \frac{N_{A,ads} + N_{B,ads}}{N_{cat}}\right) e^{-E_a/k_B T}$$

(3.17)

where C_A and C_B are the local concentrations (number densities) of A and B particles, respectively, and the term between brackets is the explicit form of $(1 - \theta)$, expressed in terms of the number of adsorbed A and B particles per unit area, $N_{A,ads}$ and $N_{B,ads}$,
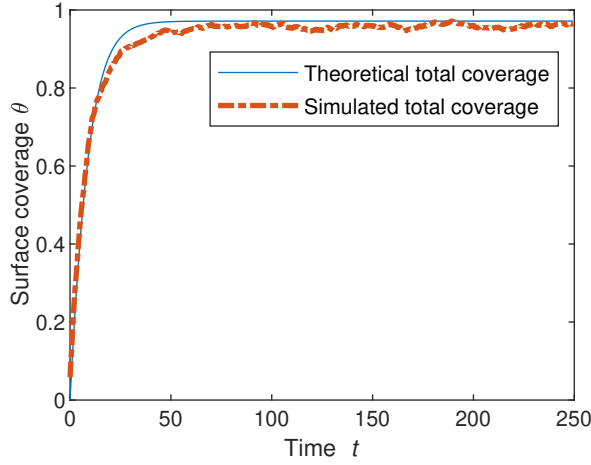
Figure 3.8: Time dependence of surface coverage of a catalytic sphere for isothermal adsorption-reaction-desorption.

relative to the total number of catalytic sites per unit area, N_{cat}. The number of A and B particles desorbing per unit area per unit time can be written as:

$$R_{A,des} \quad = \quad N_{A,ads} \frac{p_d^0}{\Delta t_s} e^{-E_d/k_B T} \qquad (3.18)$$

$$R_{B,des} \quad = \quad N_{B,ads} \frac{p_d^0}{\Delta t_s} e^{-E_d/k_B T} \qquad (3.19)$$

Finally, the number of A reacting to B per unit area per unit time (assuming an irreversible reaction) can be written as:

$$R_{A,react} = N_{A,ads} \frac{p_r^0}{\Delta t_s} e^{-E_r/k_B T} \qquad (3.20)$$

These equations can now be combined to form a set of differential equations governing the number of A and B on the surface:

$$\frac{dN_{A,ads}}{dt} \quad = \quad R_{A,ads} - R_{A,des} - R_{A,react} \qquad (3.21)$$

$$\frac{dN_{B,ads}}{dt} \quad = \quad R_{B,ads} - R_{B,des} + R_{A,react} \qquad (3.22)$$

These equations can be solved numerically to give the surface particle numbers with time. In our numerical solution, we assume that the amount of B particles re-adsorbing onto the surface is negligible, so we effectively set $\gamma_B = 0$.

Fig. 3.8 compares the surface coverage in the numerical solution (blue line) and the SRD model (red dots). It can be seen that the SRD solution closely resembles the numerical solution. The equilibrium total surface coverage can be seen to match the theoretical value, proving that the adsorption and desorption are working as expected.

3.3.5   SURFACE REACTIONS ON CATALYTIC PARTICLES WITH HEAT EFFECTS

To further demonstrate the real-time measurement of temperature in heterogeneous catalytic reaction simulations, a model with multiple spherical catalyst particles is tested in a flowing reactant medium. For heterogeneous catalytic reactions in densely packed beds, dead-zones in the hydrodynamic fields, which can cause the formation of hot-spots in the domain. These hot-spots could be catastrophic for the reactor. Simulations can aid in understanding, controlling and preferably preventing the emergence of hot spots.

To replicate the conditions in a densely packed bed reactor where. hot-spots may form, spherical catalyst particles are configured closely together. Fig. 3.9 shows a schematic of the simulation geometry, which consists of a periodic fluid domain with a thermostatted buffer region at $x = L_x$ spanning a length of 5 units. 1, 2 or 3 spheres with a radius of 3 are inserted at $z = L_z/2$, each sufficiently far away from the buffer region. A flow is induced by a uniform forcing term in the x-direction. The buffer region returns the outlet fluid to a constant temperature of 1, while also converting B particles back into A, avoiding accumulation of B in the system. L_x is chosen to be 20 (plus buffer region), L_y is 26, and L_z is 16.

The coordinates of spheres 1, 2, and 3 are (6,13,13), (12,8,13), (12,19,13), respectively. In this configuration, when simulating more than one catalytic sphere, the distance between them is set to be slightly larger than 1 SRD cell. This procedure keeps the catalytic spheres close enough to show effects of heat accumulation in the narrow area between the spheres. Individual solid temperature meshes are created for each sphere in the domain. The fluid collision time step is set to 0.5 and the local particle density to 7. The flow is driven by a body force $g = 0.001$. The arrangement method of catalytic sites is the same as for the temperature programmed desorption case and explained in Section 3.3.4 The number of catalyst sites per catalytic sphere is 100. The complete simulation settings are listed in Tab. (3.1). 250 simulations were conducted simultaneously to enable real-time temperature measurement.

Fig. 3.10 presents the product density field in the simulation domain. Subfigures 3.10a, 3.10b and 3.10c show the steady state number density contour on the plane $z = L_z/2$ for the three scenarios. It is clearly visible how in the buffer region the product particles are reset to reactant particles. From the product density distribution in 3.10a, 3.10b and 3.10c, it can be seen that convection-diffusion of the product from the surface of the catalyst occurs and varies for the 3 scenarios. The distribution of the product in the domain
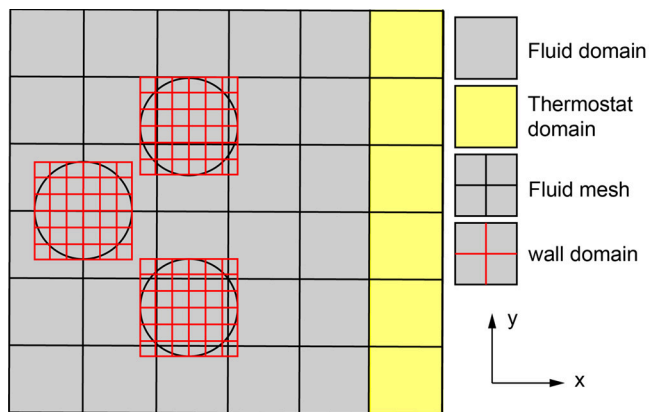
Figure 3.9: Schematic overview of the simulation domain (xy-plane) for catalytic particles with heat effects.

Table 3.1: Parameters for the simulations with surface reactions on catalytic particles (see also Appendix a.1).

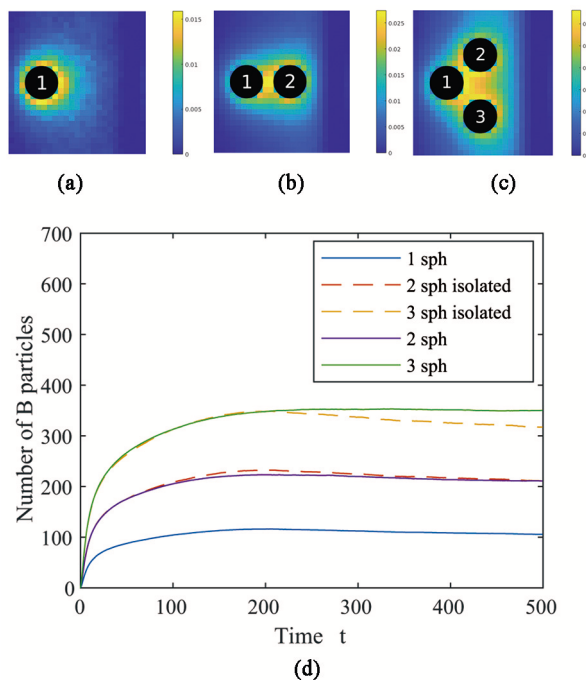| Property	Value	Property	Value
Δt_c	0.5	D	0.6249
α	90º	D_T	0.6653
γ	7	ν	0.3503
p_a^0	0.5	E_a	0.5
p_r^0	0.5	E_r	0.5
p_d^0	0.005	E_d	0.5
N_{cat}	100	Δt_s	0.0005
K_S	10	$\rho_S C_S$	100

Figure 3.10: Mean product number density distribution in a cross section of a domain. Subfigure a, b and c shows results for 1, 2 and 3 spheres. Subfigure d compares the total number of B particles in each of the system with the results expected for multiple isolated spheres.

is biased towards the right due to convection. In the case of multiple spheres, product accumulation happens in the narrow space between spheres, along with the occurrence of hydrodynamic dead-spots. Since the reaction is highly desorption limited, the magnitude of the product number density is smaller than that of the reactant.

Fig. 3.10d shows the evolution of the total number of B particles in the system with time. The three solid lines represent the three different schemes investigated here. The two dashed lines, named '2 sphere isolated' and '3 sphere isolated', are constructed by simply scaling the results for '1 sphere' by the number of spheres in the domain. It can be seen that the qualitative behavior remains the same as the number of spheres is scaled up. However, the relative placement of the 3 spheres can be seen to encourage the entrapment of more product particles in the system, when compared with three independent spheres. This effect can be attributed to the presence of the dead-zone in between the spheres. The particles that reach these dead-zones would have a longer residence time than the rest of the particles, which leads to non-uniformity in the reaction balance within a packed bed.

Each of the scenarios exhibit a quick initial increase, followed by a gradual decrease of the total number of B particles. The initial rise takes place over the first 100 to 200 time

steps, which coincides with the time for the development of the velocity field. At these initial times, the effect of convective transport has not reached a significant value, leading to a diffusion dominated transport of product. Once the convection picks up, the additional particles away from the spheres are gradually forced to the buffer region and converted back to reactant particles, thereby decreasing the total number of product particles.

Fig. 3.11a-c show the steady state fluid temperature distribution surrounding 1, 2 and 3 spheres, respectively, about the plane $z = L_z/2$. Comparing Fig. 3.10 and 3.11, it is seen that the temperature contour follows the same qualitative behavior as the product density profile, while the temperature enhancement penetrates further into the fluid than the product does. This is not caused by the diffusion, since both mass and temperature have similar diffusivity in this case (Table 2.2). Instead, this behavior can be attributed to the difference in flux of mass and energy. The energy generated due to the surface reaction is used to increase the local wall temperature. This energy is then transferred to all the particles hitting that location of the wall. In contrast, only 1 product particle is created per reaction event. This results in a higher flux of heat to the fluid than that of product particles.

Fig. 3.11b and 3.11c demonstrate the effect of dead-spots in the flow profile. The location of the hot-spots coincides with that of the density field, which is as expected. Additionally, a slightly lower temperature can be observed in Fig. 3.11c between spheres 1 and 3 compared to 1 and 2. This can once again be attributed to the effect of slightly higher local velocity, refreshing the mixture with relatively cool fluid. It can also be seen that there is an increase in the magnitude of temperature at the hot-spot with increase in number of spheres. This can be attributed to the presence of more sources and a lower heat transfer coefficient to the bulk fluid due to the restricted flow. Fig. 3.11d shows the temporal variation of local temperature half-way between spheres 2 and 3 (at $x = L_x/2$). It can be seen to follow the same behavior as the total product particle number density. The initial sharp increase is attributed to the diffusion dominated start-up regime, which is followed by a gradual decrease due to the increasing dominance of convection.

Fig. 3.12 shows the temporal evolution of density and temperature in a cross sectional plane at $z = L_z/2$. At $t = 21$, the density and temperature from each of the spheres has started to affect each other. This gradually leads to the formation of a hot-spot, which is seen from the series of figures from $t = 0$ to $t = 97$. This behavior is in line with the observations made in the previous paragraphs. One major observation from this is the difference in time scales for density change and temperature change. In the region between the catalytic spheres, the temperature can reach up to 1.3. This will cause a change in diffusivity, particle density and viscosity. This influence may induce a natural convection effect. However, with a dominant flow driven by a body force g=0.001, we did not observe obvious natural convection in this simulation.
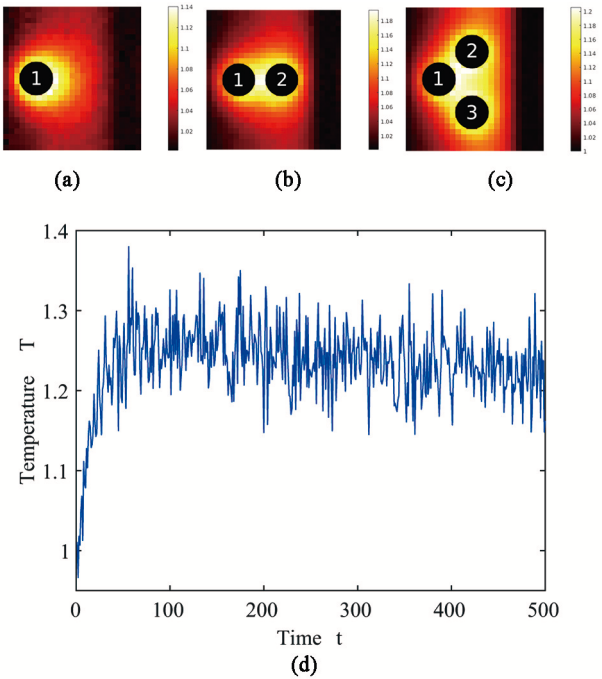
Figure 3.11: Steady state temperature profiles for a cross section of the domain (a-c). Subfigure d gives the transient change in local temperature mid-way between sphere 2 and 3 ($x = 12$ and $y = 14$).
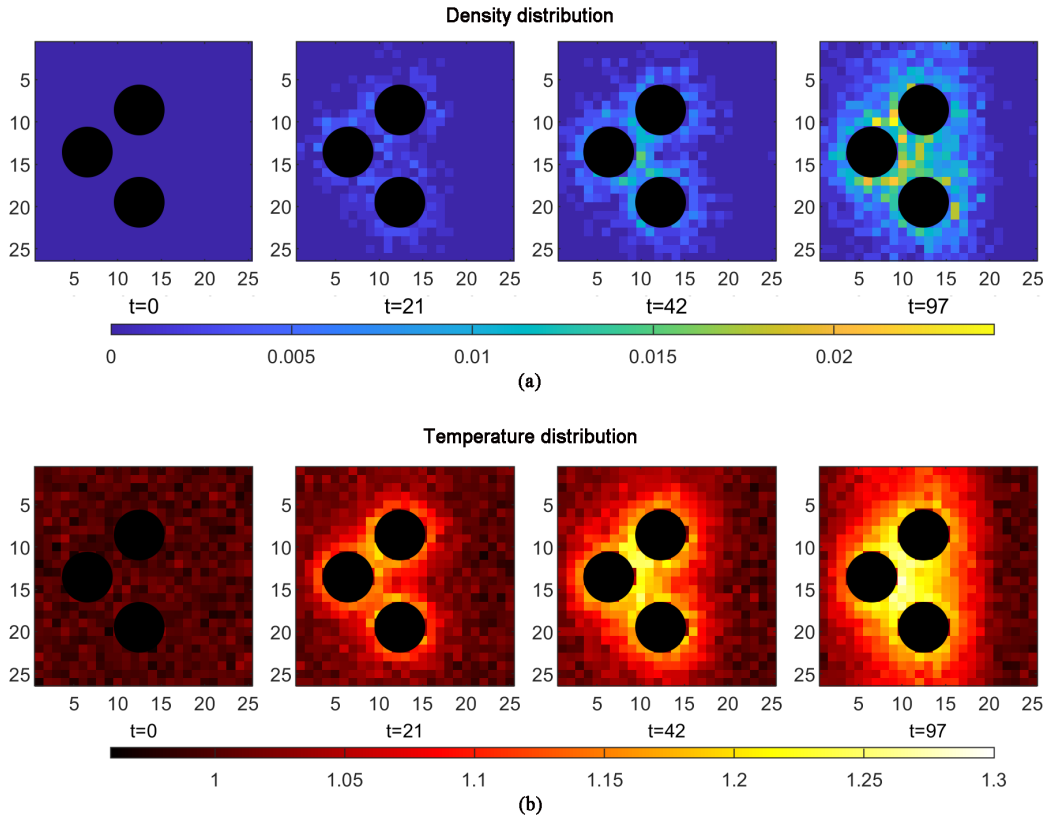
Figure 3.12: Variation of local B number density (a) and temperature (b) in cross section of domain with time.

A final observation from these two graphs is the persistence of noise in the simulations. While 250 simulations are sufficient to observe the major transient behavior in this case, a considerably higher number of ensemble averages is required to resolve smaller temperature variations.

Based on all the above results, it can be concluded that the newly developed techniques (real-time temperature measurement, surface reactions, wall coupling) are capable of working together in synergy to simulate highly complex reactive systems.

3.4   CONCLUSION

In this study, a novel temperature measurement technique for Stochastic Rotation Dynamics was developed, based on kinetic theory. This was then combined with a new form of ensemble averaging to enable real-time measurement of temperature. A proper boundary condition is applied to achieve an accurate constant-temperature no-slip boundary condition. The real-time temperature change due to chemical reaction and heat transfer in fluid phase is achieved and measured.

The newly formulated non-isothermal model was coupled with a temperature conduction equation that can model the formation of complex surface temperature patterns. The coupled method was applied to model surface reactions on catalytic particles. A SRD approach was adopted to model the adsorption, where the SRD particles have a temperature dependent probability to adsorb onto the limited number of active sites on the surface. The adsorbed particles then react with a rate that depends on the local wall temperature. A wall temperature dependent desorption model was used to release the products into the fluid. This reaction model was validated against theoretical predictions.

Finally, the combined model was applied to simulate a flow past catalytic spheres. The obtained results highlight the capability of the model to simultaneously solve for the transient evolution of macroscopic properties such as mean velocity, temperature and density, along with employing accurate wall reaction mechanisms. This expansion of the SRD method to transient and non-isothermal simulations enables the use of this method for the study of highly non-linear and transient mesoscale problems.

REFERENCES

[1] J Mareš. "On the development of the temperature concept." In: *Journal of thermal analysis and calorimetry* 60.3 (2000), pp. 1081–1091.

[2] William Thomson Baron Kelvin. *Mathematical and Physical Papers: 1841-1890*. Vol. 3. Cambridge University Press, 1890.

[3] Xiaogang Deng, Meiliang Mao, Guohua Tu, Hanxin Zhang, and Yifeng Zhang. "High-order and high accurate CFD methods and their applications for complex grid problems." In: *Communications in Computational Physics* 11.4 (2012), pp. 1081–1102.

[4] Anatoly Malevanets and Raymond Kapral. "Mesoscopic model for solvent dynamics." In: *The Journal of chemical physics* 110.17 (1999), pp. 8605–8613.

[5] G Gompper, T Ihle, DM Kroll, and RG Winkler. "Multi-particle collision dynamics: A particle-based mesoscale simulation approach to the hydrodynamics of complex fluids." In: *Advanced computer simulation approaches for soft matter sciences III*. Springer, 2009, pp. 1–87.

[6] T Ihle and DM Kroll. "Stochastic rotation dynamics: A Galilean-invariant mesoscopic model for fluid flow." In: *Physical Review E* 63.2 (2001), p. 020201.

[7] Zhen-Yue Yang, Xiao-Fei Tian, Li-Jun Liu, and Ji-Zhong Chen. "Role of hydrodynamic interactions in the deformation of star polymers in poiseuille flow." In: *Chinese Journal of Polymer Science* 38.4 (2020), pp. 363–370.

[8] Martin Wagner and Marisol Ripoll. "Solvent-induced depletion interactions in multiparticle collision dynamic simulations." In: *International Journal of Modern Physics C* 30.10 (2019), p. 1941008.

[9] Maud Formanek and Angel J Moreno. "Single-chain nanoparticles under homogeneous shear flow." In: *Macromolecules* 52.4 (2019), pp. 1821–1831.

[10] Antonio Lamura and Roland G Winkler. "Tethered Semiflexible Polymer under Large Amplitude Oscillatory Shear." In: *Polymers* 11.4 (2019), p. 737.

[11] Chien-Cheng Huang, Roland G Winkler, Godehard Sutmann, and Gerhard Gompper. "Semidilute polymer solutions at equilibrium and under shear flow." In: *Macromolecules* 43.23 (2010), pp. 10107–10116.

[12] Raghunath Chelakkot, Roland G Winkler, and Gerhard Gompper. "Migration of semiflexible polymers in microcapillary flow." In: *EPL (Europhysics Letters)* 91.1 (2010), p. 14001.

[13]   Dagmar Steinhauser, Sarah Köster, and Thomas Pfohl. "Mobility gradient induces cross-streamline migration of semiflexible polymers." In: *ACS Macro Letters* 1.5 (2012), pp. 541–545.

[14]   L Cannavacciuolo, RG Winkler, and G Gompper. "Mesoscale simulations of polymer dynamics in microchannel flows." In: *EPL (Europhysics Letters)* 83.3 (2008), p. 34007.

[15]   JT Padding and AA Louis. "Hydrodynamic interactions and Brownian forces in colloidal suspensions: Coarse-graining over time and length scales." In: *Physical Review E* 74.3 (2006), p. 031402.

[16]   A Malevanets and JM Yeomans. "Dynamics of short polymer chains in solution." In: *EPL (Europhysics Letters)* 52.2 (2000), p. 231.

[17]   JT Padding and AA Louis. "Hydrodynamic and Brownian fluctuations in sedimenting suspensions." In: *Physical review letters* 93.22 (2004), p. 220601.

[18]   Adam Wysocki, C Patrick Royall, Roland G Winkler, Gerhard Gompper, Hajime Tanaka, Alfons van Blaaderen, and Hartmut Löwen. "Direct observation of hydrodynamic instabilities in a driven non-uniform colloidal dispersion." In: *Soft Matter* 5.7 (2009), pp. 1340–1344.

[19]   Ingo O Götze and Gerhard Gompper. "Mesoscale simulations of hydrodynamic squirmer interactions." In: *Physical Review E* 82.4 (2010), p. 041921.

[20]   Gunnar Rückner and Raymond Kapral. "Chemically powered nanodimers." In: *Physical review letters* 98.15 (2007), p. 150603.

[21]   J Liam McWhirter, Hiroshi Noguchi, and Gerhard Gompper. "Flow-induced clustering and alignment of vesicles and red blood cells in microcapillaries." In: *Proceedings of the National Academy of Sciences* 106.15 (2009), pp. 6039–6043.

[22]   Mingcheng Yang and Marisol Ripoll. "Simulations of thermophoretic nanoswimmers." In: *Physical Review E* 84.6 (2011), p. 061401.

[23]   Kai Qi, Elmar Westphal, Gerhard Gompper, and Roland G Winkler. "Enhanced rotational motion of spherical squirmer in polymer solutions." In: *Physical review letters* 124.6 (2020), p. 068001.

[24]   Jan-Timm Kuhr, Felix Rühle, and Holger Stark. "Collective dynamics in a monolayer of squirmers confined to a boundary by gravity." In: *Soft Matter* 15.28 (2019), pp. 5685–5694.

[25]   Andreas Zöttl and Holger Stark. "Simulating squirmers with multiparticle collision dynamics." In: *The European Physical Journal E* 41.5 (2018), p. 61.

CHAPTER 3

[26]   Yu-Guo Tao, Ingo O Götze, and Gerhard Gompper. "Multiparticle collision dynamics modeling of viscoelastic fluids." In: *The Journal of chemical physics* 128.14 (2008), p. 144902.

[27]   Shichen Ji, Run Jiang, Roland G Winkler, and Gerhard Gompper. "Mesoscale hydrodynamic modeling of a colloid in shear-thinning viscoelastic fluids under shear flow." In: *The Journal of chemical physics* 135.13 (2011), p. 134116.

[28]   Bartosz Kowalik and Roland G Winkler. "Multiparticle collision dynamics simulations of viscoelastic fluids: Shear-thinning Gaussian dumbbells." In: *The Journal of chemical physics* 138.10 (2013), p. 104903.

[29]   S Mahdiyeh Mousavi, Gerhard Gompper, and Roland G Winkler. "Wall entrapment of peritrichous bacteria: a mesoscale hydrodynamics simulation study." In: *Soft matter* 16.20 (2020), pp. 4866–4875.

[30]   Swapnil C Kohale and Rajesh Khare. "Cross stream chain migration in nanofluidic channels: Effects of chain length, channel height, and chain concentration." In: *The Journal of chemical physics* 130.10 (2009), p. 104904.

[31]   Richard M Jendrejack, Eileen T Dimalanta, David C Schwartz, Michael D Graham, and Juan J de Pablo. "DNA dynamics in a microchannel." In: *Physical review letters* 91.3 (2003), p. 038102.

[32]   Allen P Minton. "How can biochemical reactions within cells differ from those in test tubes?" In: *Journal of cell science* 119.14 (2006), pp. 2863–2869.

[33]   Gernot Guigas, Claudia Kalla, and Matthias Weiss. "The degree of macromolecular crowding in the cytoplasm and nucleoplasm of mammalian cells is conserved." In: *FEBS letters* 581.26 (2007), pp. 5094–5098.

[34]   Raymond Kapral. "Multiparticle Collision Dynamics: Simulation of Complex Systems on Mesoscales." In: *Advances in Chemical Physics* 140 (2008), pp. 89–146.

[35]   E Allahyarov and G Gompper. "Mesoscopic solvent simulations: Multiparticle-collision dynamics of three-dimensional flows." In: *Physical Review E* 66.3 (2002), p. 036702.

[36]   Stefano Lepri, Guido Ciraolo, Pierfrancesco Di Cintio, Jamie Gunn, and Roberto Livi. "Kinetic and hydrodynamic regimes in multi-particle-collision dynamics of a one-dimensional fluid with thermal walls." In: *Physical Review Research* 3.1 (2021), p. 013207.

[37]   Alan Sam, Sridhar Kumar Kannam, Remco Hartkamp, and Sarith P. Sathian. "Water flow in carbon nanotubes: The effect of tube flexibility and thermostat." In: *The Journal of Chemical Physics* 146.23 (2017), p. 234701. DOI: 10.1063/1.4985252. URL: http://aip.scitation.org/doi/10.1063/1.4985252.

CHAPTER 3

[38]   Michael P Howard, Athanassios Z Panagiotopoulos, and Arash Nikoubashman. "Efficient mesoscale hydrodynamics: Multiparticle collision dynamics with massively parallel GPU acceleration." In: *Computer Physics Communications* 230 (2018), pp. 10–20.

[39]   Sebastian Muehlbauer, Severin Strobl, Matthew Coleman, and Thorsten Poeschel. "Simulation of catalytic reactions in open-cell foam structures." In: *arXiv preprint arXiv:2010.03904* (2020).

[40]   Juan D Olarte-Plata and Fernando Bresme. "Microscopic relationship between colloid–colloid interactions and the rheological behaviour of suspensions: a molecular dynamics-stochastic rotation dynamics investigation." In: *Molecular physics* 116.15-16 (2018), pp. 2032–2040.

[41]   Dan S Bolintineanu, Jeremy B Lechman, Steven J Plimpton, and Gary S Grest. "No-slip boundary conditions and forced flow in multiparticle collision dynamics." In: *Physical Review E* 86.6 (2012), p. 066703.

[42]   E Tüzel, Thomas Ihle, and Daniel M Kroll. "Dynamic correlations in stochastic rotation dynamics." In: *Physical Review E* 74.5 (2006), p. 056702.

[43]   T Ihle and DM Kroll. "Stochastic rotation dynamics. II. Transport coefficients, numerics, and long-time tails." In: *Physical Review E* 67.6 (2003), p. 066706.

[44]   MH Ernst, EH Hauge, and JMJ Van Leeuwen. "Asymptotic time behavior of correlation functions." In: *Physical Review Letters* 25.18 (1970), p. 1254.

[45]   MH Ernst, EH Hauge, and JMJ Van Leeuwen. "Asymptotic time behavior of correlation functions. I. Kinetic terms." In: *Physical Review A* 4.5 (1971), p. 2055.

[46]   CM Pooley and JM Yeomans. "Kinetic theory derivation of the transport coefficients of stochastic rotation dynamics." In: *The Journal of Physical Chemistry B* 109.14 (2005), pp. 6505–6513.

[47]   Thomas Ihle, E Tüzel, and Daniel M Kroll. "Equilibrium calculation of transport coefficients for a fluid-particle model." In: *Physical Review E* 72.4 (2005), p. 046707.

[48]   A Sengar, JAM Kuipers, Rutger A Van Santen, and JT Padding. "Particle-based modeling of heterogeneous chemical kinetics including mass transfer." In: *Physical Review E* 96.2 (2017), p. 022115.

4

SURFACE REACTION AND ISLAND FORMATION

4.1 INTRODUCTION

Most implementations of chemical reactions in SRD are homogeneous reactions [1, 2] or surface reactions with neglect of some processes such as adsorption, surface diffusion, or desorption through the use of mean-field rate expressions [3, 4]. Models of colloidal particles propelled by chemical reactions with adsorption-desorption kinetics such as diffusiophoretic Janus colloids and bi-particle catalytic reactions have been described before.[5–10] However, these works do not describe the detailed kinetics of changing catalyst sites. Sengar et al. were the first to incorporate a Langmuir Hinshelwood reaction kinetics by introducing individual steps like adsorption, desorption and surface reactions for a pseudo reaction A → B.[11, 12] It has been shown that SRD can simulate heterogeneously catalyzed systems and interlink surface and bulk phenomena which can occur at different time scales. In addition, the influence of the porous catalyst structure has also been investigated through this method [13]. For realistic catalytic reactions, more complex mechanisms exist, such as multiple elementary reaction steps or 'island formation' caused by interactions of surface particles, which lead to deviations from mean-field predictions [14, 15].

In this work, we show for the first time how to model more complex heterogeneous catalytic reactions by coupling an SRD fluid to a catalytic surface on which surface reactions are explicitly modelled. This paper is arranged as follows. In section 4.2, we provide a theoretical background of SRD for modelling hydrodynamics and heterogeneous surface reactions with different mechanism, including adsorption, particle interaction and desorption. In section 4.3, we validate the simulation method for different cases of surface reactions with mean-field assumptions and for the surface interactions of species when the mean-field assumptions break. Then, a three-step reaction mechanism with reactant
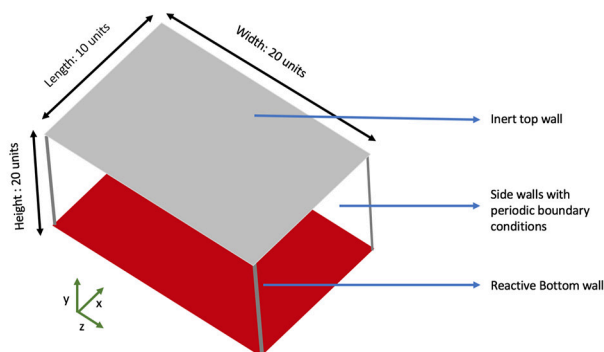
Figure 4.1: Schematic of the simulation setup. Periodic boundary conditions are employed for the sides whilst the top (inert) and bottom (reactive) surfaces are solid walls.

dissociation after adsorption is investigated to demonstrate the capability of the method when simulating more complex reaction mechanisms where mean-field assumptions fail. Finally, in section 4.4 we give our conclusions and outlook.

4.2   METHOD

4.2.1   FLUID MODEL AND SIMULATION SETUP

Fig. 4.1 shows the simulation setup. In this geometry, the top and bottom surfaces are solid and the sides of the domain are periodic. The bottom wall is reactive (boundary condition depends on the reaction that is simulated), whilst the top wall has a no flux boundary with respect to concentration (inert wall). An adjusted stochastic boundary condition [16, 17] is applied on the reactive surface in order to account for particle adsorption/desorption. In this work, these events happen during the streaming step. Particles colliding with the wall have a probability of adsorbing. Once adsorbed, the particle remains adsorbed, reacts or desorbs based on a probability. The reactive wall is divided into lattice grids. Each grid represents a catalyst site, which is occupied when a particle is absorbed.

The choice of basic units is shown in Table 2.1. The choice of simulation parameters in this work are streaming time interval (Δt_s) as 0.1, collision time interval (Δt_c) as 1, collision angle (α) as $\pi/2$ and average particle density per cell (γ) as 25. This high particle density is chosen in consideration of obtaining smooth concentration profiles.

4.2.2   REACTION SCHEME

A typical heterogeneous reaction involves the adsorption of the reactant on the catalyst surface, breaking of one or more chemical bonds, formation of new bonds, and finally the desorption of the product. Owing to the coarse grained nature of mesoscopic simulations, heterogeneous chemical reactions can be simplified using random adsorption and desorption events and reactions in steps, as explained in the following.

4.2.2.1   *Adsorption, Reaction and Desorption*

In this hybrid model, adsorption, reaction and desorption are taken into account explicitly and updated every streaming time-step (Δt_s). The implementation of the adsorption and desorption method is discussed in detail in our previous work [17]. When a particle collides with the wall, the adsorption site closest to the collision point is checked, if this site is vacant, the particle may adsorb with probability P_{ads}. Every Δt_s, the adsorbed particles are also updated for reaction. For a simple A $\rightarrow$ B reaction, a probability test (with a reaction probability P_{re}) is carried out. If the probability test is successful, A will convert to B. For simple first order reactions, the reaction rate does not depend on the surrounding of the particle. However, bi-particle elementary particles are treated differently for mean-field and non-mean-field reactions. For a mean-field A + B $\rightarrow$ C reaction, for every adsorbed particle A, a random catalyst site is picked on the wall, if the random site is of type B, a reaction may occur with a probability P_{re}. If the reaction occurs, one of the reactants turns to a type C, while the other reactant site becomes vacant. Note that for reactions involving two different species, only one of the adsorbed species is checked for the reaction. In case of non-mean-field reactions, a particle can only react with its (first and second closest) neighboring particles, and surface diffusion (including possible surface interactions) are modelled explicitly. The details for non-mean-field implementation can be found in the next subsection on surface interactions. For the desorption of the species from the wall, a test with desorption probability P_{des} is carried out. If the probability test is successful, the particle is given a velocity based on a Maxwell-Boltzmann distribution and reintroduced into the bulk. For cases in which there is a bulk flow, the velocity distribution would need to be adjusted to obtain correct flow profiles. The choice for the distributions and their validation is described in detail in our previous work [17].

To validate the simulation results obtained from SRD, it is necessary to be able to convert probabilities for adsorption, reaction and desorption into rate constants that can be used in continuum numerical models. To relate the adsorption rate constant to simulation parameters, first a relation needs to be found for the particle collision frequency (Z) with the adsorbing wall.

$$Z = \frac{1}{2}\frac{N}{V}\langle|v_y|\rangle \tag{4.1}$$

As shown in Eq. (4.1), the collision frequency can be expressed in terms of the particle concentration ($C_s = N/V$) and the average velocity in the y-direction, which is perpendicular to the wall, $\langle |v_y| \rangle = \sqrt{2k_bT/(\pi m)}$ [11].

Not every collision leads to adsorption and in order to calculate the rate of particle adsorption R_{ads}, the adsorption probability P_{ads} and the fraction of unoccupied catalyst sites θ_v needs to be considered. Therefore, based on SRD parameters, the rate of adsorption can be expressed as:

$$R_{ads} = P_{ads}Z\theta_v = C_sP_{ads}\theta_v\sqrt{\frac{k_bT}{2\pi m}}. \tag{4.2}$$

The rate of adsorption can also be calculated using a mean-field expression involving the adsorption rate constant (k_{ads}):

$$R_{ads} = k_{ads}C_s\theta_v\frac{N_{cat}}{A_{cat}}, \tag{4.3}$$

where A_{cat} represents the catalytic surface area and N_{cat} is the number of catalyst sites. An expression for k_{ads} can be obtained by combining Eqs. (4.2) and (4.3):

$$k_{ads} = \sqrt{\frac{k_bT}{2\pi m}}\frac{P_{ads}A_{cat}}{N_{cat}}. \tag{4.4}$$

A similar approach can be used to relate the desorption and first-order reaction rate constants to simulation parameters. Given an example of a first-order reaction $A \rightarrow B$, the rate constant is given by:

$$k_{re} = \frac{\ln(1-P_{re})}{\Delta t_s}, \tag{4.5}$$

in which P_{re} represents the probability for reaction. Analogously, the desorption rate constant of product particle B can be expressed as

$$k_{des} = \frac{\ln(1-P_{des})}{\Delta t_s}, \tag{4.6}$$

where P_{des} is the probability for the desorption of a B particle in a time interval Δt_s.

4.2.2.2   Surface interactions

The reaction expression with mean-field assumption has been derived in the previous section. Here, we discuss the case in which the mean-field assumption breaks down.

The mean-field approximation is a commonly made assumption to turn a many-body problem into a single-body problem [18], to reduce the complexity and computational cost of solving a system. However, the mean-field assumption is not always reasonable, for it is limited to cases in which no inter-species interactions exist and where the rate of surface diffusion is large, such that all species instantaneously adopt an even distribution over the surface. To simulate surface interactions of particles and their possible separation into 'islands' of different species, we use mesoscopic Monte Carlo simulation. Interactions between neighboring adsorbed particles are accounted for in an explicit manner by changes to the potential energy of the adsorbed particles [19]. To fit the Monte Carlo step in SRD time steps, surface mobilities are assumed to be large enough to maintain a local equilibrium on the surface.

The catalytic surface is divided into a surface lattice grid. The size, shape and orientation of this surface lattice grid can be chosen depending on the specific problem at hand, independently of the size and orientation of the cubic SRD grid. For convenience, in the simulations presented here, the catalytic surface is divided into a square lattice aligned with the SRD grid, in which each particle can interact with its first and second nearest neighbors. The division of the surface into a square grid leads to fixed catalyst sites. Although this simplified setting does not allow for the occurrence of complex kinetics such as surface reconstruction, it can be extended to study a variety of reactions in which surface interactions are prevalent. An example includes the adsorption and dissociation of oxygen in Pt(111) which is influenced by nearby chemisorbed species.[20–23] The main focus of this work is to give an example of coupling the fluid phase to the surface reaction phenomena by implementation of non-mean field effects in SRD, something which is not available with most kinetic Monte Carlo simulations. The distance between two neighboring surface sites is set to $b_0 = a_0/4$, with a_0 corresponding to one SRD cell, such that there are 16 catalyst sites per a_0^2. In this mesoscopic Monte Carlo simulation, a similar procedure as the metropolis algorithm is used. The Monte Carlo steps occur 5 times per each adsorbed particle every streaming time-step (Δt_s). In each Monte Carlo step, a random particle may move to one of its four closest neighboring lattice cells provided that it meets certain requirements. A move is directly accepted if the particle in the new position leads to a lower potential energy. Otherwise, the move may still be accepted with a probability of $P_{acc} = \exp(-(E_{after} - E_{before})/(k_B T))$. To implement this, a uniform random number between 0 and 1 is picked and the move is accepted if this number is lower than P_{acc}. If only repulsive interactions between different species are considered, then the following expression can be used to calculate the total energy:
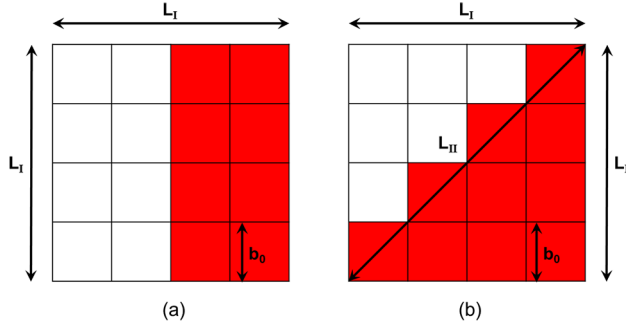
Figure 4.2: Straight (a) and slanted (b) boundaries that can form between two different species. "b_0" refers to the unit square lattice size, L_1 is the boundary length (between the red and white species) of configuration 1 and is equal to side length of the square lattice. L_2 is equal to the boundary length of configuration 2.

$$E = \frac{E_0}{2} \sum_{i=1}^{N_{ads}} \sum_{j \in Z_{i,1}} (1 - \delta(s_i - s_j))$$

$$+ \frac{E_1}{2} \sum_{i=1}^{N_{ads}} \sum_{j \in Z_{i,2}} (1 - \delta(s_i - s_j))$$

(4.7)

In this expression, E_0 and E_1 are the first and second nearest neighbor repulsive pair interactions between two adsorbed particles of different species. N_{ads} is the total number of particles adsorbed on the wall while $Z_{i,1}$ and $Z_{i,2}$ refer to the first and second neighbor list for particle i. $\delta(s_i - s_j)$ is the Dirac delta function, which is equal to 1 when the type of the species on the wall (denoted with s_i and s_j) are equal to each other and 0 otherwise. Another condition that is placed on the particle movement is that it can only enter a new site if that site is unoccupied. This mimics the fact that particle movement becomes limited when the catalyst sites are nearly all occupied.

The choice of which neighbor interactions to account for when calculating the potential energy can be important in determining the shape of the boundaries formed between two different species on the surface. Square lattices, taking into account only the four nearest neighbors, lead to the formation of square boundaries, which does not adequately represent the shape of most real phase-separated domains. As shown in Fig. 4.2, if interspecies interactions are assumed to be unfavorable (positive energetic contribution), then by only counting the nearest neighbor interactions, the energy (E_1) of a straight line boundary (configuration 1) per boundary length (L_1) is equal to $\frac{E_1}{L_1} = \frac{E_0}{b_0}$. In this expression, E_0 refers to the nearest neighbor interspecies interaction and b_0 is the square lattice unit size. Meanwhile, the energy for configuration 2 per unit length of the boundary is given by

$\frac{E_2}{L_2} = \frac{2E_0}{\sqrt{2}b_0} = \frac{\sqrt{2}E_0}{b_0}$. To enable more isotropic growth of the boundaries, both configuration 1 and 2 need to become equally favorable. This can be achieved by also taking into account the second nearest neighbor interactions (denoted by E_1) [19]. In that case, the energy of configuration 1 and 2 per unit length of the boundaries can be expressed by:

$$\frac{E_1}{L_1} = \frac{E_0 + 2E_1}{b_0} \tag{4.8}$$

$$\frac{E_2}{L_2} = \frac{2E_0 + E_1}{\sqrt{2}b_0} \tag{4.9}$$

The two expressions (energy per unit length) are equal if the following ratio is chosen between E_1 and E_0:

$$\frac{E_1}{E_0} = \frac{\sqrt{2}-1}{2-\sqrt{2}} = \frac{1}{\sqrt{2}} \tag{4.10}$$

4.3 VALIDATION AND RESULTS

In our previous work [17], we validated the adjusted stochastic boundary condition leading to thermostatting walls with a very small slip velocity in the case of convective flow. Since the present work focuses on simulating surface reactions with SRD, here we validate the method for Langmuir kinetic reactions and more complex reactions in a reactor without flow.

4.3.1 FIRST-ORDER SURFACE REACTION

In this section, a simple Langmuir kinetic model will be investigated. In the simulation, a particle of type A can adsorb on the wall with a probability $P_{ads} = 0.20$ (corresponding to $k_{ads} = 0.08a_0^3t_0^{-1}$) and can also react to become type B ($P_{re} = 0.01$ leading to $k_{re} = 0.1t_0^{-1}$) and desorb ($P_{des} = 0.01$, leading to $k_{des} = 0.1t_0^{-1}$). Species B can also adsorb and desorb from the wall with the same probabilities as species A. The reaction kinetics is expressed by:

$$A + * <=> A * -> B * <=> B + * \tag{4.11}$$
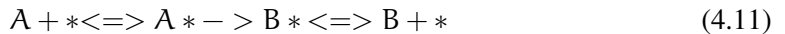
where * refers to a vacant site on the surface and A* refers to a surface site on the wall occupied by species A (the same nomenclature applies to species B and B*). This simulation allows for the validation of the adsorption-reaction-desorption implementation in the

SRD code. In terms of mean-field equations, the rate of change of surface coverage of A and B can be expressed as:

$$\frac{d\theta_A}{dt} = k_{ads,A}\theta_V\gamma(t)x_A(y=0,t) \tag{4.12}$$
$$-k_{re}\theta_A - k_{des,A}\theta_A$$

$$\frac{d\theta_B}{dt} = k_{ads,B}\theta_V\gamma(t)x_B(y=0,t) \tag{4.13}$$
$$+k_{re}\theta_A - k_{des,B}\theta_B.$$

where $x_A(y=0,t)$ is the local mole fraction of species A in the fluid near the catalytic surface located at $y=0$ and $\gamma(t)$ is the number density of particles in the fluid. θ_A, θ_B and θ_V are the surface coverage of particle A, B and vacant sites, respectively. The adsorption rate depends on the collision frequency of particle A, which is influenced by the mole fraction of A ($x_A(y=0,t)$) in the fluid and the number density $\gamma(t)$ of particles in the fluid. When the simulation starts ($t=0$), at the surface, the initial condition of fraction of particle A, B and vacant site are $\theta_A=0$, $\theta_B=0$, $\theta_V=1$. A continuum numerical model is used to validate the simulation by solving the unsteady diffusion equation for each species i in the fluid:

$$\frac{dC_i}{dt} = D_i\frac{d^2C_i}{dy^2} \tag{4.14}$$

with boundary conditions taking into account the rates of adsorption and desorption as shown in Eqs. (S3) in Appendix b.1. Here C_i represents the concentration of species i in the fluid, which can be obtained by multiplying the particle number density $\gamma(t)$ by the local mole fraction x_i, and D_i the diffusion coefficient of species i. In the numerical code, $\gamma(t)$ is assumed to be independent of local variations and the number of particles that adsorb to or desorb from the surface (or are reduced/added due to reaction) and are spread homogeneously over the SRD cell. This assumption is justified by the low adsorption probabilities that are used (all below 0.20) coupled with the large number of particles (100,000 particles in total) with respect to the number of catalyst sites (3200). For large adsorption/desorption probabilities, and low particle number densities, the local variations of local particle number densities may lead to advection effects. SRD may be capable of including these effects, however the study of these systems is beyond the scope of this work and is encouraged for further research. In the numerical model, the governing equation Eq. (4.14) is discretized using a finite volume scheme. The details of the numerical model are given in Appendix b.1.

The numerical and simulation results for the concentration profile after $10t_0$ is depicted in Fig. 4.3(a), along with the vacancy fraction as a function of time in Fig. 4.3(b). An excellent agreement is observed between the SRD simulation results for both the concentration profile in the bulk and for the vacancy fraction at the wall. Only small reaction rates are
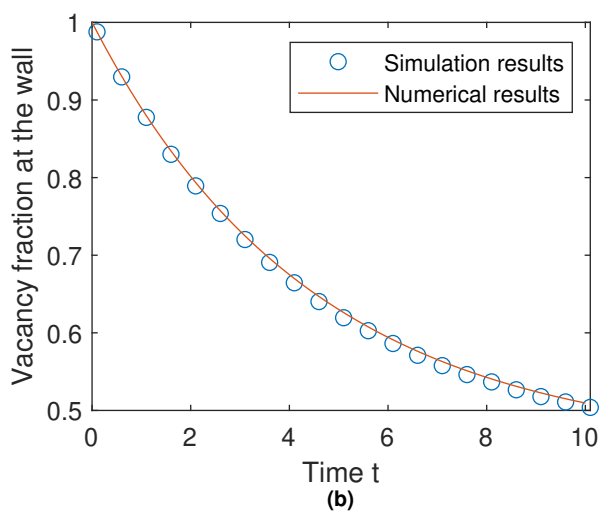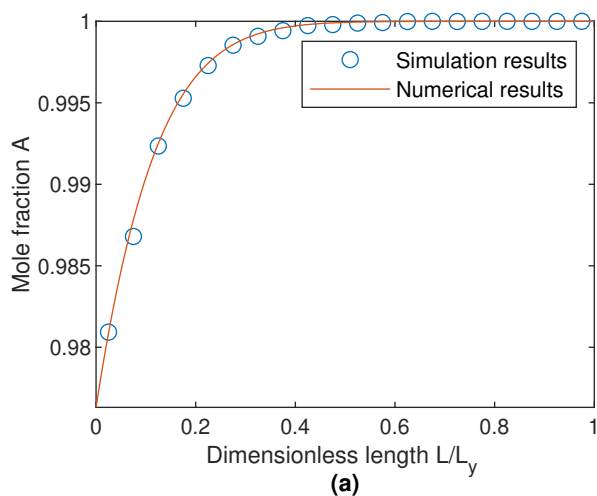
Figure 4.3: First-order mean-field surface reaction. (a) Concentration profile at a cross-section of an infinite channel. (b) Vacancy fraction on the reactive wall shown as function of time.

considered in this section to ensure that the concentration gradients near the reactive wall are small. Large concentration gradients will require a more elaborate expression for the mean-field adsorption rate constant, which is beyond the scope of this work (see Appendix b.1 for more explanation on the numerical scheme for validation).

4.3.2   BI-PARTICLE REACTIONS

Before simulating complex reaction mechanisms, it is necessary to be able to simulate bi-particle elementary reaction steps on the catalytic surface. In this section, bi-particle reactions $A + B \rightarrow C$ and $A + * \leftrightarrow 2B$ are simulated under the mean-field assumption and validated using numerical models. In order to use numerical validations, the rate constant of bi-particle reactions needs to be expressed in terms of simulation parameters (such as the probability of reaction). This calculation is done for a $A + B \rightarrow C$ reaction as a test case, but the results can be generalized for other bi-particle reactions.

Assuming that at a given time step there is no adsorption/desorption occurring concurrently, the rate of change of the number of catalyst sites occupied by species A and B over time can be described by Eqs. (4.15-4.16) using the mean-field assumption.

$$\frac{d\rho_{S,A_i}}{dt} = -k_{r,AB}\rho_{S,A_i}\rho_{S,B_i} \tag{4.15}$$

$$\frac{d\rho_{S,B_i}}{dt} = -k_{r,AB}\rho_{S,A_i}\rho_{S,B_i} \tag{4.16}$$

In these expressions, S, A_i, ρ_{S,B_i} and $k_{r,AB}$ refers to the total number of sites occupied per area of catalyst by species A, B and the reaction rate constant in the mean-field model respectively. A Taylor series expansion can be made to find an approximate expression for ρ_{S,A_i} and ρ_{S,B_i} calculated with their number density in the previous time step ($\rho_{S,A_{i-1}}$, $\rho_{S,B_{i-1}}$):

$$\rho_{S,A_i} \approx \rho_{S,A_{i-1}} + \frac{d\rho_{S,A_i}}{dt}\Delta t_s, \tag{4.17}$$

$$\frac{\rho_{S,A_i}}{\rho_{S,A_{i-1}}} \approx 1 - k_{r,AB}\rho_{S,B_{i-1}}\Delta t_s. \tag{4.18}$$

In terms of simulation parameters and given the implementation of the bi-molecular surface reactions, the fraction $\frac{\rho_{S,A}}{\rho_{S,A_{i-1}}}$ can be expressed as:

$$\frac{N_A}{N_{A_{i-1}}} = \frac{\rho_{S,A_i}}{\rho_{S,A_{i-1}}} = 1 - P_{re,AB}\theta_{B_{i-1}} \tag{4.19}$$

where $P_{re,AB}$ refers to the probability of the reaction and θ_B is the fraction of sites occupied by particle B ($\theta_B = A_{cat}\rho_{S,B}/N_{cat}$). The reaction rate constant of $A + B \rightarrow C$ can be inferred by combining Eqs. (4.18) and Eqs. (4.19) as follows:

$$k_{r,AB} = \frac{A_{cat}P_{re,AB}}{N_{cat}\Delta t_s} \tag{4.20}$$

The expression of maximum error (Er) associated with Eq. (4.18) can be calculated from the second derivative of ρ_A with respect to time (see Appendix b.2). Using this reaction rate constant, the mean-field expressions for the change of fraction occupied by A, B, C can be calculated:

$$\frac{d\theta_A}{dt} = k_{ads,A}\theta_V\gamma(t)x_A(y=0,t)$$
$$-k_{des,A}\theta_A - \frac{k_{r,AB}N_{cat}}{A_{cat}}\theta_A\theta_B \tag{4.21}$$

$$\frac{d\theta_B}{dt} = k_{ads,B}\theta_V\gamma(t)x_A(y=0,t)$$
$$-k_{des,B}\theta_B - \frac{k_{r,AB}N_{cat}}{A_{cat}}\theta_A\theta_B \tag{4.22}$$

$$\frac{d\theta_C}{dt} = k_{ads,C}\theta_V\gamma(t)x_A(y=0,t)$$
$$-k_{des,C}\theta_C + \frac{k_{r,AB}N_{cat}}{A_{cat}}\theta_A\theta_B \tag{4.23}$$

where γ and x_A represent the number density of the fluid and the mole fraction of species A in the fluid. At time $t = 0$, the reaction is catalyzed on the wall at $y = 0$. The initial mixture consists of reactants A and B in equal amounts. The masses of A and B particles are set to $1\ m_0$ and the mass of C is set to $2\ m_0$. Considering that the mass of the product is different, it implies that it has a different self-diffusion coefficient than the reactants (see Table 2.2). To simplify the validation test case, it is ensured that the production rate is low ($P_{ads,A} = 0.05$ corresponding to $k_{ads,A} = 0.00125$ and $P_{des,A} = 0.0001$ corresponding to $k_{des,A} = 0.001$). This implies that the influence of the C species on the diffusivities in the bulk can be ignored for the time-scales considered in this simulation. In this validation case, the same probability of desorption and adsorption is used for every species involved. Therefore, in this case $k_{des,A} = k_{des,B} = k_{des,C}$. As the mass of species C is set as twice that of the reactants, $k_{ads,A} = k_{ads,B} = \sqrt{2}k_{ads,C}$. Eqs. (4.21-4.23) are coupled to the numerical equations shown in Appendix b.1 to find the evolution of mole fractions $x_A(y,t)$, $x_B(y,t)$, $x_C(y,t)$ and number density $\gamma(t)$. $k_{r,AB}$ is calculated with Eq. (4.20) derived previously.

The very good agreement between the numerical and simulation results in Fig. 4.4 confirms the validity of the expression found for $k_{r,AB}$. Consistent with the error expression
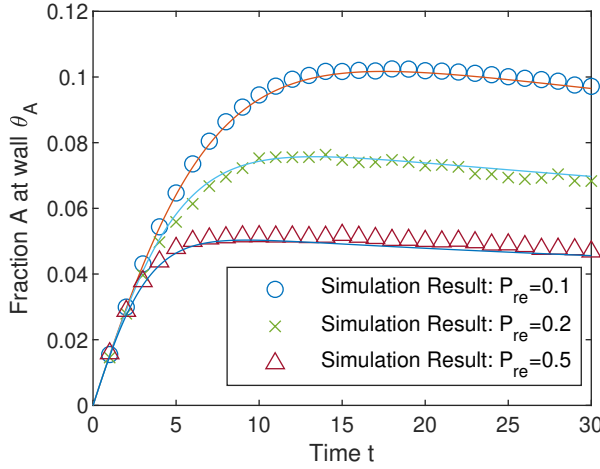
Figure 4.4: Simulation results (symbols) and continuum numerical results (lines) for a mean-field bi-particle reaction $A + B \rightarrow C$ for different reaction probabilities (0.1, 0.2 and 0.5).

in Appendix b.2, the best agreement is found for the lowest reaction probabilities, 0.1 and 0.2. The error for the $k_{r,AB}$ expression is shown in Appendix b.2 to scale with the square of the reaction probability ($P_{re,AB}$). In order to simulate reactions with higher reaction rate constants it is therefore advised to lower the time-step Δt_s. This means that the catalyst sites on the wall are updated more frequently and thereby lower reaction probabilities can be used to obtain the same reaction rates.

Another validation test is done with a reversible reaction: $A + * \leftrightarrow 2B$. At the start of the reaction, the solution only contains particles of type A ($x_A = 1$). To conserve mass, the mass of A is set to 2 ($m_A = 2$) and the mass of B is set to 1 ($m_B = 1$). Three different reaction probabilities of 0.1, 0.2 and 0.5 are used. The same probability of reaction is used for the forward and backward reaction. This would correspond to a $k_{r,A \leftrightarrow 2B}$ of 0.0625, 0.125 and 0.3125, respectively. The same probability of adsorption ($P_{ads} = 0.05$) and desorption ($P_{des} = 0.0001$) were used as in the previous subsection for both species A and B. This corresponds to $k_{des,A} = 0.001$ and $\sqrt{2}k_{ads,A} = k_{ads,B} = 0.00125$. The rate of change of the catalyst occupation of A and B (denoted by θ_A and θ_A) are given by:
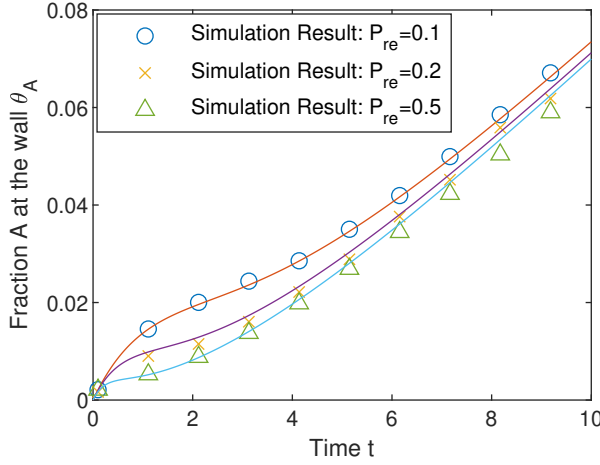
Figure 4.5: Simulation results (symbols) and numerical results (lines) for a mean-field reversible reaction $A + * \rightarrow 2B$ for different reaction probabilities (0.1, 0.2 and 0.5).

$$\frac{d\theta_A}{dt} = k_{ads,A}\theta_V\gamma(t)x_A(y=0,t) - k_{des,A}\theta_A \tag{4.24}$$
$$- \frac{k_{r,A\leftrightarrow B}N_{cat}}{A_{cat}}\theta_A\theta_V + \frac{k_{r,A\leftrightarrow B}N_{cat}}{A_{cat}}\theta_B^2$$

$$\frac{d\theta_B}{dt} = k_{ads,B}\theta_V\gamma(t)x_B(y=0,t) - k_{des,B}\theta_B \tag{4.25}$$
$$+ \frac{k_{r,A\leftrightarrow B}N_{cat}}{A_{cat}}\theta_A\theta_V - \frac{k_{r,A\leftrightarrow B}N_{cat}}{A_{cat}}\theta_B^2$$

The numerical and simulation results are shown in Fig. 4.5. The reaction shows an initial non-linearity which ceases at $t > 7$. The onset of this quasi-steady state originates from the reversibility of the reaction. As it proceeds, the production and consumption term of A and B equilibrate and mainly the linear growth due to adsorption is observed. This equilibration of the non-linear reactive terms happens more rapidly when $k_{r,A\leftrightarrow B}$ becomes large compared to the other process rates (desorption and adsorption). At later stages, it is expected that the fraction of A at the wall will equilibrate. This will occur when the vacant surface sites become more occupied thereby making the adsorption and desorption process reach the same rate. However, this is still not observed at the time scales considered ($0 < t < 10$). Based on Fig. 4.5, the simulation seems capable in representing both the non-linear change in the initial stage ($t < 5$) and the increase in the latter stage.

4.3.3   SURFACE INTERACTION

After having validated the bi-particle mean-field reactions, it is now possible to simulate more complex surface reactions in which the mean-field assumptions are no longer valid. This applies to reactions in which the unfavorable interactions between different adsorbed species leads to species separation and formation of 'islands'. Examples of such reactions include heterogeneously catalyzed nitrogen oxide reduction by ammonia [24] or hydrogen [25] and the CO oxidation reaction [26]. In this section, the influence of island formation on the reaction rate of a $A + B \rightarrow C$ reaction is evaluated by drawing comparisons with mean-field reactions that were discussed previously. The method of simulating the surface interactions of particles and the consequent separation of particles into islands is described in Section 4.2.

Fig. 4.6 shows that boundaries are less isotropic when only nearest neighboring interactions are considered than when second neighboring interactions are also included. This finding indicates that the second neighboring interactions should be considered at the very least for a realistic accounting of the surface interactions. Taking additional neighboring interactions into account can lead to more isotropic boundaries, but will increase the computational cost.

To demonstrate island-formation, only repulsive forces between two separate species are considered in this study. However, separation between the particles can also occur if the interactions of the species with themselves is more favorable than the inter-species interactions. The magnitude and sign of interactions will depend on the species that are simulated. The influence of having different magnitudes of interactions is considered here to demonstrate its consequence for the coupling between the SRD simulation and the mesoscopic Monte Carlo method.

To study the influence of island formation on bi-particle reaction rates, a $A + B \rightarrow C$ reaction is considered. This reaction was also studied in Section 4.3.2 under mean-field conditions at different reaction rates. A probability of reaction of 0.1 (corresponding to a mean field rate constant of 1 a_0^2/t_0) is studied. An E_0 of $2.00 k_B T$ is considered (second neighboring interactions are included as described Section 4.2), with 5 Monte-Carlo steps per adsorbed particle at each Δt_s. This corresponds to islands formed on the scale of around 5 a_0 (similar to the islands in Fig. 4.6 (b)).

Fig. 4.7 shows that surface interactions (i.e., the case of island formation) can have a considerable influence on the reaction rate. As species A and B have unfavorable interactions, the probability that they come into contact is lowered with respect to the mean-field assumption. This lowers the reaction rate. This effect is prominent especially in the initial stages when the reactants A and B can avoid being in contact (as most of the catalyst sites are vacant). From Fig. 4.7, adsorption is the dominating mechanism up until the time of $t = 30$, after which depletion of A occurs as the reaction rate becomes prominent. The
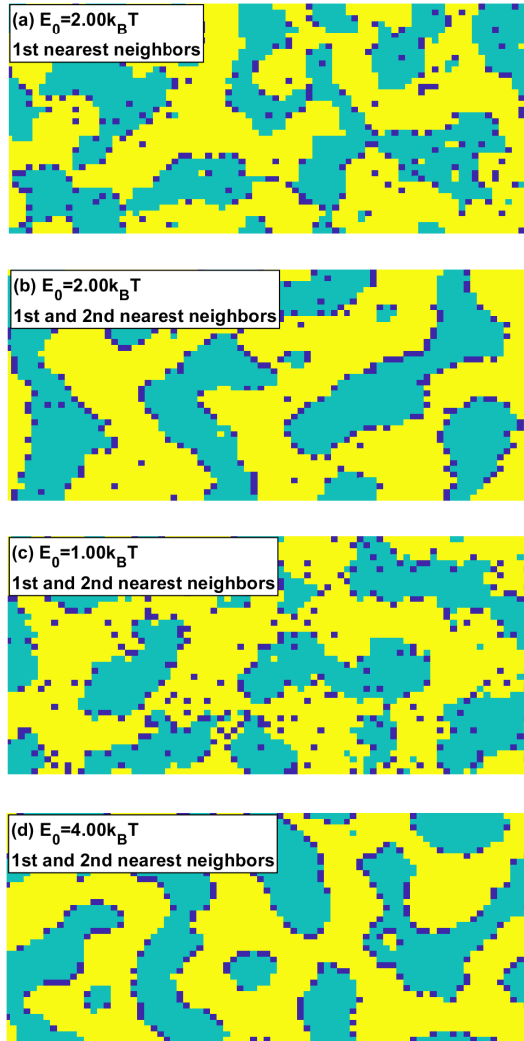
Figure 4.6: Island formation between two species A and B with different energetic interaction (E_0) between two adjacent inter-species and taking into account different neighbors. The yellow, green and blue color represent A, B and vacant sites, respectively.
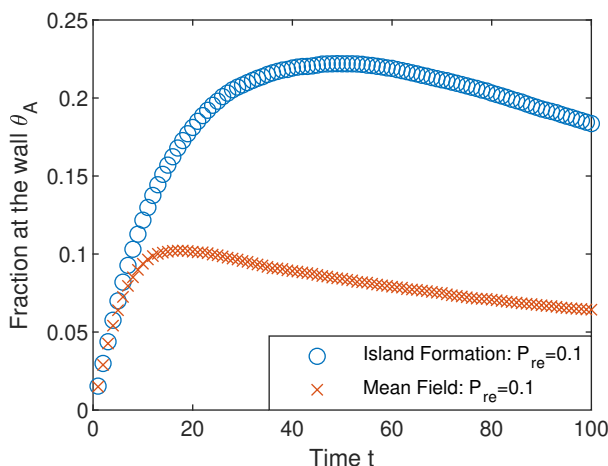
Figure 4.7: Influence of island formation on bi-molecular reactions. The same probability of re-action ($P_{re} = 0.1$) is used for both the mean-field and non-mean-field, island forming, model. The initial mixture consist of 50% (molar) of species A and 50% of species B.

same transition between dominant mechanisms occurs already at $t = 10$ for the mean-field case. Consequently, the maximum fraction of A on the surface is approximately twice as high when island formation is considered. This notable change signifies the importance that surface interactions can have in reaction mechanisms.

4.3.4   ELEMENTARY REACTION

The methods developed so far are applied to simulate a gas-phase reaction involving three different elementary steps to show the potential usage of SRD in heterogeneously cat-alyzed reaction. An example of a typical industrially relevant reaction explained in terms of this mechanism is CO oxidation. Since this reaction involves a mixture of components, a multi-component diffusion model is needed to accurately predict the concentration pro-files that form in the catalytic channel. For such surface reactions, catalysts are inherently dynamic in nature. Dynamic surface behavior such as surface reconstruction has been investigated in various experimental works and molecular simulations[27–31]. The ob-jective of the current work is to mimic the mechanism, not to incorporate full atomistic details of the surface kinetics for a certain reaction. Effects of surface reconstruction and specific crystal structures are not considered in this work. There is a clear distinction be-tween our test case and a real CO oxidation reaction in the sense that the surface ordering of the species and locations of O(ads) and CO(ads) on the surface would need a more thorough consideration (e.g. to consider short length O(ads)-O(ads) repulsion and sur-face restructuring that can occur at higher O(ads) fractions). The simulation considered

in this section involves 3 species in the SRD domain, namely species A, B_2 (the notation B_2 is picked because this species will dissociate into $2B_{ads}$ on the surface) and the product C. Species A has a unit mass m_0, species B_2 is given a mass of 1.17 m_0 and species C is given a mass of 1.57 m_0 to mimic the mass ratio of CO, O_2 and CO_2, respectively. Due to the differences in mass, it can be seen that the species considered have different self-diffusion coefficients (see Table 2.2). Specifically, the self-diffusion coefficient of species A is around 15% higher than that of B_2 and around 36% higher than that of species C. This difference warrants the need for a multi-component diffusion model. Based on the mechanism of CO oxidation, the change of these three species through the surface catalyzed reaction is shown below.

$$A + * \quad \leftrightarrow \quad A_{ads} \tag{4.26}$$

$$B_2 + 2* \quad \rightarrow \quad 2B_{ads} \tag{4.27}$$

$$A_{ads} + B_{ads} \quad \rightarrow \quad C + 2* \tag{4.28}$$

In this reaction mechanism, species A and B_2 adsorb on the catalyst surface with an adsorption probability of 0.05, while C does not undergo adsorption. To simulate catalyst poisoning, species A_{ads} is given a low desorption probability of 0.0001, while B_{ads} does not undergo desorption. A_{ads} and B_{ads} have unfavorable repulsive interactions ($E_0 = 2k_b T$) and can react together with a probability of 0.1 to form the product C. Upon formation, C desorbs off the wall instantaneously. To test the mechanism and probe the influence of the initial composition on the reaction rate and the fraction induced on the wall, three different compositions are tested. These compositions consist initially only of reactants at A to B_2 molar ratios of 1:1, 2:1 and 1:2, respectively. In Fig. 4.8a, the fraction of A_{ads} and B_{ads} on the wall is shown over time for an equimolar initial mixture of A and B_2. This composition is more optimal compared to the other two compositions as none of the species is fully poisoning the catalyst by excessively occupying the catalytic sites. Furthermore, as the fractions of A_{ads} and B_{ads} are both high (at least until time $t = 100t_0$), the largest production rate is expected. The large fractions of A_{ads} and B_{ads} are especially important in this reaction mechanism as island formation of A and B is considered (as the species will tend to avoid each other when the occupied fractions are smaller).

The product concentration profile at time $t = 100t_0$ for different initial compositions is compared in Fig. 4.8b. This figure shows that at time $t = 100t_0$ there are significant spatial variations in the bulk fluid (especially in the equimolar reactant mixture test case). The total production of C is obtained from the area under these curves. Comparing these areas shows that a 1:1 initial ratio of A to B_2 is preferred as it yields approximately 25% more production of C than the least optimal composition, being the 2:1 ratio.

Notably, the profiles obtained in Fig. 4.8b are not easily obtainable numerically without making simplifications since multi-component diffusion models would need to be
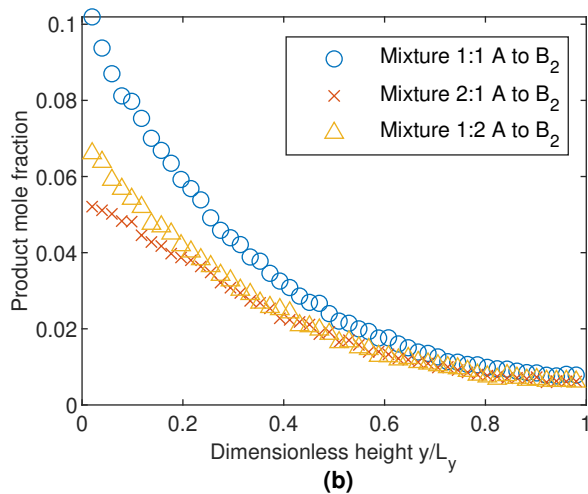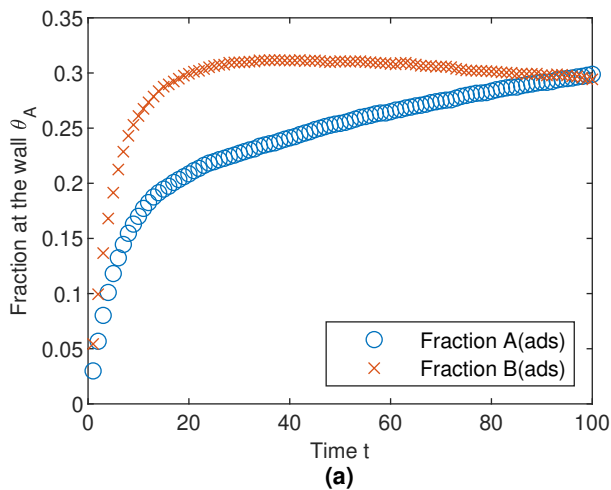
Figure 4.8: Non-mean-field elementary reaction mechanism involving a three-step reaction mechanism with reactant dissociation (Eqs. 5.7-5.9). (a) Evolution of the A_{ads} and B_{ads} fraction at the wall for an initial 1:1 A to B_2 molar ratio. (b) Product concentration profile at time $t = 100t_0$ for initial A to B_2 molar ratios of 1:1, 2:1 and 1:2, with no product initially.

applied with composition dependent Maxwell-Stefan diffusion coefficients. These then need to be further coupled to the non-linear surface reaction kinetics. This simulation therefore demonstrates the convenience and capability of SRD simulations when having multi-component reactive mixtures with complex reactive boundary conditions.

4.4 CONCLUSION

We developed a mesoscopic framework to study heterogeneously catalyzed multi-particle reactions both in the mean-field and non mean-field regime, connecting mass transport in the fluid to elementary reaction steps on the catalytic surface. Multiple test cases were carried out to demonstrate that the developed method produces the correct reaction behavior. Mean-field elemental reactions can be simulated by neglecting particle-particle interactions on the surface, ensuring that the adsorbed particles can react at any location on the surface. Non-mean-field reactions can be simulated by applying a mesoscopic Monte Carlo simulation on the surface, with the bulk fluid simulated by SRD.

Comparing an $A + B \rightarrow C$ reaction in the mean-field and non mean-field regime demonstrated that the formation of islands for different species can lead to significant coverage differences due to inhibition of reaction rates. These differences demonstrate the importance that surface interactions may have on the total reactivity of a system. Surface mechanisms, such as island formation, are intricately linked to spatial variations in composition, which are in turn related to imposed external forces and flow profiles. Although convective effects were not studied in this work, they can easily be considered.

The method was applied to a heterogeneously catalyzed reaction mechanism in a multi-component gas phase system with a three-step mechanism involving the initial adsorption of a reactant, its dissociation on the catalyst surface, and a surface reaction. A catalyst poisoning process was simulated by imposing a low desorption rate. This simulation allowed for coupling between detailed surface information (such as surface interaction and coverage results) to spatial concentration variations in the bulk of a multi-component gas mixture. Allowing for such intricate combinations illustrates the strength of the method developed.

CHAPTER 4

REFERENCES

[1]   Kay Tucci and Raymond Kapral. "Mesoscopic Multiparticle Collision Dynamics of Reaction- Diffusion Fronts." In: *The Journal of Physical Chemistry B* 109.45 (2005), pp. 21300–21304.

[2]   Katrin Rohlf, Simon Fraser, and Raymond Kapral. "Reactive multiparticle collision dynamics." In: *Computer Physics Communications* 179.1-3 (2008), pp. 132–139.

[3]   Alireza Sayyidmousavi and Katrin Rohlf. "Reactive multi-particle collision dynamics with reactive boundary conditions." In: *Physical biology* 15.4 (2018), p. 046007.

[4]   Jiang-Xing Chen, Yu-Guo Chen, and Raymond Kapral. "Chemically propelled motors navigate chemical patterns." In: *Advanced Science* 5.9 (2018), p. 1800028.

[5]   Pierre de Buyl and Raymond Kapral. "Phoretic self-propulsion: a mesoscopic description of reaction dynamics that powers motion." In: *Nanoscale* 5.4 (2013), pp. 1337–1344.

[6]   Jiang-Xing Chen and Raymond Kapral. "Mesoscopic dynamics of diffusion-influenced enzyme kinetics." In: *The Journal of chemical physics* 134.4 (2011), 01B624.

[7]   Gunnar Rückner and Raymond Kapral. "Chemically powered nanodimers." In: *Physical review letters* 98.15 (2007), p. 150603.

[8]   Pierre de Buyl. "Mesoscopic simulations of anisotropic chemically powered nanomotors." In: *Physical Review E* 100.2 (2019), p. 022603.

[9]   Shang Yik Reigh, Mu-Jie Huang, Hartmut Löwen, Eric Lauga, and Raymond Kapral. "Active rotational dynamics of a self-diffusiophoretic colloidal motor." In: *Soft matter* 16.5 (2020), pp. 1236–1245.

[10]   Andreas Zöttl. "Simulation of microswimmer hydrodynamics with multiparticle collision dynamics." In: *Chinese Physics B* 29.7 (2020), p. 074701.

[11]   A Sengar, JAM Kuipers, Rutger A Van Santen, and JT Padding. "Particle-based modeling of heterogeneous chemical kinetics including mass transfer." In: *Physical Review E* 96.2 (2017), p. 022115.

[12]   A Sengar, JAM Kuipers, RA van Santen, and JT Padding. "Towards a particle based approach for multiscale modeling of heterogeneous catalytic reactors." In: *Chemical Engineering Science* 198 (2019), pp. 184–197.

[13]   Sebastian Muehlbauer, Severin Strobl, Matthew Coleman, and Thorsten Poeschel. "Simulation of catalytic reactions in open-cell foam structures." In: *arXiv preprint arXiv:2010.03904* (2020).

[14]   Wen Lai Huang and Jinghai Li. "Mesoscale model for heterogeneous catalysis based on the principle of compromise in competition." In: *Chemical Engineering Science* 147 (2016), pp. 83–90.

[15]   Joaquın Cortés, Heinrich Puschmann, and Eliana Valencia. "Mean-field hierarchical equations for some A+ BC catalytic reaction models." In: *The Journal of chemical physics* 109.14 (1998), pp. 6086–6091.

[16]   Dan S Bolintineanu, Jeremy B Lechman, Steven J Plimpton, and Gary S Grest. "No-slip boundary conditions and forced flow in multiparticle collision dynamics." In: *Physical Review E* 86.6 (2012), p. 066703.

[17]   Rong Fan, Githin T Zachariah, Johan T Padding, and Remco Hartkamp. "Real-time temperature measurement in stochastic rotation dynamics." In: *Physical Review E* 104.3 (2021), p. 034124.

[18]   Mie Andersen, Chiara Panosetti, and Karsten Reuter. "A practical guide to surface kinetic Monte Carlo simulations." In: *Frontiers in chemistry* 7 (2019), p. 202.

[19]   Richard LeSar. *Introduction to computational materials science: fundamentals to applications*. Cambridge University Press, 2013.

[20]   H Steininger, S Lehwald, and H Ibach. "Adsorption of oxygen on Pt (111)." In: *Surface Science* 123.1 (1982), pp. 1–17.

[21]   Tomaso Zambelli, Johannes V Barth, Joost Wintterlin, and Gerhard Ertl. "Complex pathways in dissociative adsorption of oxygen on platinum." In: *Nature* 390.6659 (1997), pp. 495–497.

[22]   BK Min, AR Alemozafar, MM Biener, J Biener, and CM Friend. "Reaction of Au (111) with sulfur and oxygen: Scanning tunneling microscopic study." In: *Topics in Catalysis* 36.1 (2005), pp. 77–90.

[23]   Xingyi Deng, Byoung Koun Min, Amado Guloy, and Cynthia M Friend. "Enhancement of O2 dissociation on Au (111) by adsorbed oxygen: implications for oxidation catalysis." In: *Journal of the American Chemical Society* 127.25 (2005), pp. 9267–9270.

[24]   G Veser, F Esch, and R Imbihl. "Regular and irregular spatial patterns in the catalytic reduction of NO with NH 3 on Pt (100)." In: *Catalysis letters* 13.4 (1992), pp. 371–382.

[25]   VP Zhdanov and B Kasemo. "Monte Carlo simulation of oscillations in the NO–H2 reaction on Pt (1 0 0)." In: *Applied Catalysis A: General* 187.1 (1999), pp. 61–71.

[26] Paul T Fanson, W Nicholas Delgass, and Jochen Lauterbach. "Island formation during kinetic rate oscillations in the oxidation of CO over Pt/SiO2: A transient Fourier transform infrared spectrometry study." In: *Journal of Catalysis* 204.1 (2001), pp. 35–52.

[27] Ronald Imbihl and Gerhard Ertl. "Oscillatory kinetics in heterogeneous catalysis." In: *Chemical Reviews* 95.3 (1995), pp. 697–733.

[28] AL Vishnevskii and VI Savchenko. "Self-oscillations in the rate of CO oxidation on Pt (110)." In: *Reaction Kinetics and Catalysis Letters* 38.1 (1989), pp. 167–173.

[29] Vladimir I Elokhin, Andrei V Matveev, Evgenii V Kovalyov, and Vladimir V Gorodetskii. "From single crystals to supported nanoparticles in oscillatory behavior of CO+ O2 reaction on platinum and palladium surfaces: Experiment and stochastic models." In: *Chemical Engineering Journal* 154.1-3 (2009), pp. 94–106.

[30] NV Petrova and IN Yakovkin. "Monte Carlo simulation of CO and O coadsorption and reaction on Pt (1 1 1)." In: *Surface science* 578.1-3 (2005), pp. 162–173.

[31] Da-Jiang Liu and JW Evans. "Atomistic and multiscale modeling of CO-oxidation on Pd (1 0 0) and Rh (1 0 0): From nanoscale fluctuations to mesoscale reaction fronts." In: *Surface science* 603.10-12 (2009), pp. 1706–1716.

<div style="text-align: right; font-size: 3em;">5</div>

SIMULATING REACTIONS IN COMPLEX GEOMETRIES

5.1 INTRODUCTION

For heterogeneous catalysis, reactions happen on the catalyst surface. Therefore, maximising the contact surface area between the catalyst and the fluid phase is a key factor in enhancing the reaction process. Zeolites or other porous media such as metal-organic frameworks (MOFs) become the material of choice to support the catalytic active sites. The structure of zeolites and MOFs can be found in databases [1] or obtained from crystallographic data [2]. For amorphous catalyst supports, catalyst pellets have internal macropores and micropores, with a distribution that is typically highly irregular. The stochastic nature of the pore space distribution is complicating analytical prediction of the interplay between reaction kinetics and mass transfer [3]. This is where simulations can help.

Various methods have been developed to simulate the irregular porous structures of heterogeneous catalysts. Random pores [4] and Bethe lattices[5, 6] have been introduced to simulate a catalyst network in two dimensions. The employment of Voronoi polyhedra includes the connectivity and cycle loops of pores [7]. These ideas can be expanded to 3-D pore networks.

For mesoscale simulations, most works that involve complex geometries focus on the influence of pore structure on material properties, such as those of concrete, sandstone and membranes [8–10]. Reactions are studied in some coarse grained works, in particular when they cause a geometry change. For instance, Tarabkhah et al. simulated fluid flow and chemical reactions in different porous media for cases where the porous media volume and structure changed during reaction [11].

In contrast to LBM or lattice gas cellular automata (LGCA), complex geometry generation in SRD is relatively easy because, as far as boundaries are concerned, SRD is a lattice-free method; the only important thing is to have a mathematically convenient way to detect the collision of an SRD particle with a solid boundary. It is possible to define the geometry in multiple ways. For example, spheres with mathematically defined boundaries can be implemented in SRD, as shown in Chapter 3. Though it is possible to fully define complex geometries using mathematical equations, the computing cost to resolve the geometry could become prohibitively expensive. On the other hand, the pore structure
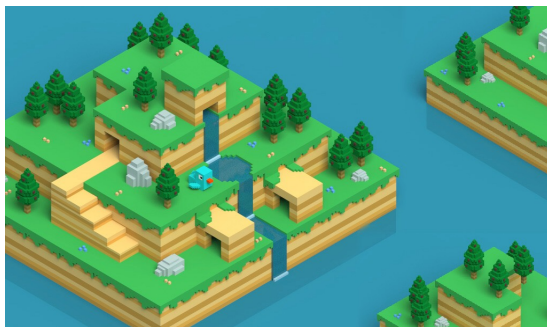
Figure 5.1: Video game made with voxels [12].

of real catalyst materials could be obtained from multiple experimental measurements such as microcomputed tomography (microCT), atomic force microscopy (AFM), transmission electron microscope (TEM), and optical profilometers. It is convenient to build the three-dimensional model based on volume elements with a certain shape. Voxels, as popularly applied in video games as shown in Figure 5.1, can be an option for building a complex geometry. This is the approach we will take in this chapter.

5.2   METHOD

5.2.1   GEOMETRY GENERATION

There are many methods to generate random porous media structures, for example through a reconstruction process using deep learning of images, through a simulated annealing method, or using multiple-point statistics [13–15]. The correct inclusion of spatial correlations in the pore space distribution in the reconstruction method is crucial and complicated. The simplest method is to randomly distribute obstacles or pores, ignoring any other details of microstructure. Wang et al. [16] proposed the quartet structure generation set (QSGS) approach, based on the idea of Coveney et al. [17] and cluster growth theories [18], growing the pores with time and controlling the structure by a set of parameters such as initial probability of pore core distribution, neighboring growing probability and volume fraction.

A similar approach could be used to generate a voxel-based catalyst porous structure for SRD simulations. A flowchart containing the steps of the approach used in this research is shown in 5.2. Four main steps are used. First, n voxels are randomly picked from a solid block of voxels and converted to pore (fluid) voxels. These selected voxels will serve as the starting point for creating pores. Then, a probability test is performed (meaning that a uniform number between 0 and 1 is drawn) for all of the neighbors of the selected starting
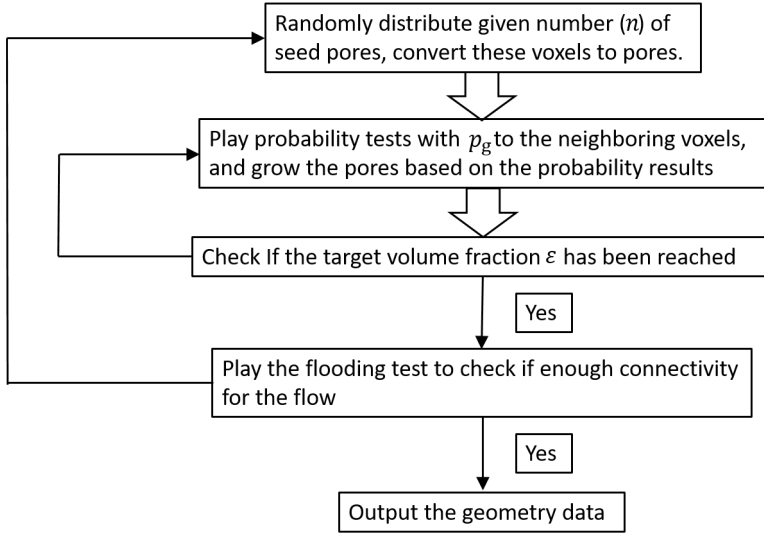
Figure 5.2: Flowchart of the pore geometry generation algorithm.

voxels. If the test is satisfied (meaning that the random number is smaller than the specified probability), the neighboring voxel is converted to a pore voxel.

A pseudo-code of the probability test is as follows:

```
p=0.5;  % probability of generating a fluid neighbouring voxel
void = C; %voidage of pre-existing pores
count=0;
loop=1;
while (void < desiredvoidage)
   i = randi[1,Lx] %pick a random voxel within the domain of [Lx,Ly,Lz]
   j = randi[1,Ly]
   k = randi[1,Lz]
   if Voxel(i,j,k)==0 && rand()<p %add neighbouring fluid voxel
      x=randi[-1,1]; %decide to add voxel in the x-, y-, or z-direction
      delta = 2*randi[0,1]-1; %negative or positive direction
      if x==-1 && i+delta>0 && i+delta<Lx+1 && Voxel(i+delta,j,k)==1
         Voxel(i+delta,j,k)=0;
         count =count+1;
      endif
      if x==0 && j+delta>0 && j+delta<Ly+1 && Voxel(i,j+delta,k)==1
         Voxel(i,j+delta,k)=0;
         count =count+1;
      endif
      if x==1 && k+delta>0 && k+delta<Lz+1 && Voxel(i,j,k+delta)==1
```

CHAPTER 5

```
        Voxel(i,j,k+delta)=0;
        count =count+1;
      endif
    endif
   void = void + count/(Lx*Ly*Lz); %update the total voidage
endwhile
```

At the end step of the geometry generation loop, a flooding test is done to ensure the connectivity of the porous media catalyst region allowing the fluid to go through the region from one side to the other. The flooding test is conducted by starting from one side of the catalyst region, assuming the fluid comes from this side. In the test, the check will go along with the fluid direction and check for each position whether the fluid can reach another voxel. Each voxel that the fluid can reach will be remembered in a given condition index, like being "colored".

A two-dimensional example of the method is shown in Figure 5.3. In this example, the bulk of the catalyst region is located between $x = 0$ and $x = 8$. Some voxels are solid and some are hollow. If the flow starts at $x = 0$, there are two hollow voxels in the first layer (lowest x coordinate). When the two hollow voxels are detected, they will be "colored" (given a special index in the program), as shown in red in the figure. Then, a check of their neighbors will be done and the connected voxels will also be colored. At this moment, one voxel in the second layer of x coordinates is colored. Then the loop goes to the second layer of x coordinates, checking any colored voxels' neighbors and coloring them. This process repeats until the last layer in the x-direction. Then for a 2-D scenario, the same coloring process needs to be done in the y-direction, which will allow for connectivity with backflow, as shown in Figure 5.3. When all connected hollow voxels are colored, the existence of at least one colored voxel in the last layer of the catalyst along the flow direction shows the connectivity (i.e. the existence of a percolation path) throughout the whole region. Unconnected pores, like shown in grey in the Figure, are not colored in the flooding test and are not reachable by the fluid.

An example of a 3D pore geometry generated through the above methodology is shown in Figure 5.4. Alternatively, a catalyst geometry could be generated starting with seeds of channels instead of pores. This method uses a similar strategy as the previous one, however, it gives very different results. Instead of generating random void seeds inside the solid part, random void seeds are located on the surface. For each seed, there are 6 directions for the pore to grow: one forward and five other directions to a neighboring cell. The probability of growing forward is set to be larger than the probability of growing around, therefore the channel will ultimately grow to the other side of the solid part. An example of this generating method result is shown in Figure 5.5. The advantage of this method is that the channels will naturally pass the flooding test.
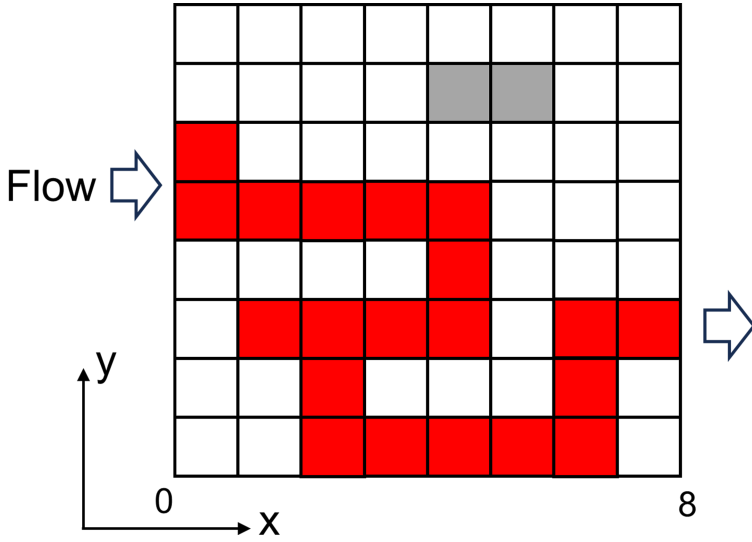
Figure 5.3: Illustration of the flooding test: Solid voxels are colored white, flow connected voxels red, and unconnected voxels grey. See the main text for details.
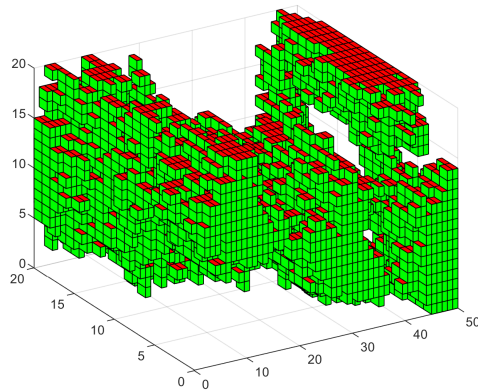

Figure 5.4: Example of a pore space generated through $n = 15$ seeds and probability $p = 0.5$ for a porosity of $\epsilon = 0.3$.
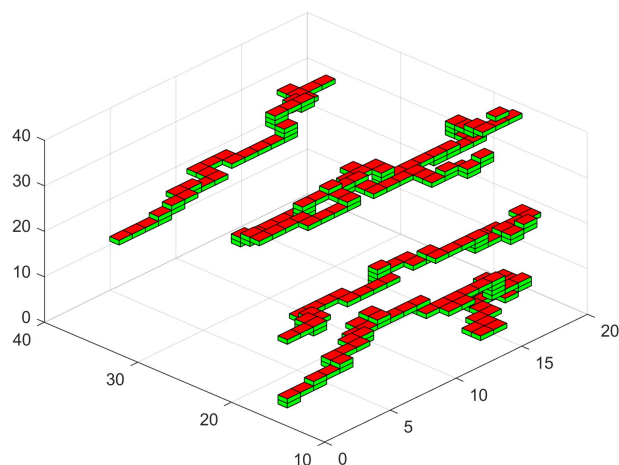
Figure 5.5: Example of channels generated with 4 surface seeds, with a forward probability of 0.4 and probabilities for the other directions (including backward) equal to 0.12.

5.2.2 COMPLEX GEOMETRY BOUNCE-BACK IMPLEMENTATION FOR SRD

After having generated a complex voxel geometry, another problem must be solved: how to bounce back SRD particles from the solid voxel walls efficiently. To solve this problem, a proper solid mapping and bounce-back method is needed. The mapping algorithm used in this research is described below.

After updating the position of a particle, the integer values of the old and new positions are taken and compared (where the voxel size is conveniently taken to be unity) in each coordinate direction. The differences of these values in each direction are saved as dix, diy, diz. These values could be negative, positive or zero, and contain information about the possible intersection of the particle path with one of the solid voxel faces. In consideration of the small mean-free-path chosen in our work, in general, the travelling distance would not be more than one grid, so we can assume that the absolute value of the difference integer would not be larger than 1. If the value equals 0, this means that the particle has travelled within the same grid in this coordinate direction, which implies there is no possibility of collision with a solid voxel in this direction. A value not equal to zero means that the particle moved across a grid boundary in that coordinate direction, and a collision could have happened depending on whether or not there is a solid surface present in between. Therefore, it is necessary to check the precise collision situation.

Let us first determine the solid boundary that the particle hits first (if any) within the last time step Δt_s. Since we have already taken the values of new and old positions, we can easily calculate the coordinate of the (possible) crossing point in each direction: it is

either on the left- or righthand side boundary of the cell of the old particle position, and this information is already contained within the value of the integer difference value in that direction. For example for a possible intersection in the x-direction, the intersection x-coordinate x1 can be calculated by $x1 = ixo + (dix + 1)/2$, where ixo is the integer of the particle's old x-position. Based on this value, the value of the travelling time that the particle needed to move to this boundary can be calculated through $t1 = (x1 - xold)/Vx$, where Vx is the particle's x-velocity component. This time is then used to calculate the on-surface impact coordinates $(y1, z1)$. Similarly the (possible) collisions in the y and z directions lead to surface crossing coordinates $y2$ and $z3$, travelling times $t2$ and $t3$, and on-surface impact coordinates $(x2, z2)$ and $(x3, y3)$, respectively. By finding the order of traveling times in the three different directions, we can calculate the order of the boundaries that the particle (potentially) hits.

Once we have the grid surface impact positions, we can find out if we are dealing with a solid surface, in the order of the traveling times (as long as they are shorter than the time step Δt_s). If a solid surface is hit, adsorption of the particle is attempted with a probability test. If the particle is not adsorbed, it is bounced back into the fluid domain. In principle the particle could hit another surface within the same time step, and should therefore be adsorbed or bounced back at the next surface. However, in this work we assume that the typical displacement of a particle within a time step Δt_s is small relative to the voxel size. Therefore we can limit ourselves to an accurate adsorption/bounceback treatment for the first surface that is hit, and a much simpler scheme that folds the particle position back into the fluid (effectively bounce-forward) for any subsequent surface collisions within the same time step. This simplification will only affect particles very close to the corners of the voxelated geometry. To better explain this process, Figure 5.6 schematically shows the calculation and changes of variables.

5.2.3   REACTION SCHEME

Similar to our previous work in Chapter 4, each elementary step (adsorption, reaction and desorption) of the whole reaction with Langmuir-Hinshelwood kinetics is updated by the streaming time-step (Δt_s), as discussed in detailed in previous work [19]. However, the setting of catalyst site distribution and local vacancy is different with previous works. In this work, the catalyst surface is divided into unit surface areas (the voxel implementation of the catalyst geometry makes it easy to define the unit surface as a voxel surface). The number of catalyst sites can be set on each unit surface, allowing for a locally varying occupancy of catalyst sites. When a particle collides with a catalyst surface, the location of the particle is checked and a further probability test is applied to determine the next status of the particle. The probability test is performed in the same manner as in our previous work, as well as the reaction and desorption steps. For multi-particle reactions where the
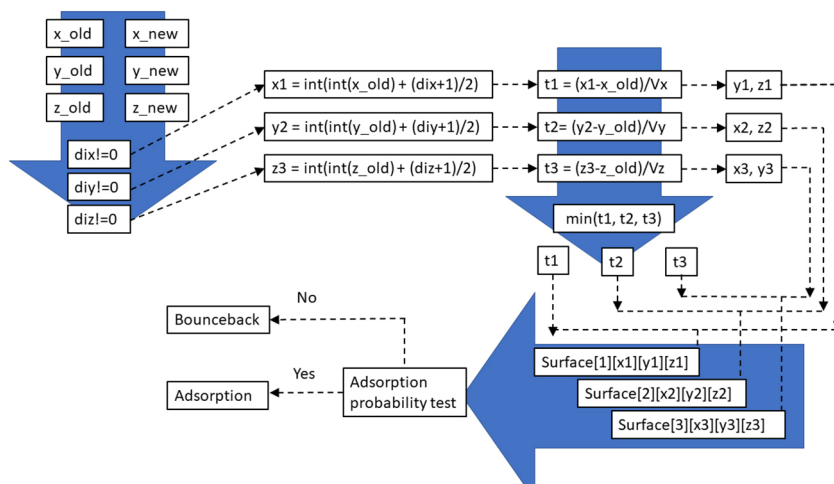
Figure 5.6: Flowchart of particle position mapping and collision detection with surfaces of a voxelated geometry. See main text for details.

particle number changes, the update is more complex and described in detail in 5.4.2. The conversion of simulation parameters and probabilities for the elementary steps to adsorption, reaction and desorption rates are shown in Table 5.1, in which the probability of adsorption, reaction and desorption are P_{ads}, P_{re}, and P_{des} correspondingly.

5.3   VALIDATION

In this section, the adsorption, reaction and desorption processes are tested separately to validate the algorithm. The tests are done with a planar surface, but using the voxelated geometry algorithm.

5.3.1   SIMULATION DOMAIN

The simulation domain for validation is a cuboid space with the dimension of 80, 20 and 20 units in the x, y and z directions, respectively, as shown in Figure 5.7. There are two solid plates with a thickness of 1 unit length on both sides of the domain confining the fluid in the z direction. A part of the solid-fluid interface is made catalytically active. This active area is chosen by randomly distributing the effective unit surface among the total surface area.

Table 5.1: Adsorption, reaction and desorption rates as a function of simulation parameters.

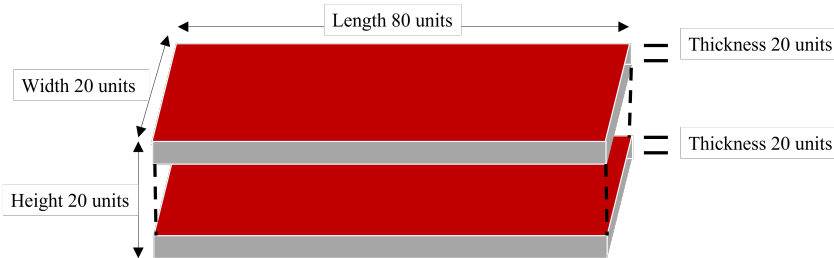|	
Particle concentration	$C_s = N/V$
Particle collision frequency	$Z = \frac{1}{2}\frac{N}{V}\langle|v_y|\rangle$
Average velocity in i-direction	$\langle|v_i|\rangle = \sqrt{2k_bT/(\pi m)}$
Rate constant of particle adsorption	$k_{ads} = \sqrt{\frac{k_bT}{2\pi m}}\frac{P_{ads}A_{cat}}{N_{cat}}$
Rate constant of reaction	$k_{re} = \frac{\ln(1-P_{re})}{\Delta t_s}$
Rate constant of particle desorption	$k_{des} = \frac{\ln(1-P_{des})}{\Delta t_s}$

Figure 5.7: Simulation domain.

5.3.2   ADSORPTION

For adsorption, the change in the number of absorbed particles, N_A, available catalyst sites, N_{cat}, and occupancy of particle A, θ_A, can be expressed as:

$$\frac{dN_A}{dt} = Zp_{ads,A}\frac{N_{cat} - N_A}{N_{cat}}A_{cat} \tag{5.1}$$

$$\theta_A = \frac{N_A}{N_{cat}} = 1 - e^{-Zp_{ads,A}\frac{A_{cat}}{N_{cat}}t} \tag{5.2}$$

where we assume that we start without any particles adsorbed and that only adsorption (no reaction, no desorption) is taking place.

Fig. 5.8 shows a verification of the adsorption function. In this test, the probability of adsorption is set to 0.1, and the effective surface area is set to 1200 unit cells. On average, each unit surface has 1 available catalyst site and in total 1200 catalytic sites are randomly distributed over the surface. A comparison of the analytical solution and simulation result in Figure 5.8 shows good agreement.
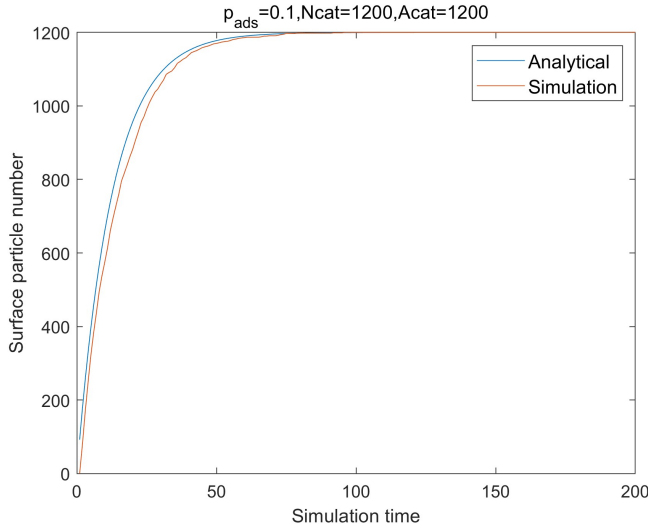

Figure 5.8: Comparison of the simulation result for the adsorption test against analytical solution.

5.3.3 REACTION

Next we turn to heterogeneously catalyzed reactions. Suppose the reactive surface is saturated with reactant particles A, undergoing a second-order reaction. Without simultaneous adsorption and desorption the occupancy of particle A should evolve as follows:

$$\frac{d\theta_A}{dt} = -k_{re}\theta_A{}^2 \tag{5.3}$$

$$\theta_A = \frac{1}{k_{re}t + C_0} \tag{5.4}$$

The value of C_0 can be calculated from initial conditions. In the validation of this section, the initial condition is $\theta_A(t=0) = 0.5$, i.e. $C_0 = 2$.

Figure 5.8 shows a verification of the reaction function. In this test, the reaction probability is set to $p_{re} = 0.05$, and the effective surface area is 100 unit cells. On average, each unit surface has 1 available catalyst site and 4000 catalytic sites are randomly distributed over the surface. A comparison of the analytical solution and simulation result in Figure 5.8 shows good agreement.
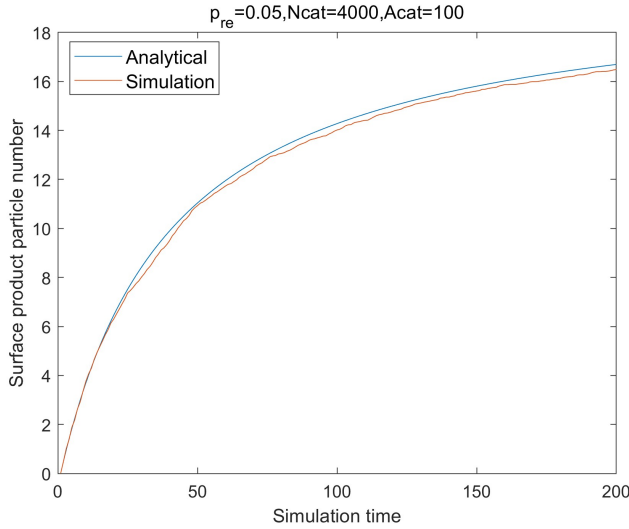

Figure 5.9: Comparison of the simulation result for the reaction test against analytical solution.

5.3.4   DESORPTION

Finally, we test the desorption function. For this, the only process that is allowed to happen is desorption itself. The initial condition is set to a surface saturated with a single species particle A. The occupancy of particle A can then be expressed as:

$$\frac{d\theta_A}{dt} = -k_{des}\theta_A \qquad (5.5)$$

$$\theta_A = e^{-k_{des}t} \qquad (5.6)$$

where we used that $\theta_A(t=0) = 1$.

Figure 5.10 shows a verification of the desorption function. In this test, the probability of desorption is set to 0.1, and the effective surface area is set to 1200 unit cells. On average, each unit surface has 4 available catalyst sites, so that 4800 catalytic sites are distributed over the solid surface. A comparison of the analytical solution and simulation result in Figure 5.10 again shows good agreement.
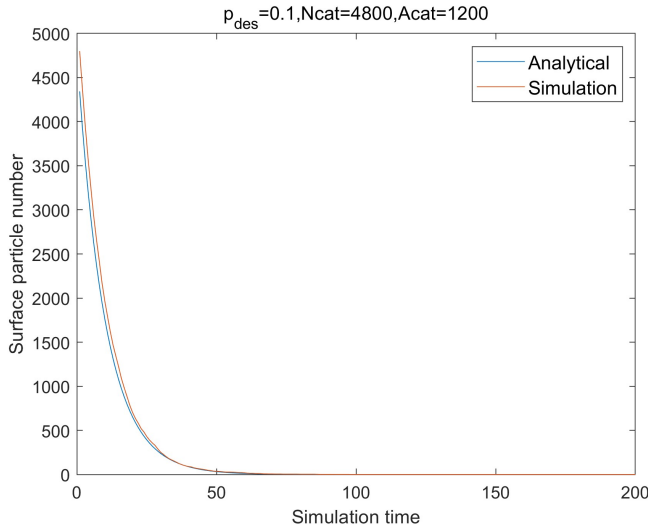

Figure 5.10: Comparison of the simulation result for the desoprtion test against analytical solution.

5.4   RESULTS

5.4.1   GEOMETRY GENERATION

Applying the random geometry generation method, a catalytic porous medium is generated and loaded in the simulation domain. The geometry has a void fraction of $\epsilon = 0.3$,

using $n = 15$ initial seeds, and a probability of generating voids in neighboring cell equal to $p = 0.5$. Slices of the catalyst at different y locations are shown in Figure 5.11. The total volume of the catalyst geometry is 13416 unit volume and the total surface area is 8505 unit area. For better observation of random effect and further contrast with another geometry, the effective catalyst sites are defined on the whole surface area. In this simulation, an area of 120 unit cells among the total of 8505 are randomly picked to be catalytically active. In each effective catalyst unit surface, 4 available catalyst sites are defined.
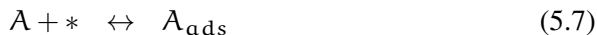
5.4.2 COMPLICATED REACTIONS IN A COMPLEX GEOMETRY

We will now show that the algorithm can also simulate more complicated heterogeneous surface reactions, in this case based on the Langmuir-Hinshelwood mechanism. Real reactions can also be complicated by the fact that the number of molecules can change with the reaction. The mass transfer and catalyst deactivation could be significantly influenced by the complexity of the pores' geometry. Therefore, it is particularly important to simulate the reaction environment close to a real heterogeneous catalytic reactor.

In this section, we will demonstrate that the hybrid method developed in this chapter can simulate a heterogeneous catalytic reaction in which the number of molecules changes in a complex porous geometry. This gas-phase reaction contains 3 elementary steps:

1 Adsorption of particle A or B on the catalytic surface, each on one catalytic site.

2 Combination of particles A and B on the same surface cell to product particle C.

3 Desorption of the product particle C.

Similar to the study in Chapter 4, the process can be described as:

$$A + * \quad \leftrightarrow \quad A_{ads} \tag{5.7}$$
$$B_2 + 2* \quad \rightarrow \quad 2B_{ads} \tag{5.8}$$
$$A_{ads} + B_{ads} \quad \rightarrow \quad C + 2* \tag{5.9}$$

In contrast with Chapter 4, in this simulation, the interactions between species are ignored since it is not under the same conditions and with the same method. The method developed in this chapter allows particles to be adsorbed locally and react with particles adsorbed on the same grid, therefore the influence of geometry could be highlighted and shown in the results.

In this simulation, the collision interval value is taken as 0.1 unit simulation time. The average particle density in each SRD grid is set as 5, to ensure a balance between enough particles in the system to sustain the fluid phenomena and efficiency of the simulations. For real molecules in a reactive gas, the molecular mass of different species is different,
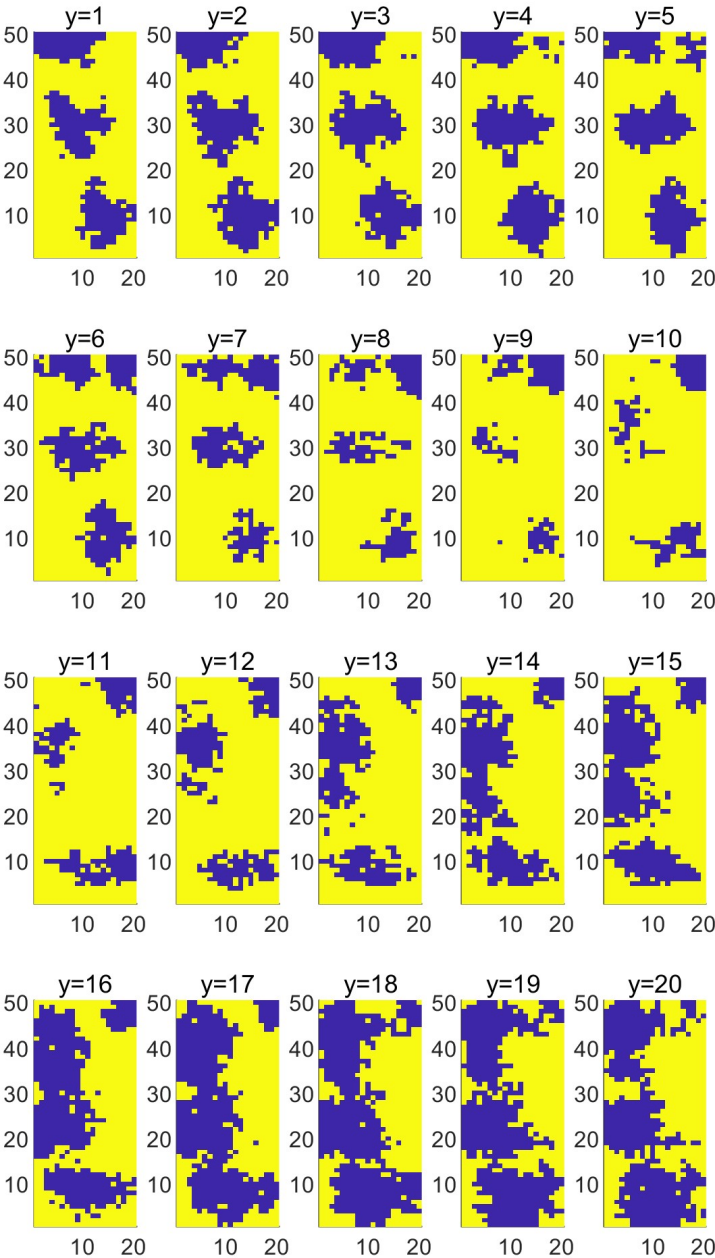
Figure 5.11: Slices of the random catalyst geometry in the the xz-plane for different y values. Solid is yellow. Pore space is blue.

resulting in different diffusivities. Therefore, the species A, B, C and inert (solvent) particles are given the particle mass 28, 32, 44 and 30, respectively. In this simulation, the adsorption probability of both particles A and B is 0.1. The probability of product particle desorption is set to 0.01. For more significant reaction changes, the desorption probability of particles A and B, and the adsorption probability of the product particle C are set to 0 to force the reactant conversion to the product.

A fluid flow is generated by exerting an external force on the particles, mimicking the effect of a pressure gradient across the porous medium. At the start of the simulation, surface reactions, absorption and desorption of particles are all deactivated (by setting all probabilities to zero) to allow for a steady flow to develop. After this, the surface reactions are activated by setting the probabilities for adsorption, reaction and desorption to their respective values.

A technical difficulty of updating reactions for such a multi-particle reaction mechanism is updating the fraction of every species in real time during one time step, especially when the changes in a single time step can be relatively large. When dealing with a certain particle, it is necessary to let that particle know the change of the fractional occupancy caused by other particles. This is not possible in principle when treating each particle sequentially, although the approach will be slightly better when updating the particles in a random order. The most realistic operation is to update all particles based on the condition of the previous time step. However, this may lead to a situation in which the reaction consumes more particles than is realistic. Therefore, a counting system should be implemented for updating the real-time available particle number and the surface fraction per catalytic surface grid cell. In our simulation, each surface grid was assigned memory of its local particle fraction. To save on computing resources, only one array is used to remember the number of B particles consumed in reactions when updating the number of A particles consumed in reactions. Later, a separate function is run to update the real number of B particles in each surface grid.

A porous medium typically provides a larger surface area for catalytic reactions to occur. This means the surface area is very crucial to the total reaction rate. However, the porous structure also influences transport phenomena such as diffusion and convection through the reactor.

To disentangle effects due to increased catalytic area from effects due to the porous structure, in the following we will compare two systems with different structure but the same catalytically active area. Figure 5.12 shows the product C concentration in a planar catalyst geometry (a) compared with that in a porous catalyst geometry (b). In both cases a flow is driven from bottom to top through the reactor, and both reactors have the same catalyst area. To ensure a steady state can be reached, the product particles C are continually reset to A and B particles (corresponding to a zero C concentration) in the top and bottom regions.
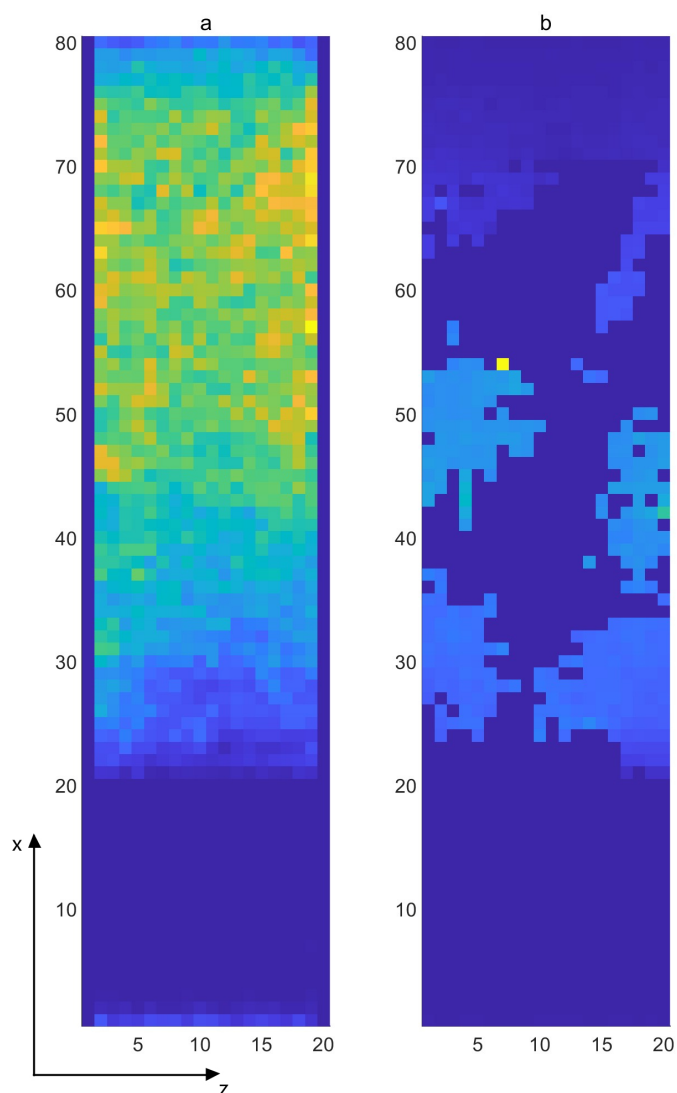
Figure 5.12: Product C concentration map between $y = 10$ and $y = 11$: (a) With planar catalyst geometry; (b) With porous media catalyst geometry. Brighter colors correspond to higher concentrations. The flow is from bottom to top and both reactors have the same catalyst area. Note that the color maps are different for (a) and (b), with the product concentration typically an order of magnitude higher in (b).
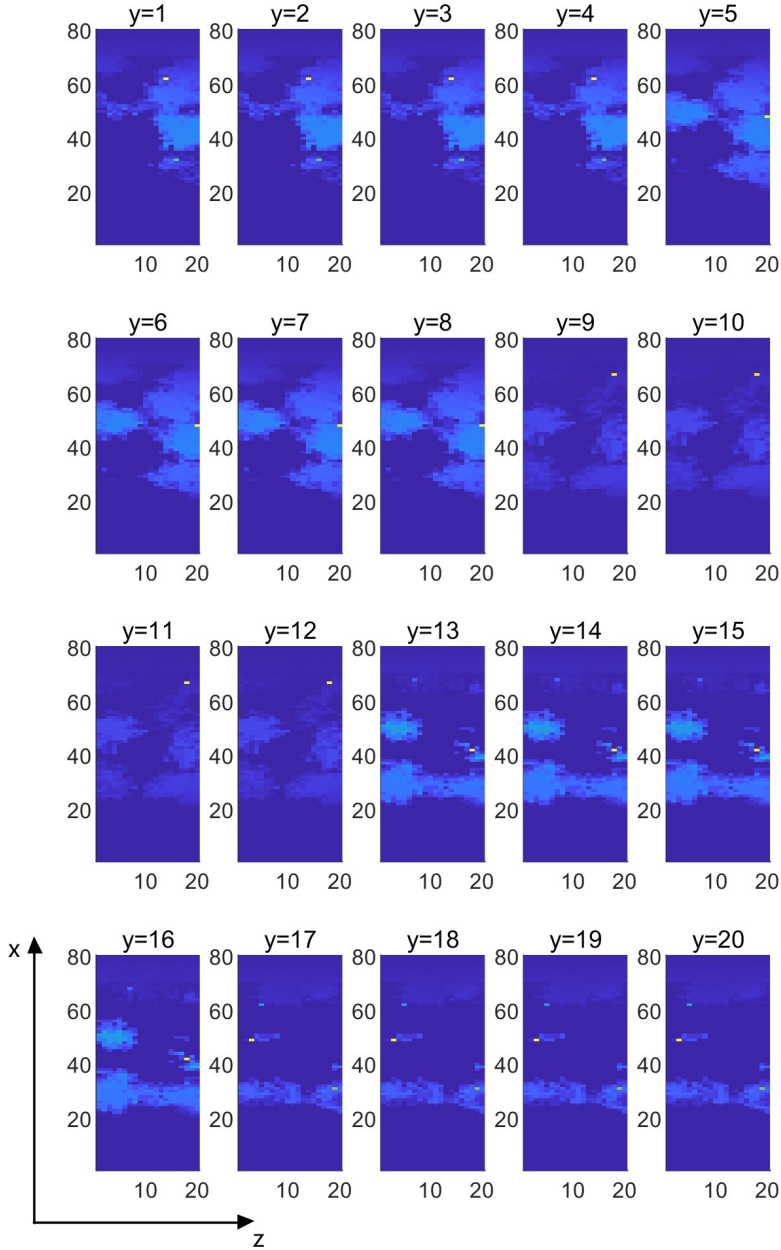
Figure 5.13: Slices of the product C concentration map in the xz-plane for different y values in the porous medium catalyst geometry. Brighter colors correspond to higher concentrations.

Figure 5.12 shows that for the planar geometry, as expected, the largest product concentrations occur near the catalyst planes at the sides (minimum and maximum z). By contrast, in the porous medium the local product concentration is strongly influenced by the porous structure. Note that the color maps are different, with the concentration typically an order of magnitude higher for the porous medium than for the planar catalyst.

To show the difference in product concentration more quantitatively, Figures 5.14 and 5.15 give the 1D-averaged product mole fraction along the x direction. Each 1D plot is an average of 5 sets of sample results, each sample is obtained by averaging over a 200 unit simulation time. It can be observed that for the planar catalyst, the product mole fraction increases until almost the end of the catalyst area at $x = 70$. However, the product mole-fraction profile for the porous media catalyst geometry is more jagged, with a peak concentration at around $x = 50$, showing the influence of the larger resistance of the geometry, leading to a lower flow velocity and therefore relatively larger influence of backdiffusion from the zero concentration boundary.
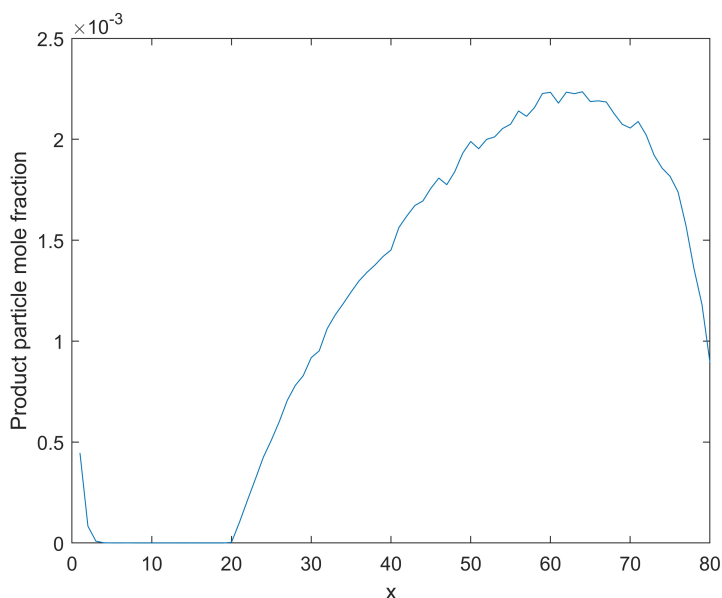

Figure 5.14: Average product C mole fraction as a function of x coordinate for the planar catalyst surface.

5.5   CONCLUSION

In this chapter, we showed how the SRD method can be modified to model heterogeneous catalytic surface reactions and bulk flow in a complex random geometry. The presence

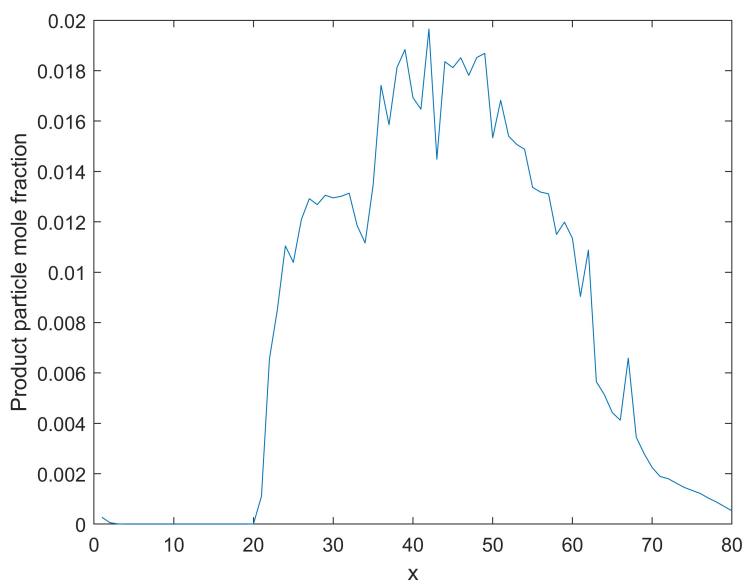Figure 5.15: Average product C mole fraction as a function of x coordinate for the porous media catalyst geometry.

of porous media alters the fluid dynamics within the reactor. To further help with the catalyst geometry design, information related to flow field analysis may be needed, such as the velocity distribution and velocity fields. This was not addressed in this work, but could be considered in future work.

REFERENCES

[1] L.B. McCusker Ch. Baerlocher. *Database of Zeolite Structures*. URL: `http://www.iza-structure.org/databases/`.

[2] Frerich J Keil. "Complexities in modeling of heterogeneous catalytic reactions." In: *Computers & Mathematics with Applications* 65.10 (2013), pp. 1674–1697.

[3] Joseph Hoshen and Raoul Kopelman. "Percolation and cluster distribution. I. Cluster multiple labeling technique and critical concentration algorithm." In: *Physical Review B* 14.8 (1976), p. 3438.

[4] Marvin FL Johnson and Warren E Stewart. "Pore structure and gaseous diffusion in solid catalysts." In: *Journal of Catalysis* 4.2 (1965), pp. 248–252.

[5] JW Beeckman and Gilbert F Froment. "Catalyst deactivation by site coverage and pore blockage: Finite rate of growth of the carbonaceous deposit." In: *Chemical Engineering Science* 35.4 (1980), pp. 805–815.

[6] Sebastián Reyes and Klavs F Jensen. "Estimation of effective transport coefficients in porous solids based on percolation concepts." In: *Chemical engineering science* 40.9 (1985), pp. 1723–1734.

[7] Alan R Kerstein. "Equivalence of the void percolation problem for overlapping spheres and a network problem." In: *Journal of Physics A: Mathematical and General* 16.13 (1983), p. 3071.

[8] Petikirige Sadeep Madhushan Thilakarathna, KS Kristombu Baduge, Priyan Mendis, Vanissorn Vimonsatit, and Hanseung Lee. "Mesoscale modelling of concrete–a review of geometry generation, placing algorithms, constitutive relations and applications." In: *Engineering Fracture Mechanics* 231 (2020), p. 106974.

[9] Nicole GÜLdemeister, Kai WÜNnemann, Nathanael Durr, and Stefan Hiermaier. "Propagation of impact-induced shock waves in porous sandstone using mesoscale modeling." In: *Meteoritics & Planetary Science* 48.1 (2013), pp. 115–133.

[10] Zachary Grant Mills, Wenbin Mao, and Alexander Alexeev. "Mesoscale modeling: solving complex flows in biology and biotechnology." In: *Trends in biotechnology* 31.7 (2013), pp. 426–434.

[11] Meisam Tarabkhah and Behnam Khoshandam. "Simulation of Structure Change in Porous Media During Gas–Solid Reactions Using Cellular Automata Model." In: *Transport in Porous Media* 128 (2019), pp. 553–570.

[12]   megavoxels. *Voxel Art Tutorial: What are Voxels and How to Make Them*. en-US. July 2021. URL: https://www.megavoxels.com/learn/voxel-art-tutorial-what-are-voxels-and-how-to-make-them/ (visited on 06/25/2024).

[13]   Zhiqiang Niu, Valerie J Pinfield, Billy Wu, Huizhi Wang, Kui Jiao, Dennis YC Leung, and Jin Xuan. "Towards the digitalisation of porous energy materials: evolution of digital approaches for microstructural design." In: *Energy & environmental science* 14.5 (2021), pp. 2549–2576.

[14]   Shuaibing Song. "An improved simulated annealing algorithm for reconstructing 3D large-scale porous media." In: *Journal of Petroleum Science and Engineering* 182 (2019), p. 106343.

[15]   Yuqi Wu, Chengyan Lin, Lihua Ren, Weichao Yan, Senyou An, Bingyi Chen, Yang Wang, Xianguo Zhang, Chunmei You, and Yimin Zhang. "Reconstruction of 3D porous media using multiple-point statistics based on a 3D training image." In: *Journal of Natural Gas Science and Engineering* 51 (2018), pp. 129–140.

[16]   Moran Wang, Jinku Wang, Ning Pan, and Shiyi Chen. "Mesoscopic predictions of the effective thermal conductivity for microscale random porous media." In: *Physical Review E* 75.3 (2007), p. 036702.

[17]   PV Coveney, J-B Maillet, JL Wilson, PW Fowler, O Al-Mushadani, and BM Boghosian. "Lattice-gas simulations of ternary amphiphilic fluid flow in porous media." In: *International Journal of Modern Physics C* 9.08 (1998), pp. 1479–1490.

[18]   Paul Meakin. *Fractals, scaling and growth far from equilibrium*. Vol. 5. Cambridge university press, 1998.

[19]   Rong Fan, Githin T Zachariah, Johan T Padding, and Remco Hartkamp. "Real-time temperature measurement in stochastic rotation dynamics." In: *Physical Review E* 104.3 (2021), p. 034124.

6

CONCLUSIONS & OUTLOOK

6.1 CONCLUSIONS

This thesis proposed an approach of simulating heterogeneous catalytic reactions in complex catalyst geometries and reactor environments. The complexity of addressing this problem has several aspects:

- Simulating macroscopic properties of the bulk fluid under the continuum assumption while random behavior, especially for spontaneous random surface reactions, is simultaneously relevant at the microscopic scale.

- Simulating microscopic stochastic properties such as molecular adsorption while simultaneously simulating complex surface reaction mechanisms.

- Implementing real-time temperature measurement and heat transfer as a result of the energy change caused by chemical reactions.

- Simulating microscopic stochastic properties in combination with complex catalyst microstructures.

In Chapter 3, the Stochastic Rotation Dynamics (SRD) method was extended to enable real-time measurement of properties, in particular temperature. Based on kinetic theory and combining with a new form of ensemble averaging, the real-time temperature measurement is tested on various standard cases for validation. Coupling with the conduction equation, the influence of solid surface temperature patterns and to the catalyst and local fluid is demonstrated. The method is tested in the case of temperature dependent probability to surface adsorption and temperature dependent desorption to show the match with analytical solution. A catalyst sphere was used to test the combined model and highlighted the capability of the developed technique to simultaneously solve for the transient evolution of macroscopic transport properties such as mean velocity, temperature and concentration, along with employing an accurate wall reaction mechanism.

The aim of Chapter 4 was to develop and apply stochastic rotation dynamics to explore heterogeneously catalyzed multi-particle reactions. In this chapter, heterogeneously catalyzed mean-field reaction mechanisms were developed by applying an infinite surface

diffusion assumption. This model was numerically validated by linking the simulation parameters and the mean-field rate constants. The accuracy of the results is negatively influenced by applying too large reaction probabilities. Therefore, we concluded that to simulate cases with higher reaction rates instead of increasing the reaction probability constant, the frequency with which the catalyst sites are updated should be increased. The non mean-field reactions in reactions in which surface interactions of the particles are considered were simulated by implementing a hybrid of stochastic rotation dynamic method and mesoscopic Monte-Carlo simulation on the planner catalytic surface. Island formation was observed by applying interactions between different particle species. Second-neighbor interactions and other simulation parameters were tested to be necessary for smoother island boundaries. An A+B → C reaction was compared between mean-field and non mean-field regimes to show significant differences caused by the island formations. A three-step reaction mechanism, which is widely employed for modeling realistic reaction mechanisms, was simulated at the end of the chapter. Repulsive interactions and a low desorption rate inducing catalyst poisoning effects were included in the simulation to show the capability of the hybrid method to couple detailed surface information (such as surface interaction and coverage results) to spatial concentration variations in the bulk of a multi-component gas mixture.

The potential of the SRD method to simulate the complex geometry of a real catalyst was explored in Chapter 5. The compatibility of SRD with different random or structured geometry generating methods enables the study of various types of catalyst applications in a very convenient way. The results reveal that the shape of catalyst affects the reaction by influencing the balance between available reactive surface area and mass transport (flow and diffusion). The porous media geometry could create barriers that slow down the movement of the reactive flow when increasing the chance of particle collision with the reactive surface, affecting the reaction rate. In a complex catalyst geometry, balancing and optimization of mass transfer dominated reaction rates, conversion and productivity become complicated. The complex nature of catalytic systems requires thorough approaches to understand the process and collect important data and information for further design and improvement work of the system. Direct simulation can play a key role in reactor control, for it could give a realistic prediction of the reaction condition, mass transfer, catalyst activity and heat transfer. Chapter 5 provided an example, where such a complex catalyst system could be simulated by application of SRD with its high computation efficiency and intuitive and minimalist algorithms of mapping the catalyst geometry and tackling the particle movement in such complex geometry. However, when employing SRD to solve real physics problems, it should be noted that the method has its limitations of representing microscale phenomena with coarse grained simplifications. The details of molecular level rely on the researcher's assumptions. The value of this method is to provide a bridge of

phenomena at different scales, but weighing the balance between the level of detail and computational efficiency requires conscientious consideration.

6.2 OUTLOOK

The development of the SRD method in this work was aimed at extending the capability of the method for simulating more complex physical and chemical phenomena. To further enhance the feasibility of the method, several advanced developments are under consideration, exploring ways to utilize the advantages of SRD in addressing more complex multi-physical problems.

When using the replica approach (Chapter 3), the SRD method is highly parallelizable since there is very limited interaction between individual instances of the simulation. However, further optimization of each replica could drastically improve the computing efficiency, making it more accessible to larger and more complex system for more applications.

Chemical poisoning of heterogeneous catalyst was briefly studied in Chapter 4. However, the influence of catalyst physical poisoning and geometrical change caused by the blockage of microchannels and pores has not yet been touched by current SRD simulations. These effects have far-reaching impact on effective reaction rates.

For simplicity, in this work, temperature measurement, surface interaction and complex geometry were meshed with Cartesian grids. However, the voxelation used in Chapter 5 can result in surface errors. More precise meshing techniques can offer a more accurate simulation of the real physical problem, especially for surfaces with curvature. This will not only rectify the voxelization errors but also amplify the level of precision in both the identification and adsorption of particles onto the surface, giving an overall improvement in the accuracy and efficacy of the simulation.

A combination of complex geometry, complex non-mean-field surface reactions, and temperature effects could be explored through simulations. Although all three features were simulated separately in this work, their combination still needs to be developed to simulate real complex heterogeneous chemical reactions in porous reactor environments.

Finally, although computational simulations could provide powerful predictions and observations of complex phenomena, their accuracy and reliability depend on their simplifications of real physics and assumptions. Meanwhile, by contrasting simulation results with experimental results, potential discrepancies and limitations of the computational approach could be detected. To further improve the performance of the developed simulation method and ensure the credibility of theoretical assumptions, experimental validation is crucial.

PART II APPENDIXES

a

A.1 SIMULATING HETEROGENEOUS REACTIONS

In this work we use the reaction method suggested by Sengar [1]. When a SRD particle bounces on a catalytic surface, the particle will be adsorbed with a certain probability p_a. In a single time step Δt_s, for adsorbed particles, further probabilities for reaction and desorption can be applied. Based on this, the intrinsic rates in terms of the SRD simulation parameters can be calculated. In the following, to simplify our notation, we will assume that the probabilities per time step are sufficiently small. If large probabilities ($0.1 < p \leqslant 1$) are used, the conversion to rates should be done according to $k = -\ln(1-p)/\Delta t_s$, see [1] for a detailed explanation.

The kinetic model used by Pooley and Yeomans [2] is extended to derive an expression for the particle collision rate at walls. The collision frequency, i.e. the number of collisions occurring per unit area of the wall per unit time step, is:

$$Z = C_s \langle |v_y| \rangle \tag{S1}$$

In this expression, C_s is the number density of the particle species of interest and $|v_y|$ is the average velocity of the particles perpendicular to the wall (in this example the wall normal is chosen in the y-direction). The expectation value of $|v_y|$ from the Maxwell-Boltzmann distribution is $\sqrt{2k_b T/(\pi m)}$. The adsorption rate, i.e. the number of adsorption events per unit area of catalytic surface per unit time, can therefore be expressed as

$$R_a = C_s \sqrt{\frac{2k_b T}{\pi m}} p_a \tag{S2}$$

The adsorption probability per collision event p_a depends on local temperature through the activation energy for adsorption E_a, which arises from the Eyring-Polanyi equation in Transition State theory, and depends on the fractional catalytic surface coverage $\theta = N_a/N_{cat}$, where N_a is the number of adsorbed particles per unit area and N_{cat} is the number of adsorption sites per unit area of catalytic surface. In this work, we use a first order (Langmuir model) dependence on the fraction of empty sites $(1-\theta)$, giving us the following expression for adsorption probability:

$$p_a = p_a^0 (1-\theta) e^{-E_a/k_B T} \tag{S3}$$

where p_a^0 is the adsorption probability pre-exponential factor.

If there are $N_{r,a}$ reactant particles adsorbed per unit area catalytic surface (remember that there may also be adsorbed product particles), we can write the reaction rate, i.e. the number of reactant particles converted to product particles per unit area per unit time, as:

$$R_r = N_{r,a} k_r \tag{S4}$$

where k_r is the reaction rate which in the simulations is controlled by setting the reaction probability p_r:

$$k_r = \frac{p_r}{\Delta t_s} \tag{S5}$$

Here p_r is the probability of an adsorbed reactant particle to react to an adsorbed product particle during a single time step Δt_s. This probability can be written in the form of an Arrhenius equation (similar to the adsorption probability):

$$p_r = p_r^0 e^{-E_r/k_B T} \tag{S6}$$

where p_r^0 is the reaction probability pre-exponential factor and E_r is the activation energy for the reaction.

A similar approach can be adopted to determine the desorption rate per unit area catalytic surface. For example, focusing on desorption of product particles, we have:

$$R_d = N_{p,a} k_d \tag{S7}$$
$$k_d = \frac{p_d}{\Delta t_s} \tag{S8}$$
$$p_d = p_d^0 e^{-E_d/k_B T} \tag{S9}$$

where $N_{p,a}$ is the number of adsorbed product particles per unit area, k_d is the desorption rate, p_d is the probability of an adsorbed particle to desorb during a time step Δt_s, E_d is the desorption activation energy and p_d^0 is the pre-exponential factor. Although in this work they are chosen equal, different desorption activation energies and pre-exponential factors may be chosen for the reactant particles.

b

B.1 NUMERICAL SOLUTION FOR FIRST-ORDER REACTION $A \to B$

In this work, when validating the simulation with continuum numerical models, the unsteady diffusion partial differential equation (4.14) valid inside the fluid is discretized along the y-axis using a finite difference scheme:

$$C_{A,i}^{l+1} = C_{A,i}^{l} + \frac{D_A \Delta t}{\Delta y^2}(C_{A,i+1}^{l} - 2C_{A,i}^{l} + C_{A,i-1}^{l}). \tag{S1}$$

In this expression, $C_{A,i}^{l}$ represents the particle concentration of species A on an interior cell i at time step l. A similar scheme can be built for the cells at the edge of the nonreactive wall, at which a zero flux boundary condition is imposed. If n denotes the cell at this nonreactive boundary, the cell at $n+1$ is fictitious and only used to satisfy the no-flux boundary condition:

$$\left. \frac{dC_A}{dy} \right|_{y=L_y} = 0 \approx \frac{C_{A,n+1}^{l} - C_{A,n-1}^{l}}{2\Delta y},$$

$$C_{A,n+1}^{l} = C_{A,n-1}^{l}. \tag{S2}$$

On the reactive wall, the boundary condition takes the form of:

$$-D_A \left. \frac{dC_A}{dy} \right|_{y=0} = -k_{ads} \frac{N_{cat}}{A_{cat}} \theta_v C_A + k_{des} \frac{N_{cat}}{A_{cat}} \theta_A. \tag{S3}$$

In the expression above, N_{cat} is the total number of catalytic sites while A_{cat} is the total area of the reactive catalyst. The total number of catalyst sites remains constant throughout the simulation. C_A refers to the A concentration at $y = 0$. The boundary cell at the reactive wall can be updated using F_A to represent the flux at the right hand side of Eq. (S3):

$$-D_A \frac{C_{A,1}^{l} - C_{A,-1}^{l}}{2\Delta y} = F_A \tag{S4}$$

leading to

$$C_{A,-1}^l = \frac{2\Delta y F_A}{D_A} + C_{A,1}^l \tag{S5}$$

$$C_{A,0}^{l+1} = C_{A,0}^l + \frac{D_A \Delta t}{\Delta y^2}(2C_{A,1}^l - 2C_{A,0}^l + \frac{2\Delta y F_A}{D}) \tag{S6}$$

Note that for the derivation of the expression for k_{ads} in Sec.4.2.2, a constant concentration profile was assumed in the bulk. If the difference of concentration between the surface and bulk is small, the SRD and numerical model match very well. Large concentration gradients will require a more elaborate expression for the mean-field adsorption rate constant, which is beyond the scope of this work.

B.2 ERROR ESTIMATION

Using the Taylor series expansion, the maximum error (Er) associated with Eqs. (4.18) can be calculated as:

$$Er = \frac{1}{\rho_{S,A}} \max\left(\frac{\Delta t_s^2}{2} \frac{d^2\rho_A}{dt^2}\right) \tag{S7}$$

Using Eqs. (4.15-4.16), the second derivative of $\rho_{S,A}$ is calculated as:

$$\frac{d^2\rho_A}{dt^2} = -k_{r,AB}\rho_{A_{i-1}}\frac{d\rho_B}{dt} - k_{r,AB}\frac{d\rho_A}{dt}\rho_{B_{i-1}}$$

$$= k_{r,AB}^2\rho_{A_{i-1}}^2\rho_{B_{i-1}} + k_{r,AB}^2\rho_{A_{i-1}}\rho_{B_{i-1}}^2 \tag{S8}$$

Therefore,

$$Er = \frac{\Delta t_s^2}{2}(k_{r,AB}^2\rho_{B_{i-1}}^2 + k_{r,AB}^2\rho_{A_{i-1}}\rho_{B_{i-1}}) \tag{S9}$$

To keep the accuracy of Eqs. (4.20) as high as possible, we aim to keep the relative error of $\frac{\rho_{S,A}}{\rho_{S,A_{i-1}}}$ to stay below 1%. The maximum numerical relative error can be guaranteed to be lower than the following expression:

$$MaxErr < \frac{1}{2}(P_{re,AB}^2\theta_{B0}^2 + P_{re,AB}^2\theta_{A0}\theta_{B0}) \tag{S10}$$

The surface coverages θ_{B0} and θ_{A0} are bounded between 0 and 1. When the desired maximum relative error is 1%, the condition $P_{re,AB} < 0.14$ is deemed sufficient.

C

A pseudo-code of the channel generating method is shown as follows:

```
Lx = 50;
Ly = 40;
Lz = 40;
C = 5; %initial seeds
Voxel=zeros(Lx,Ly,Lz);
Sx=20; %starting x coordinate
Se=40; %end x coordinate
LS = Se-Sx;
ps = 0.4; %forward probability
pi = (1-ps)/4; %other direaction growth probability
for i=Sx:Se
    for j=1:Ly
    for k=1:Lz
    Voxel(i,j,k) = 1;
    end
    end
end
listy = zeros(1,C);
listz = zeros(1,C);
for i=1:C
    y = floor(rand*(Ly-1)+1);
    z = floor(rand*(Lz-1)+1);
    if(Voxel(Sx,y,z)>0)
        Voxel(Sx,y,z)=0; end
    listy(1,i)=y;
    listz(1,i)=z;
end
for j=1:C
    i = Sx;
    choice = 0;
```

```
while i<=Se
    y = listy(j);
    z = listz(j);
    j
    choice = rand;
    l =i;
    if choice<=ps
    i = i+1;
    if i<Se+1
    Voxel(i,y,z)=0; end
    end
   if choice<=ps+pi*1 && choice>ps
    y = y-1;
    y = mod((y-1),Ly)+1
    Voxel(i,y,z)=0;
   end
    if choice<=ps+pi*2 && choice>ps+pi*1
    y = y+1;
    y = mod((y-1),Ly)+1
    Voxel(i,y,z)=0;
    end
    if choice<=ps+pi*3 && choice>ps+pi*2
    z = z-1;
    z = mod((z-1),Lz)+1
    Voxel(i,y,z)=0;
    end
    if choice<=ps+pi*4 && choice>ps+pi*3
    z = z+1;
    z = mod((z-1),Lz)+1
    Voxel(i,y,z)=0;
    end
    listy(j)= y;
    listz(j)= z;
end
end
```
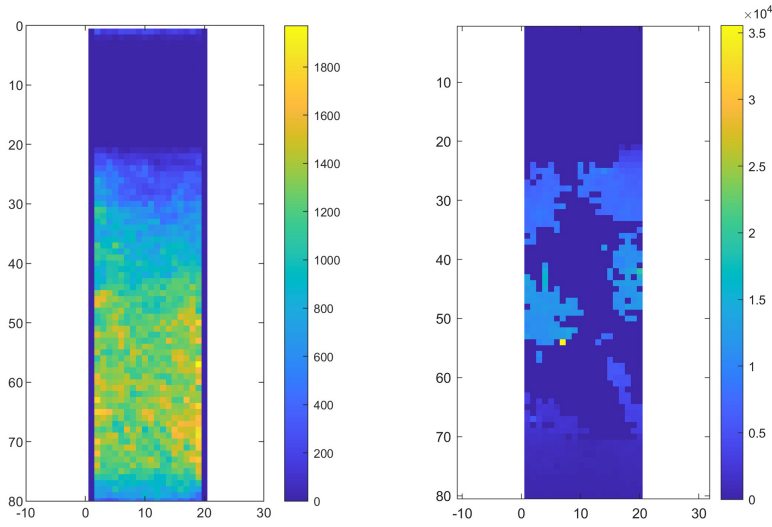
Figure S1: Product C concentration map between $y = 10$ and $y = 11$ with color bar of the numerical count value of C particle in 2000 unit time: (a) With planar catalyst geometry; (b) With porous media catalyst geometry. Brighter colors correspond to higher concentrations. The flow is from bottom to top and both reactors have the same catalyst area. Note that the color maps are different for (a) and (b), with the product concentration typically an order of magnitude higher in (b).

PART III

ACKNOWLEDGMENTS

There are many people I must give great appreciation to, for the priceless help and company given to me during my journey of doing phD in Delft. The precious experience is unforgotten and shinning.

First, I would like to convey my deepest appreciation and sincere gratitude to my Prof.dr.ir. Johan Padding, for offering the opportunity and inspiring the idea of this research. Your profound knowledge invaluable insights, unwavering motivation and patience always navigated when I was lost.

I would like to extend my heartfelt appreciation to my co-promotor Dr. Remco Hartkamp. I am incredible thankful for your valuable guidance, practical instruction and constructive suggestions. You nourished my development as a resercher.

I would like to extend my heartfelt thanks to the members of my doctoral committee, Prof.dr.ir Wiebren de Jong, Prof.dr.ir. J(Hans).A.M. Kuipers, Prof.dr. Rene Pecnik, Dr.ir Volkert van Steijn, and Dr. Tom Burdyny, for their valuable input, constructive criticism, and suggestions that greatly enhanced the quality of this research. Their expertise and scholarly contributions have enriched my understanding of the subject matter and strengthened the academic rigor of this work.

I would like to express my sincere appreciation to my master students, Githin T Zachariah and Parsa Habibi, for their unwavering dedication to my PhD research. Their consistent commitment, hard work, and enthusiasm have had a profound impact on the progress and outcomes of my doctoral journey. I am truly grateful for their steadfast pursuit of excellence, their valuable ideas, and their willingness to go the extra mile in their research endeavors. Their unwavering presence and contributions have brought fresh perspectives and invaluable insights that have greatly enriched the quality and depth of my work. I will always cherish their exceptional contributions and consider myself fortunate to have collaborated with such outstanding individuals. To those of you currently embarking on your Ph.D. journey, I sincerely hope that you are fortunate enough, just as I have been, to have the privilege of working with exceptional master students.

I would like to extend my deepest appreciation and gratitude to a group of exceptional individuals who have played a pivotal role in the success of my research.Their support, encouragement, and expertise have tremendous influence to the overall experience of my phD life.

To Rumen and Velislava Georgiev, I am indebted to your hands on assisting and accompany when I am in trouble and frustration. You stood by me in the moment when academic and life pressure seemed insurmountable. The listening ear and wise counsel

has been a lifeline during challenging times. Thank you both for being wonderful friends and comforter and being the Great Summer's parent.

In the journey of completing this thesis, I've been fortunate to be surrounded by an exceptional group of peers and friends who have provided unwavering support and camaraderie. To my fellow graduate students and colleagues, your shared experiences, insightful discussions, and mutual encouragement have been invaluable throughout this academic endeavor. Whether it was collaborating on research projects, exchanging ideas during seminars, or simply lending a listening ear during challenging times, your presence has made this journey both enriching and enjoyable. Special thanks to To Arvind Pari, Esaar Butt, Nagaraj Nagalingam, Ravi Ramesh, Elyas Mohammadzadeh Moghaddam, Stephan Sneijders, Suriya Senthil Kumar, Heng Li, Qi An, Pingping Cui, Mengmeng Zhang, Peng Yan, Zhiyi Leong, Fatma Ibis-Ozdemir, Rishabh Ghotge, Vikram Korede, Nikhilesh Kodur Venkatesh, Wouter van der Does, Joe Blake, Marko Draskić, Aviral Rajora, Willem Haverkort, Sevgi PolatShilong Fu, Nandalal Girichandran, Asvin Sajeev Kumar, Hengameh Farahmandazad, Boaz Izelaar, Katie Lawrence, Daniel van den Berg, Simone Asperti, Wenze Guo, Pedro Costa, Luis Cutz, Willy Huang, An Zhao, Teng Dong, Bin Fang, Liangyuan Wei, Xuan TaoJie RenMengmeng RenXu Huang, Ivan Mema, Vinay V Mahajan, Sathish Krishnan P. Sanjeevi, Junaid Mehmood, whose friendship has been a source of inspiration and motivation. Your belief in my abilities and willingness to celebrate both the triumphs and setbacks have made this journey all the more meaningful. This thesis stands as a testament to the collective efforts of this remarkable community of peers and friends, and for that, I am profoundly grateful.

To my dearest fellow Chinese friends: Mengmeng Zhang, Haoyu Li, Shilong Fu, Pingping Cui, Qi An, Heng Li, An Zhao, Xuan Tao, Liangyuan Wei, Willy, Peng Yan, Meng Wang, Bing Fang, Teng Dong, Wenze Guo, Zac Leong, Jie Ren, Mengmeng Ren, who always help me find solace and comfort, your understanding and support provided a sense of belonging and connection. The shared experiences were a balm to the soul. This thesis bears witness to the enduring friendships forged in the crucible of academia, and I am forever grateful for the sense of home you brought to this journey.

I would like to express my sincere appreciation to the dedicated individuals who provide invaluable support behind the scenes in academia, to Linda Starrenburg- Hannewijk and Leslie van Leeuwen.

Rong Fan
June, 28th, 2024

CURRICULUM VITAE

PERSONAL INFORMATION

FULL NAME: Rong Fan

BIRTH DATE: 11-12-1990

NATIONALITY: Chinese

EDUCATION

2017-2024: PhD Research Scholar, Process & Energy Department, Delft University of Technology, The Netherlands.

2014-2016: MSc in Chemical Engineering, Eindhoven University of Technology, The Netherlands.

2009-2013: BSc in Chemical Engineering, Xiamen University, China.

LIST OF PUBLICATIONS

[1] Fan, R., Zachariah, G. T., Padding, J. T., Hartkamp, R. (2021). Real-time temperature measurement in stochastic rotation dynamics. Physical Review E, 104(3), [034124]. https://doi.org/10.1103/PhysRevE.104.034124

[2] Fan, R., Habibi, P., Padding, J. T., Hartkamp, R. (2022). Coupling mesoscale transport to catalytic surface reactions in a hybrid model. Journal of Chemical Physics, 156(8), [084105]. https://doi.org/10.1063/5.0081829

[3] Fan, R., Padding, J.T., Hartkamp, R. Simulating reactions in complex geometries using Stochastic Rotation Dynamics. *To be submitted (2024).*